

ANALYTICAL PERFORMANCE EVALUATION OF HOLLOW PRESTRESSED  
PILES AND PILE-CAP CONNECTIONS IN THE I-5 RAVENNA BRIDGE

By

STEVEN MICHAEL GREENWOOD

A thesis submitted in partial fulfillment of  
the requirements for the degree of

MASTER OF SCIENCE IN CIVIL ENGINEERING

WASHINGTON STATE UNIVERSITY  
Department of Civil and Environmental Engineering

DECEMBER 2008

To the Faculty of Washington State University:

The members of the Committee appointed to examine the thesis of STEVEN  
MICHAEL GREENWOOD find it satisfactory and recommend that it be accepted.

---

Chair

---

---

---

## **ACKNOWLEDGEMENT**

There are many people I wish to thank who directly and indirectly helped me with this work. I would like to express my sincere gratitude to Dr. William Cofer, my advisor and committee chair, for introducing me to the world of Finite Element Analysis, and having faith and trust in my abilities as a student and researcher. He has provided invaluable knowledge, patience, and guidance throughout this work.

Special thanks To Dr. Mohamed ElGawady for all his time devoted to frequent, unexpected discussions and near daily use of his computer. To Dr. Balasingam Muhunthan, I extend my thanks for the discussions pertaining to plasticity and helping me identify the crucial geotechnical aspects of this research. I am deeply obliged to Dr. David McLean for his constructive criticism and questioning while discussing results of this work. As my committee members and as individuals I thank them for all their help and guidance, which inspired me to push my own limits.

I would like to thank the Washington State Department of Transportation (WSDOT) for providing funding for this research under Project No. 5200. This work would not have been possible without their financial support. In addition, I would like to thank Mr. Craig Boone and Mr. DeWayne Wilson for their guidance, expertise, and promptness during this collaborative effort. Their assistance is greatly appreciated.

Finally, I extend a very special thank you to my family, especially Mom, Dad and Doug, for their eternal love, encouragement, and support.

ANALYTICAL PERFORMANCE EVALUATION OF HOLLOW PRESTRESSED  
PILES AND PILE-CAP CONNECTIONS IN THE I-5 RAVENNA BRIDGE

**Abstract**

By Steven Michael Greenwood, M.S.  
Washington State University  
December 2008

**Chair:** William F. Cofer

The Washington State Department of Transportation (WSDOT) developed a bridge seismic retrofit program in 1990 in order to address seismic risk associated with state owned bridges. There are 22 bridges with hollow-core pile foundations located on I-5, I-405, and State Route 520 in the Puget Sound region of Washington State. Sudden, catastrophic failure has been observed in tested piles of this configuration at displacement ductilities of four or less.

In order to investigate the behavior of the *in situ* hollow-core piles and pile-to-cross-beam connections used in the I-5 Ravenna Bridge near Seattle, Washington, a series of nonlinear 3D finite element (FE) analyses were performed using ABAQUS/Standard. In addition, 2D nonlinear Winkler beam models were developed using SAP2000 Advanced Nonlinear in conjunction with XTRACT in order to evaluate its model's ability to predict failure. The FE and beam models developed were calibrated against existing experimental data.

The proposed FE model is capable of capturing the behavior of prestressed hollow core concrete piles. During calibration, load capacity and displacement ductilities at yield and failure were well-predicted with an over-prediction in strength of roughly 20%.

Results from the FE analyses for the *in situ* hollow pile illustrated that confining pressure supplied by the soil does not provide appreciable strength to the cover concrete. The subgrade plastic hinge was found to vary from 2.88 to 3.0 pile diameters and was located, on average, 610 mm (24 in.) below ground level, depending on the soil model.

The Winkler beam models were found to provide a conservative approximation for the load-displacement response of the 3D FE models. The simplified analyses under-predicted load capacity and displacement ductility capacity by roughly 30 percent.

For the connection, a 50 percent reduction in axial load reduced the post-yield moment response by roughly 10 percent. Modeling the connection as fixed reduces the rotation capacity by nearly 60 percent while the moment capacity is virtually unaffected. It is recommended that the rotational stiffness of the connections be taken as the equivalent energy elastic-plastic response of the moment-rotation response obtained from the proposed finite element model.

## TABLE OF CONTENTS

	Page
<b>CHAPTER ONE .....</b>	<b>1</b>
<b>1. INTRODUCTION.....</b>	<b>1</b>
<b>1.1 BACKGROUND.....</b>	<b>1</b>
<b>1.2 RESEARCH OBJECTIVES.....</b>	<b>4</b>
<b>1.3 SEISMICITY OF WESTERN WASHINGTON STATE.....</b>	<b>5</b>
<b>1.4 ORGANIZATION OF THESIS .....</b>	<b>6</b>
<b>CHAPTER TWO .....</b>	<b>8</b>
<b>2. LITERATURE REVIEW .....</b>	<b>8</b>
<b>2.1 INTRODUCTION.....</b>	<b>8</b>
<b>2.2 EXPERIMENTAL WORK .....</b>	<b>9</b>
<b>2.3 ANALYTICAL MODELING .....</b>	<b>12</b>
<b>2.4 CONCRETE CONSTITUTIVE MODELS .....</b>	<b>15</b>
2.4.1 LINEAR AND NONLINEAR ELASTICITY .....	16
2.4.2 PERFECT PLASTICITY .....	17
2.4.3 WORK-HARDENING PLASTICITY .....	18
2.4.4 ENDOCHRONIC PLASTICITY.....	19
<b>CHAPTER THREE .....</b>	<b>20</b>
<b>3. MODEL CALIBRATION.....</b>	<b>20</b>
<b>3.1 PILE DESCRIPTION .....</b>	<b>20</b>
<b>3.2 XTRACT.....</b>	<b>21</b>

3.2.1	INTRODUCTION .....	21
3.2.2	MODEL FORMULATION .....	22
3.2.3	XTRACT RESULTS .....	23
<b>3.3</b>	<b>ABAQUS/STANDARD.....</b>	<b>28</b>
3.3.1	INTRODUCTION .....	28
3.3.2	MODEL FORMULATION .....	32
3.3.2.1	<i>CONCRETE PROPERTIES</i> .....	32
3.3.2.2	<i>ELASTIC CONCRETE &amp; SADDLE STEEL</i> .....	38
3.3.2.3	<i>HOOP AND LONGITUDINAL REINFORCEMENT</i> .....	38
3.3.2.4	<i>PRESTRESSING STRANDS</i> .....	38
3.3.2.5	<i>RUBBER PADS</i> .....	39
3.3.3	MODEL GEOMETRY .....	39
3.3.4	BOUNDARY & INITIAL CONDITIONS .....	42
3.3.5	LOADING .....	42
3.3.6	ABAQUS RESULTS .....	43
3.3.7	SENSITIVITY ANALYSIS .....	50
<b>3.4</b>	<b>SAP2000 ADVANCED NONLINEAR.....</b>	<b>55</b>
3.4.1	INTRODUCTION .....	55
3.4.2	PLASTIC HINGE DEFINITION .....	55
3.4.3	SAP2000 RESULTS .....	60
<b>3.5</b>	<b>CONCLUSIONS.....</b>	<b>65</b>
	<b>CHAPTER FOUR.....</b>	<b>69</b>
<b>4.</b>	<b>IN SITU PILE MODELING.....</b>	<b>69</b>

<b>4.1</b>	<b>INTRODUCTION .....</b>	<b>69</b>
<b>4.2</b>	<b>PILE DESCRIPTION .....</b>	<b>69</b>
<b>4.3</b>	<b>XTRACT MODELING .....</b>	<b>72</b>
4.3.1	XTRACT RESULTS .....	73
<b>4.4</b>	<b>ABAQUS/STANDARD MODELING .....</b>	<b>75</b>
4.4.1	INTRODUCTION .....	75
4.4.2	MODEL FORMULATION .....	77
4.4.2.1	<i>PRESTRESSING STRANDS AND REINFORCEMENT PROPERTIES .....</i>	<i>77</i>
4.4.2.2	<i>CONCRETE PROPERTIES .....</i>	<i>78</i>
4.4.2.3	<i>BOSTON BLUE CLAY PROPERTIES .....</i>	<i>79</i>
4.4.2.4	<i>OTTAWA SAND PROPERTIES .....</i>	<i>82</i>
4.4.3	MODEL GEOMETRY .....	83
4.4.4	BOUNDARY & INITIAL CONDITIONS .....	86
4.4.5	LOADING .....	89
4.4.6	SOIL-PILE INTERACTION PROPERTIES .....	90
4.4.7	RESULTS, BOSTON BLUE CLAY .....	92
4.4.8	RESULTS, OTTAWA SAND .....	98
<b>4.5</b>	<b>SAP2000 MODELING .....</b>	<b>101</b>
4.5.1	FOUNDATION MODELING .....	101
4.5.2	PLASTIC HINGE DEFINITION .....	102
4.5.3	RESULTS .....	104
<b>4.6</b>	<b>CONCLUSIONS .....</b>	<b>109</b>
<b>CHAPTER FIVE .....</b>	<b>113</b>	



<b>5.</b>	<b>CONNECTION MODELING .....</b>	<b>113</b>
5.1	INTRODUCTION .....	113
5.2	CONNECTION DESCRIPTION.....	113
5.3	BOUNDARY & INITIAL CONDITIONS .....	117
5.4	LOADING.....	118
5.5	CONTACT INTERACTIONS.....	119
5.6	CONNECTION MODEL RESULTS.....	120
5.7	CONCLUSIONS.....	125
	<b>CHAPTER SIX .....</b>	<b>128</b>
<b>6.</b>	<b>CONCLUSIONS .....</b>	<b>128</b>
6.1	SUMMARY .....	128
6.2	CONCLUSIONS: CHAPTER THREE .....	129
6.3	CONCLUSIONS: CHAPTER FOUR .....	131
6.4	CONCLUSIONS: CHAPTER FIVE.....	133
6.5	RECOMMENDATIONS FOR FUTURE RESEARCH.....	134
	<b>REFERENCES.....</b>	<b>136</b>
	<b>APPENDIX.....</b>	<b>141</b>
<b>A.</b>	<b>APPENDIX A .....</b>	<b>142</b>
A.1	SOIL DATA .....	142
A.2	CONNECTION DETAILS.....	144
<b>B.</b>	<b>APPENDIX B .....</b>	<b>148</b>
B.1	SOFT CLAY PRESSURE-DISPLACEMENT DATA.....	148
B.2	MEDIUM CLAY PRESSURE-DISPLACEMENT DATA .....	151

<b>B.3</b>	<b>STIFF CLAY PRESSURE-DISPLACEMENT DATA .....</b>	<b>154</b>
<b>B.4</b>	<b>SOFT CLAY NONLINEAR SPRING DATA .....</b>	<b>157</b>
<b>B.5</b>	<b>MEDIUM CLAY NONLINEAR SPRING DATA .....</b>	<b>160</b>
<b>B.6</b>	<b>STIFF CLAY NONLINEAR SPRING DATA .....</b>	<b>163</b>

## LIST OF TABLES

	Page
<b>Table 3.3.1: Summary of Analyses for Sensitivity Analysis.....</b>	<b>50</b>
<b>Table 4.3.1: Unconfined Concrete Properties .....</b>	<b>72</b>
<b>Table 4.3.2: Longitudinal Reinforcement Properties .....</b>	<b>72</b>
<b>Table 4.3.3: Prestressing Strand Properties .....</b>	<b>72</b>
<b>Table 4.4.1: Prestressing Strand Input .....</b>	<b>77</b>
<b>Table 4.4.2: Longitudinal Rebar and Hoop Input .....</b>	<b>78</b>
<b>Table 4.4.3: Concrete Density and Elastic Behavior Input.....</b>	<b>78</b>
<b>Table 4.4.4: Concrete Compression Hardening Input .....</b>	<b>78</b>
<b>Table 4.4.5: Concrete Tension Stiffening Input .....</b>	<b>79</b>
<b>Table 4.4.6: Concrete Compression Damage Input.....</b>	<b>79</b>
<b>Table 4.4.7: Concrete Tension Damage Input.....</b>	<b>79</b>
<b>Table 4.4.8: Properties of Boston Blue Clay (Murugaiah, 2004).....</b>	<b>80</b>
<b>Table 4.4.9: Summary of Ottawa Sand Properties .....</b>	<b>82</b>
<b>Table 4.4.10: Input Parameters for Initial Geostatic Stresses .....</b>	<b>88</b>
<b>Table 4.4.11: Input Parameters for Initial Void Ratio .....</b>	<b>89</b>
<b>Table 4.5.1: LPILE Input Parameters for Soft, Medium, and Stiff Clay .....</b>	<b>102</b>
<b>Table 4.5.2: SAP2000 M3 Hinge Input Parameters.....</b>	<b>103</b>

## LIST OF FIGURES

	Page
Figure 1.1.1: Location of I-5 Ravenna Bridge (Google Earth, 2008) .....	3
Figure 1.3.1: Schematic of Cascadia Subduction Zone (USGS, 2002) .....	6
Figure 3.1.1: Arrangement of Test Apparatus .....	20
Figure 3.2.1: Stress at Failure for Specimen PS12.....	24
Figure 3.2.2: Stress at Failure for Specimen PS13.....	25
Figure 3.2.3: Comparison of XTRACT and Test Results for Specimen PS12 .....	26
Figure 3.2.4: Effect of Cyclic Loading on Pile Response.....	27
Figure 3.2.5: Comparison of XTRACT and Test Results for Specimen PS13 .....	28
Figure 3.3.1: Idealized Compressive Stress-Strain Relationship.....	34
Figure 3.3.2: Tensile Stress-Displacement Behavior .....	35
Figure 3.3.3: Reinforcement Layout .....	41
Figure 3.3.4: Pile Assembly .....	41
Figure 3.3.5: Comparison of Finite Element and Test Results for Specimen PS12..	45
Figure 3.3.6: Comparison of Finite Element and Test Results for Specimen PS13..	45
Figure 3.3.7: Contour Plot of Compressive Damage, $d_c$ , (x-y section) .....	47
Figure 3.3.8: Contour Plot of Compressive Damage, $d_c$ , (y-z section) .....	47
Figure 3.3.9: Principal Plastic Strain Distribution (x-y section) .....	49
Figure 3.3.10: Principal Plastic Strain Distribution (y-z section).....	49
Figure 3.3.11: Effect of Volumetric Transverse Reinforcement Ratio ( $\rho_t$ ).....	51
Figure 3.3.12: Effect of Fracture Energy, $G_f$ .....	52
Figure 3.3.13: Effect of Concrete Tensile Strength, $f_{sp}$ .....	53
Figure 3.3.14: Effect of Prestressing Force.....	54
Figure 3.4.1: Effective Moment-Curvature Relationships, Specimen PS12.....	56
Figure 3.4.2: Effective Moment-Curvature Relationships, Specimen PS13.....	57
Figure 3.4.3: P-M Interactions (Yield Surfaces) for Specimens PS12 and PS13 .....	57
Figure 3.4.4: Moment-Curvature Relationships for Specimen PS12.....	59
Figure 3.4.5: Moment-Curvature Relationships for Specimen PS13.....	59
Figure 3.4.6: Comparison of SAP2000 and Experimental Results for Specimen PS12 .....	60

Figure 3.4.7: Comparison of SAP2000 and Experimental Results for Specimen PS13 .....	61
Figure 3.4.8: Comparison of SAP2000 and Experimental Results, Specimen PS12. ....	62
Figure 3.4.9: Comparison of SAP2000 and Experimental Results, Specimen PS13. ....	63
Figure 3.4.10: Comparison of ABAQUS, SAP2000, and Experimental Results (Specimen PS12).....	64
Figure 3.4.11: Comparison of ABAQUS, SAP2000, and Experimental Results (Specimen PS13).....	64
Figure 4.2.1: Cross-Section of <i>In situ</i> Piles .....	71
Figure 4.2.2: Transverse Reinforcement Details of <i>In Situ</i> Piles.....	71
Figure 4.3.1: <i>In Situ</i> Pile Cross-Section Model.....	73
Figure 4.3.2: Deformed Cross-Section of <i>In Situ</i> Pile Model .....	74
Figure 4.3.3: Moment-Curvature Ductility Relationship for <i>In Situ</i> Pile.....	75
Figure 4.4.1: Void Ratio vs. Depth, Boston Blue Clay .....	81
Figure 4.4.2: Schematic for Determining Void Ratio Axis Intercept.....	81
Figure 4.4.3: <i>In Situ</i> Pile Model Assembly and Mesh.....	85
Figure 4.4.4: <i>In Situ</i> Pile Reinforcement and Tendon Assembly.....	86
Figure 4.4.5: <i>In Situ</i> Pile Boundary Conditions .....	87
Figure 4.4.6: <i>In Situ</i> Pile Contact Surface Definitions.....	90
Figure 4.4.7: <i>In Situ</i> Pile Deformed Shape (Boston Blue Clay) .....	92
Figure 4.4.8: Pile Compression Damage, Side View (Boston Blue Clay).....	93
Figure 4.4.9: Pile Compression Damage, End View (Boston Blue Clay) .....	94
Figure 4.4.10: Inelastic Strain Distribution, z-component (Boston Blue Clay) .....	95
Figure 4.4.11: Comparison of Failure Measures.....	96
Figure 4.4.12: Soil Confining Pressure on Plastic Hinge Region (Boston Blue Clay) .....	97
Figure 4.4.13: Pile Compression Damage, Side View (Ottawa Sand) .....	98
Figure 4.4.14: Pile Compression Damage, End View (Ottawa Sand) .....	99
Figure 4.4.15: Soil Confining Pressure on Plastic Hinge Region (Ottawa Sand)....	100
Figure 4.5.1: SAP2000 Beam Model of <i>In Situ</i> Pile .....	104
Figure 4.5.2: Effect of Varying Foundation Stiffness, $L_p = 1.4 \cdot D$ .....	105

Figure 4.5.3: Effect of Plastic Hinge Length, Soft Clay Foundation .....	106
Figure 4.5.4: Comparison of SAP2000 and ABAQUS Results, Soft Clay Foundation .....	107
Figure 4.5.5: Effect of Including Confining Pressure In SAP2000 Model.....	108
Figure 5.2.1: Connection Model Overview .....	114
Figure 5.2.2: Cross Beam and Plug Rebar Layout .....	115
Figure 5.2.3: Connection Model Assembly .....	116
Figure 5.3.1: Connection Model Boundary Conditions.....	118
Figure 5.5.1: Connection Model Contact Surface Definitions .....	120
Figure 5.6.1: Overview of Tensile Damage, $d_t$ , Distribution in Connection .....	121
Figure 5.6.2: Distribution of Tensile Damage, $d_t$ , in the Concrete Plug.....	122
Figure 5.6.3: Max Principal Strain Distribution in Cross Beam-Plug Ties.....	123
Figure 5.6.4: Nodes Used for Calculations.....	124
Figure 5.6.5: Moment-Rotation Response Comparison .....	125
Figure A.1: Borehole Locations (Marked With Red) .....	142
Figure A.2: Original SPT Data from Six Boreholes .....	143
Figure A.3: Cross-Beam Details .....	144
Figure A.4: Pile-Cross-Beam Connection Details .....	145
Figure A.5: Cross Beam Stirrup Geometry.....	146
Figure A.6: Cross Beam Rectangular Hoop Geometry .....	146
Figure A.7: Plug to Cross Beam Tie Geometry.....	147
Figure B.1.1: $p$ - $y$ Curves for Soft Clay at Depths of 6, 12, and 18 in. ....	148
Figure B.1.2: $p$ - $y$ Curves for Soft Clay at Depths of 24, 30, and 36 in. ....	148
Figure B.1.3: $p$ - $y$ Curves for Soft Clay at Depths of 42, 48, and 54 in. ....	149
Figure B.1.4: $p$ - $y$ Curves for Soft Clay at Depths of 60, 66, and 72 in. ....	149
Figure B.1.5: $p$ - $y$ Curves for Soft Clay at Depths of 78, 90, and 102 in. ....	150
Figure B.1.6: $p$ - $y$ Curves for Soft Clay at Depths of 114, 120, and 132 in. ....	150
Figure B.2.1: $p$ - $y$ Curves for Medium Clay at Depths of 6, 12, and 18 in.....	151
Figure B.2.2: $p$ - $y$ Curves for Medium Clay at Depths of 24, 30, and 36 in.....	151
Figure B.2.3: $p$ - $y$ Curves for Medium Clay at Depths of 42, 48, and 54 in.....	152
Figure B.2.4: $p$ - $y$ Curves for Medium Clay at Depths of 60, 66, and 72 in.....	152

Figure B.2.5: <i>p-y</i> Curves for Medium Clay at Depths of 78, 90, and 102 in. ....	153
Figure B.2.6: <i>p-y</i> Curves for Medium Clay at Depths of 114, 120, and 132 in. ....	153
Figure B.3.1: <i>p-y</i> Curves for Stiff Clay at Depths of 6, 12, and 18 in. ....	154
Figure B.3.2: <i>p-y</i> Curves for Stiff Clay at Depths of 24, 30, and 36 in. ....	154
Figure B.3.3: <i>p-y</i> Curves for Stiff Clay at Depths of 42, 48, and 54 in. ....	155
Figure B.3.4: <i>p-y</i> Curves for Stiff Clay at Depths of 60, 66, and 72 in. ....	155
Figure B.3.5: <i>p-y</i> Curves for Stiff Clay at Depths of 78, 90, and 102 in. ....	156
Figure B.3.6: <i>p-y</i> Curves for Stiff Clay at Depths of 114, 120, and 132 in. ....	156
Figure B.4.1: Force-Displacement Curves for Soft Clay at Depths of 6, 12, and 18 in. .....	157
Figure B.4.2: Force-Displacement Curves for Soft Clay at Depths of 24, 30, and 36 in. ....	157
Figure B.4.3: Force-Displacement Curves for Soft Clay at Depths of 24, 48, and 54 in. ....	158
Figure B.4.4: Force-Displacement Curves for Soft Clay at Depths of 60, 66, and 72 in. ....	158
Figure B.4.5: Force-Displacement Curves for Soft Clay at Depths of 78, 90, and 102 in. ....	159
Figure B.4.6: Force-Displacement Curves for Soft Clay at Depths of 114, 120, and 132 in. ....	159
Figure B.5.1: Force-Displacement Curves for Medium Clay at Depths of 6, 12, and 18 in. ....	160
Figure B.5.2: Force-Displacement Curves for Medium Clay at Depths of 24, 30, and 36 in. ....	160
Figure B.5.3: Force-Displacement Curves for Medium Clay at Depths of 42, 48, and 54 in. ....	161
Figure B.5.4: Force-Displacement Curves for Medium Clay at Depths of 60, 66, and 72 in. ....	161
Figure B.5.5: Force-Displacement Curves for Medium Clay at Depths of 78, 90, and 102 in. ....	162

<b>Figure B.5.6: Force-Displacement Curves for Medium Clay at Depths of 114, 120, and 132 in.....</b>	<b>162</b>
<b>Figure B.6.1: Force-Displacement Curves for Stiff Clay at Depths of 6, 12, and 18 in. ....</b>	<b>163</b>
<b>Figure B.6.2: Force-Displacement Curves for Stiff Clay at Depths of 114, 120, and 132 in. ....</b>	<b>163</b>
<b>Figure B.6.3: Force-Displacement Curves for Stiff Clay at Depths of 114, 120, and 132 in. ....</b>	<b>164</b>
<b>Figure B.6.4: Force-Displacement Curves for Stiff Clay at Depths of 114, 120, and 132 in. ....</b>	<b>164</b>
<b>Figure B.6.5: Force-Displacement Curves for Stiff Clay at Depths of 114, 120, and 132 in. ....</b>	<b>165</b>
<b>Figure B.6.6: Force-Displacement Curves for Stiff Clay at Depths of 114, 120, and 132 in. ....</b>	<b>165</b>



# **CHAPTER ONE**

## **1. INTRODUCTION**

### **1.1 BACKGROUND**

The Washington State Department of Transportation (WSDOT) developed a bridge seismic retrofit program in 1990 in order to address seismic risk associated with state owned bridges. Nearly 3,000 bridges are constructed on state owned land in Washington, all of which are the responsibility of the WSDOT for maintenance. Many of these bridges were constructed as part of the national interstate program which began in the 1950's. In addition, the majority of the bridges were constructed prior to current seismic design standards. These bridges were constructed using either wood, concrete, prestressed concrete, or steel. Based on bridge deck area, 41 percent of the bridges were constructed using prestressed concrete, 35 percent with reinforced concrete, 23 percent with steel, and the remaining one percent with timber (Kapur, 2006).

A total of 922 bridges are part of the WSDOT seismic retrofit program, which are located on state routes in the western half of the state. As of July 2008, 217 have been completely retrofitted, 153 are partially retrofitted, 32 are under contract or in planning, 12 have been assessed and found to require no retrofit, and 2 have been replaced. Therefore, 506 bridges have not had work performed to assess retrofit needs or implement retrofit strategies (WSDOT, 2008).

Following the magnitude 6.7 Nisqually earthquake in 2001, WSDOT engineers determined that bridges within a 117 km (73 mi.) radius of the epicenter required

inspection, which resulted in 1456 bridges inspected. Upon completion of inspections, 78 bridges were found to have sustained significant damage and 46 of the damaged bridges are maintained and owned by WSDOT. Of the 78 damaged bridges, 36 were reinforced concrete, 20 were prestressed concrete, 16 were steel construction, and six were moveable bridges (Kapur, 2006). Cracking and spalling of cover concrete was the most commonly reported damage documented by WSDOT inspectors.

Hollow prestressed reinforced concrete piles were used as the foundation of many bridges in Washington State during the 1960's. Overall, 22 bridges with hollow-core pile foundations are located on I-5, I-405, and State Route 520 in the Puget Sound region (Kapur, 2006). One of the major deficiencies associated with hollow-core prestressed piles is that they do not provide sufficient ductility for high seismic regions, which is the case in the Puget Sound region. Additionally, sudden, catastrophic failure has been observed in tested piles of this configuration at displacement ductilities ( $\mu_{\Delta}$ ) ranging from 2.5-4.0. The generally observed failure mechanism of tested piles was spalling of the concrete which covers reinforcing steel and prestressing tendons, commonly referred to as cover concrete. Research has also shown that a plastic hinge of roughly one pile diameter ( $1-D$ ) occurs near the pile-to-pile-cap connection at similar displacement ductilities. Traditional retrofit techniques, such as supplying additional confinement and longitudinal reinforcement through the plastic hinge region, have shown to be effective in increasing the shear capacity of hollow piles. However, stiffening the region adjacent to the pile-to-pile-cap connection causes the plastic hinge to form near mid-height of the above ground portion of the pile, reducing displacement ductility in the process.

Currently, no effective retrofitting techniques exist to improve the ductility performance of hollow-core piles.

The objective of this research is to understand the failure mechanisms associated with hollow-core prestressed reinforced concrete piles and the pile-to-cross-beam connections used in constructing the I-5 Ravenna Bridge near Seattle, Washington. The Bridge is located approximately 6.5 km (4 mi.) north of Seattle, Washington, as depicted in Figure 1.1.1.

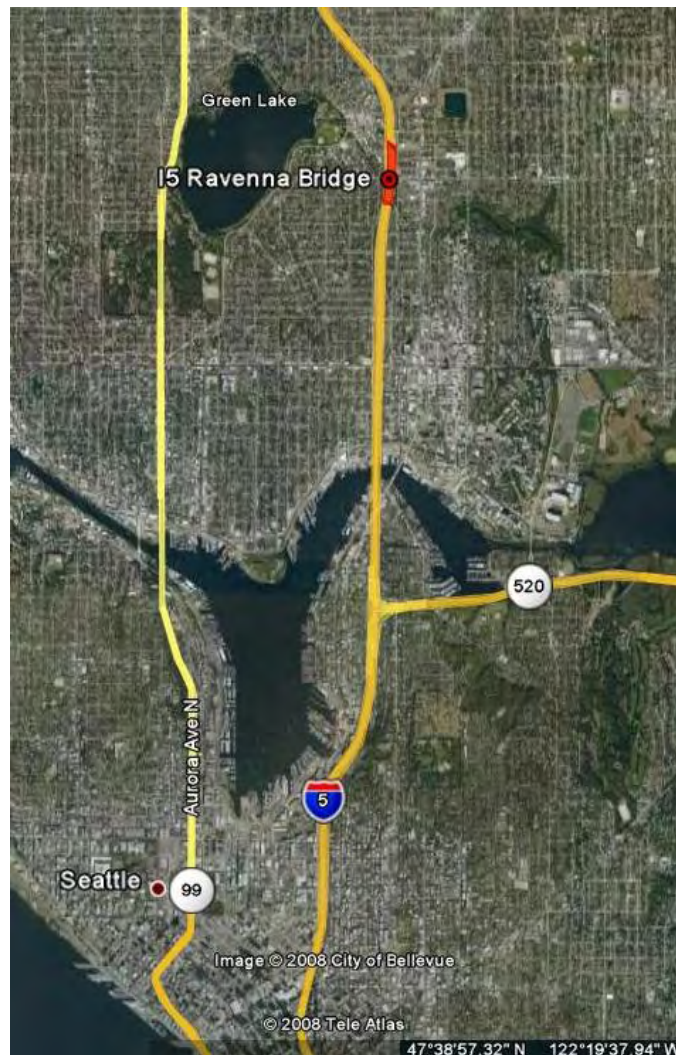


**Figure 1.1.1: Location of I-5 Ravenna Bridge (Google Earth, 2008)**

In order to understand the response of the hollow-core piles, a series of inelastic nonlinear analyses have been performed using two methods. The first is a simplified analytical model using moment-curvature results from XTRACT (TRC/Imbsen Software Systems, Inc., 2001) to define plastic hinge behavior for a beam model generated with SAP2000 (Computers & Structures, Inc., 2007). The second method is a detailed three dimensional finite element model using ABAQUS/Standard (Dassault Systèmes SIMULIA, 2007). To assess the performance of the pile-to-cross-beam connection, only a 3D finite element model was used. With the results of these evaluations, pushover and nonlinear dynamic analyses can be performed to determine retrofit demands for the I-5 Ravenna Bridge, as presented by Shafiei (2008).

## **1.2 RESEARCH OBJECTIVES**

The specific objectives of this research are to:

- Develop a 3D finite element (FE) model and calibrate it to existing experimental data.
- Develop a 2D beam model in SAP2000 Advanced Nonlinear using moment-curvature results from XTRACT to define plastic hinge behavior, and verify performance against experimental results.
- Compare results from the two models and evaluate their ability to predict failure, both qualitatively and quantitatively.
- Develop a model of an *in situ* pile in the I-5 Ravenna Bridge using two soil types in order to understand the influence of confining pressure from the soil on the exterior surface of the pile.

- Determine whether or not confining pressure is great enough such that the cover concrete in the pile behaves as confined concrete.
- Determine the location and length of the subgrade plastic hinge for the *in situ* piles.
- Develop a model of the *in situ* pile-to-cross-beam connection to understand the failure mechanisms and to predict the moment-rotation response of the connection for use in future analyses.

### **1.3 SEISMICITY OF WESTERN WASHINGTON STATE**

The Puget Sound Region of Washington State is located near the boundary of the Juan de Fuca plate and North American plate near the Cascadia Subduction Zone. The two plates are converging at the rate of 3.6 cm/yr (1.4 in./yr), where the Juan de Fuca plate is underthrusting the North American Plate. This subduction zone produces three types of earthquakes: great thrust earthquakes that occur along the plate boundary fault beneath the continental shelf, deep earthquakes in the Juan de Fuca plate where it bends beneath the North American plate, and shallow earthquakes which occur on crustal faults in Western Washington and Oregon (USGS). An overview of the tectonic plate movement in the Cascadia subduction zone is depicted in Figure 1.3.1.

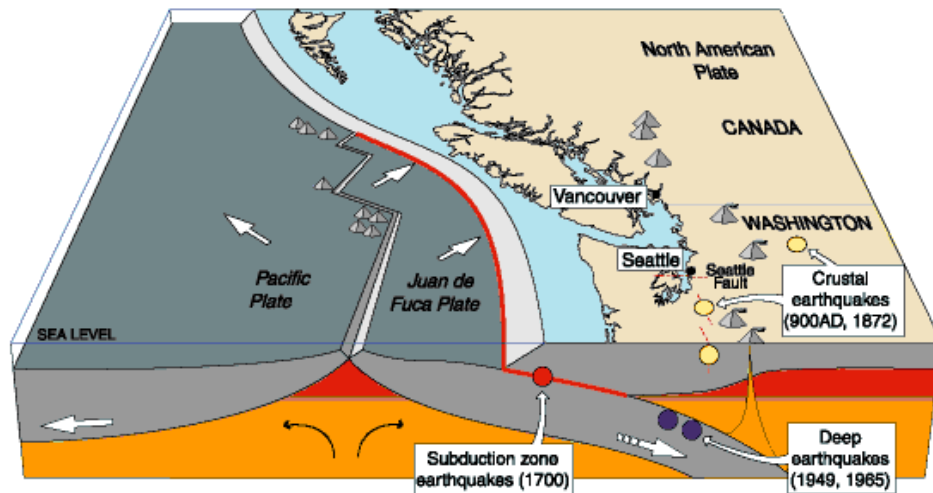


**Figure 1.3.1: Schematic of Cascadia Subduction Zone (USGS, 2002)**

#### **1.4 ORGANIZATION OF THESIS**

This thesis is organized into six chapters. Chapter 2 presents a summary of literature reviewed prior to this work. Chapter 3 first introduces the previously tested piles used to develop and verify the analytical models. It then transitions into a detailed discussion pertaining to development of the XTRACT and SAP2000 models by reviewing the fiber method of cross-section analysis. The 3D finite element analysis is then discussed which is accompanied by a discussion of the constitutive theories employed and a method developed to systematically define the concrete material behavior. Chapter 3 ends with the presentation of results from each analytical model followed by conclusions reached from the analyses. Chapter 4 presents the *in situ* pile modeled using ABAQUS/Standard. The pile geometry, soil types, constitutive theories and material input, mesh, initial conditions, boundary conditions, and loading are discussed in great detail. The chapter concludes with the presentation and discussion of results. Chapter 5 presents the analytical model of the pile-to-cross-beam connection in the I-5 Ravenna Bridge. As with

Chapter 4, all pertinent aspects of the model are discussed in great detail with the exception of the constitutive theories, and it concludes with the presentation and discussion of results. Finally, Chapter 6 summarizes the major conclusions drawn from this study and this thesis closes with recommendations for future research in this area.

## CHAPTER TWO

### 2. LITERATURE REVIEW

#### 2.1 INTRODUCTION

Pile foundations are commonly used for wharves, single and multiple column bent bridges, and high rise buildings which are to be constructed on a soil medium that cannot support the overburden pressure from the superstructure. Moreover, pile foundations are used to transmit loads acting on a superstructure directly to competent soil layers beneath the structure. When the depth to bedrock or stiff soil is vast, piles can be used to gradually transmit the structural load into unstable soils by friction interaction.

Historically, piles have been made of wood, steel, precast reinforced concrete, precast prestressed concrete, or cast-*in situ* piles. Precast concrete piles generally have square, octagonal, or circular cross-sections and can either be solid or hollow-core. Some advantages of concrete piles include resistance to corrosion, easy integration with concrete superstructures, and the ability to withstand large driving forces. Two major disadvantages are difficulties associated with transport and proper cutoff height.

Although a great deal of research has been performed on prestressed and reinforced concrete piles, little research exists pertaining to the response of *in situ* hollow-core precast prestressed reinforced concrete piles under lateral loading. Thus, a deficiency in research exists with respect to confinement of the external pile surface provided by soil and lateral earth pressures. The emphasis of this work is to understand how the response of hollow-core piles is affected when the plastic hinge region is surrounded by various



types of uniform soil media. A thorough literature review of this topic was conducted and is presented in three separate sections. The first section provides an overview of previous experimental work, followed by a discussion of past analytical modeling of concrete piles. Thirdly, concrete constitutive theories are reviewed with key points summarized.

## **2.2 EXPERIMENTAL WORK**

Numerous tests have been performed to study the inelastic behavior of prestressed concrete piles (e.g. Falconer and Park, 1982; Ikeda et al., 1982; Muguruma et al., 1987; Pam et al, 1988; Budek et al., 1997a, 1997b; Budek and Priestley, 2004). The majority of this research was devoted to understanding the effects of varying prestressing force ( $P_s$ ), prestressing steel ratio ( $\rho_{ps}$ ), volumetric transverse reinforcement ratio ( $\rho_t$ ), longitudinal reinforcement ratio ( $\rho_l$ ), and external confinement of the expected plastic hinge region via load apparatus.

In 1982, Ikeda, et al. tested three groups of circular, hollow prestressed piles under monotonic and cyclic lateral loading. Five parameters were varied between the series of tests: transverse reinforcement ratio, non-prestressed longitudinal reinforcement ratio, prestressing steel reinforcement ratio, and prestressing force. In addition, the researchers also tested non-prestressed, reinforced piles where reinforcement was supplied by either deformed bars or unstressed tendons. They observed that all of the prestressed piles exhibited brittle failure at displacement ductilities ( $\mu_\Delta$ ) ranging from 4.0-8.0. The researchers concluded that undesirable brittle failure, which occurred shortly after yield, could be improved by one of two methods. First, to utilize sufficiently close spacing of the transverse reinforcement to provide confinement to the core in order to prevent shear failure, ultimately preventing the pile from reaching its flexural capacity. Second, include

non-prestressed longitudinal reinforcement in order to facilitate ductile behavior after rupture of the prestressing tendons.

Murgurma, et al. (1987) tested thirteen high-strength spun concrete hollow prestressed piles to determine methods for improving ductility. Each specimen contained a fixed number of deformed steel prestressing bars, stressed such that the section prestress remained constant. Transverse reinforcement of the specimens varied from zero to 3% based on the net cross-section area. The researchers observed displacement ductilities ranging from 1.3-2.9, curvature ductilities ( $\mu_\phi$ ) ranging from 1.6-4.8, and set forth three conclusions. First, the flexural capacity can be enhanced significantly by means of high uniform elongation prestressing steel. Second, the level of uniform elongation for the prestressing steel should be taken as the ultimate tensile strain capacity. Third, to avoid fracture of prestressing steel, transverse reinforcement levels must be carefully defined since enhancing ductility via transverse reinforcement can greatly increase tensile demand on prestressing steel.

Six cast-in-place, one third scale piles were tested to investigate the effect of transverse reinforcement and external confinement of the subgrade plastic hinge region (Budek, et al., 1997a). All of the specimens included non-prestressed longitudinal reinforcement, which was not varied through the series of tests. Transverse reinforcement was varied to result in volumetric ratios of 0.3, 0.6, and 0.9 percent. Two piles of each transverse reinforcement ratio were tested. All of the piles were loaded cyclically with either full or no confinement of the plastic hinge region provided by the loading fixture. The test fixture simulated a soil subgrade moment pattern which would be expected over the subgrade plastic hinge region for an *in situ* pile. It was found that the presence of

external confinement essentially negated the effect of increasing the level of volumetric transverse reinforcement. For specimens with unconfined plastic hinge regions,  $\mu_A$  values were reported as 3.0, 4.0, and 5.0 for  $\rho_t$  of 0.3, 0.6, and 0.9 percent, respectively.

Four circular hollow prestressed pile configurations under cyclic loading were tested to investigate the effects of varying the volumetric transverse reinforcement ratio, varying levels of external confinement of the plastic hinge region, and inclusion of non-prestressed longitudinal reinforcement through the expected plastic hinge region (Budek, et al., 1997b; Budek and Priestley, 2004). External confinement was supplied by rubber pads, which lined the loading apparatus. The piles displayed a nearly nonlinear elastic response to cyclic loading and exhibited minimal energy-absorbing hysteretic behavior. Varying external confinement and transverse reinforcement had a negligible influence on displacement capacity. Failure initiated when the core strain reached a value of approximately 0.004 which was violent, abrupt, and concurrent with spalling of the concrete cover. Inclusion of longitudinal rebar through the plastic hinge region did not improve ductility but rather resulted in a significant reduction due to a higher yield displacement and failure at the same concrete strain. The failure mechanism generally observed in the tests was spalling of the concrete cover followed by loss of the compression zone.

Two full scale circular hollow prestressed piles embedded into cohesive soil were tested by Tuladhar, et al. (2007) in order to determine the lateral capacity when subjected to monotonic and reversed cyclic loading. The researchers found that the load carrying capacity of the piles under reversed cyclic loading was roughly 70 percent of the capacity under monotonic loading. It was noted that the degradation in load capacity in reversed

cyclic loading was due to the reduction in the shear stiffness of the clay due to cyclic loading. The location of maximum damage was found to be 600 mm (24 in.) and 1200 mm (48 in.) below ground for the monotonic and reversed cyclic loaded specimens, respectively.

### 2.3 ANALYTICAL MODELING

In 1997, researchers performed a series of nonlinear inelastic finite-element analyses on hollow prestressed pile foundations modeled as Winkler beams (Budek, et al., 1997c). Moment-curvature analyses were performed to a core failure strain of 0.004. The hollow piles were analyzed using a bilinear soil model and three above grade heights; 0, 5, and 10- $D$ ,  $D$  being the pile diameter of 1.22 m (48 in). Axial loads varying from zero to  $0.4f_c'A_g$  were applied to each analysis, where  $f_c'$  is the concrete compressive strength and  $A_g$  is the gross area of the cross section. The prestressed piles exhibited limited ductility which was severely degraded at high levels of axial load. The authors concluded that axial loads should be kept at or lower than  $0.2f_c'A_g$ .

In order to investigate the response of a solid reinforced concrete pile in cohesionless soil, inelastic finite element analyses were performed (Budek et al., 2000). Specifically, researchers set out to determine ductility capacity and identify parameters which influenced equivalent depth to fixity, depth to maximum moment, and equivalent plastic hinge length. The pile was modeled as a Winkler beam on an elastic foundation and nonlinear behavior of the pile section was defined using a moment-curvature relationship. The parameters that were varied throughout the analyses included pile head boundary conditions, above ground height, and soil stiffness. The soil spring stiffnesses were

prescribed using linear, bilinear, and hyperbolic formulations. The researchers set forth the following conclusions:

- Above ground height and soil stiffness mildly influence ductility capacity.
- Shear is significantly underpredicted by elastic analysis since inelastic behavior influences the location of the maximum moment.
- The location of maximum moment and the plastic hinge length are adversely affected by soil stiffness, and in the case of fixed-head piles, above ground height.
- Linear soil models were deemed appropriate for most pile/column design.

In 2002, an extended equivalent cantilever model was proposed to investigate the inelastic response due to inertial loading for solid reinforced concrete piles in cohesive and cohesionless soils (Chai, 2002). Researchers developed the model by adapting the equivalent cantilever model in an elastic soil-pile system (Poulos and Davis, 1980; Pender, 1993) to inelastic soil-pile systems. The elastic soil-pile system is used to determine the equivalent depth to fixity by equating the soil-pile system and equivalent cantilever lateral stiffnesses. To include inelastic behavior, the maximum moment is assumed to occur at some depth above the depth-to-fixity. In doing so, the lateral strength of the pile, a function of the depth to maximum moment, can be determined from the ultimate pressure distribution of the soil and the flexural strength of the pile. Assuming that the plastic hinge rotation is concentrated at the location of maximum moment, a kinematic relationship between the local curvature ductility demand and global displacement ductility demand was developed. It was shown that the proposed kinematic relationship was dependent on four parameters: the depth to maximum moment,

equivalent depth to fixity, above ground height, and equivalent plastic hinge length. The authors concluded that the analytical model provides reasonable estimations for local curvature ductility when compared to experimental results (Chai and Hutchinson, 2002), but overpredictions can result if the value for the rate of increase of the horizontal subgrade reaction modulus is not carefully selected.

In an attempt to incorporate Performance-Based Seismic Engineering (PBSE) aspects to the design of reinforced concrete piles and drilled shaft bents, a simple analytical model was developed (Suarez, 2005) using guidelines set forth by Chai (2002). Nonlinear static analyses were carried out for single solid reinforced concrete columns embedded in sand and clay. Nonlinear behavior was incorporated in the soil and pile, and boundary conditions at the column head were specified as pinned or fixed. Results from the nonlinear static analyses provided predictions for target displacement, ductility demand, and plastic hinge location which were used in development of the analytical model. The author concluded the following:

- For a given soil type, equivalent length increases with column diameter and bent height.
- For a given soil type and bent height, yield displacement is increased when pile diameter is increased.
- For a given bent height, displacement limit, and column diameter, the influence of soil type was summarized as follows: softer soils will result in a larger equivalent length and yield displacement while reducing ductility demand compared to behavior in stiff soils.

In 2007, Tuladhar, et al. performed a series of 3D nonlinear finite element analyses to analytically investigate the behavior of experimentally tested specimens. Nonlinearity of the concrete prior to cracking was defined using an elasto-plastic fracture model, and post cracking behavior was incorporated using a smeared crack model. The behavior of the soil was separated into deviatoric and volumetric components. The volumetric behavior was assumed as linear elastic while the deviatoric component was modeled using a nonlinear Ohasaki model. The soil-pile interaction was modeled using a 16-node interface element in order to allow for active and passive behavior between the soil and pile. The researchers concluded that the formation of the gap between the soil and pile had a significant effect on pile performance. In addition, if the bentonite-cement slurry used for boring is not included in the analytical model, the lateral load capacity of the pile is overestimated. Overall, it was determined that the finite element model could realistically account for the formation of the gap between the soil and pile, and it provided accurate predictions for pile response when compared to experimental results.

## **2.4 CONCRETE CONSTITUTIVE MODELS**

A vast amount of literature pertaining to concrete constitutive modeling exists. Many of the constitutive models in existence have been defined using one of four methods: (1) representing stress-strain behavior in terms of mathematical functions or fitted curves, (2) using linear elastic and nonlinear elastic theories, (3) via perfect plasticity and work-hardening plasticity theories, and (4) by means of the endochronic, or intrinsic, theory of plasticity. Existing concrete constitutive models based on all four abovementioned methodologies are summarized by Chen (2007) and are briefly described.

#### 2.4.1 LINEAR AND NONLINEAR ELASTICITY

Linear elastic theory is the most common behavior used to describe the pre- and post-failure region of the stress-strain behavior for concrete. Linear elastic formulation, however, is unable to predict inelastic deformations due to excessive loading, unloading, or load-history and rate effects such as creep and viscoplastic deformations. Linear elastic models can be significantly improved when nonlinear elastic behavior is considered. The two most prominent nonlinear elastic formulations are based on *hyperelasticity* or *hypoelasticity*. In the case of hyperelasticity, the stress-strain behavior is derived from a strain energy density function which is strain rate independent. The hyperelastic formulation results in a path-independent approximation for material stress-strain behavior which is reversible. As with a linear elastic model, constitutive models derived using the concepts of hyperelasticity fail to allow for inelastic deformation unless unloading criteria are defined. Hypoelastic formulations typically express the state of stress in a material as a function of the state of strain and the stress path followed to reach the current state. Conversely, stress-strain behavior as described by hypoelastic formulation is path-dependent and can be incrementally reversible. Simply put, hypoelastic formulation requires that the state of stress at any given time is dependent on the state of strain at a particular instance and the stress path followed to reach the current state. This is commonly referred to as an *incremental* or *differential* material description. The hypoelastic formulation, being an incremental description, leads to two inherent difficulties in creating the constitutive definition. The first is that the material stiffness matrix must be formulated for each incremental state of stress and strain. The second is that under multiaxial stresses, loading in shear may result in unloading of normal



components of stress which further requires a unique definition of loading and unloading behavior. Regardless of whether a linear or nonlinear elastic formulation is used to describe the stress-strain behavior of concrete, failure criteria for tensile and compressive behavior must also be incorporated to reasonably approximate material behavior.

#### *2.4.2 PERFECT PLASTICITY*

It is commonly known that when concrete is loaded in triaxial compression it experiences flow, similar to ductile materials, along the yield or failure surface before ultimate compressive strains are reached. It is for this reason that elastic-perfectly-plastic constitutive models were introduced. The perfectly plastic model assumes that concrete under triaxial compression can flow along the yield surface until the fracture surface is reached. The assumption that concrete fails completely when ultimate compressive strain within a continuum is achieved is a rough approximation to the material response, but reasonable in the case of a perfectly plastic model. Furthermore, the aforesaid definition of failure implies a brittle fracture behavior. The elastic-perfectly-plastic brittle-fracture model can thus be described as three regions: behavior prior to yielding, plastic flow after yielding, and post-fracture behavior. Material behavior in the pre-yielding and post-fracture regimes has commonly been described using a linear elastic formulation which implies that only the plastic flow regime requires definition. In order to define the plastic flow region, a definition of yield and fracture must be defined. Yielding in concrete is typically defined using von Mises, Drucker-Prager (extended von Mises), Coulomb, or modified Coulomb criteria. Furthermore, a common assumption for concrete modeling is that the failure surface is coincident to the yield surface, thus defining perfectly plastic deformation after yielding. To formulate the stress-strain behavior during plastic

deformation, one must prescribe a flow rule. In general, the flow rule is defined as the plastic-deformation-rate vector normal to the yield surface. This definition of the flow rule implies that under plastic deformation, the material will dilate due to an increase in plastic volume under pressure. Furthermore, if plastic deformation is defined based on the aforesaid assumptions, a material is said to abide by an *associated flow rule*. If one opts to assume that the plastic-deformation-rate vector is oblique to the yield surface, a material is said to abide by a *nonassociated flow rule*. The assumption as to whether concrete should be defined using the associated flow rule rather than a nonassociated flow rule has been a highly controversial topic in numerical modeling of materials (Chen, 2007). However, due to the lack of evidence supporting nonassociated flow, it is generally accepted in practice that plastic deformation in concrete follows the associated flow rule.

#### 2.4.3 WORK-HARDENING PLASTICITY

The work-hardening theory of plasticity is considered to be a generalization of the elastic and perfectly-plastic material definitions in the sense that concrete can be represented as an elasto-plastic material through the use of *loading surfaces*. The loading surface replaces the initial yield surface by combining perfect plasticity with strain hardening effects. The work-hardening theory of plasticity defines the initial yield surface based on von Mises, Drucker-Prager, Coulomb, or extended Coulomb yield criteria, thus specifying the elastic limit. An assumed associated flow rule is used to define plastic deformation and the subsequent new yield surfaces, typically referred to as loading surfaces. Therefore, when the state of stress is such that it lies within the elastic limit surface, elastic theory can be applied. When the state of stress exceeds the elastic limit

surface, the initial yield surface is replaced by a loading surface which can be used for determining irrecoverable deformations in the event of unloading and reloading. For example, if a material is loaded beyond the elastic limit, a loading surface is defined to maintain the state of plastic deformation. If the material is then unloaded and reloaded within the new yield surface, no additional plastic deformation will be experienced.

In order to determine failure, a fracture surface is formulated in terms of fracture and crushing strains to account for both tensile and compressive behavior. The fracture surface is the outermost bounding surface of material behavior and it should be noted that all loading surfaces which are generated during unloading and reloading of the material must lie between the initial yield and fracture surfaces. Another important note is that stress-softening effects are not considered based on the work-hardening theory of plasticity described thus far. In order to do so, it is commonly assumed that once the failure surface has been reached, it begins to collapse, signifying material softening.

#### *2.4.4 ENDOCHRONIC PLASTICITY*

The endochronic theory of plasticity, or incremental-flow theory, is essentially an extension of the work-hardening theory of plasticity. It assumes that an initial yield surface and hardening rule define subsequent loading surfaces. The assumption that the initial yield surface is coupled with a hardening rule allows for loading, unloading, and reloading to be dealt with in separate steps, resulting in a discontinuous material model. The major strength of this theory is that it utilizes intrinsic time, which can be used to describe the incremental change in the material since the constitutive model is expressed in differential form.

## CHAPTER THREE

### 3. MODEL CALIBRATION

#### 3.1 PILE DESCRIPTION

The finite element model proposed in this chapter was generated in an attempt to reproduce the response of the specimens denoted by Budek, et al. (1997b) as PS12 and PS13. A brief summary of the pile specifications and loading devices follows.

An overview of the testing apparatus is provided in Figure 3.1.1. The test fixture was assembled such that the pile could be considered as a simply supported flexure member. The concrete compressive strength for both piles was approximately 67 MPa (9700 psi). The piles measured 7315 mm (288 in.) in overall length, 6100 mm (240 in.) between supports. The pile was constructed with a 610 mm (24 in.) outer diameter and 422 mm (16.6 in.) inner diameter, resulting in a wall thickness of 94 mm (3.7 in.).

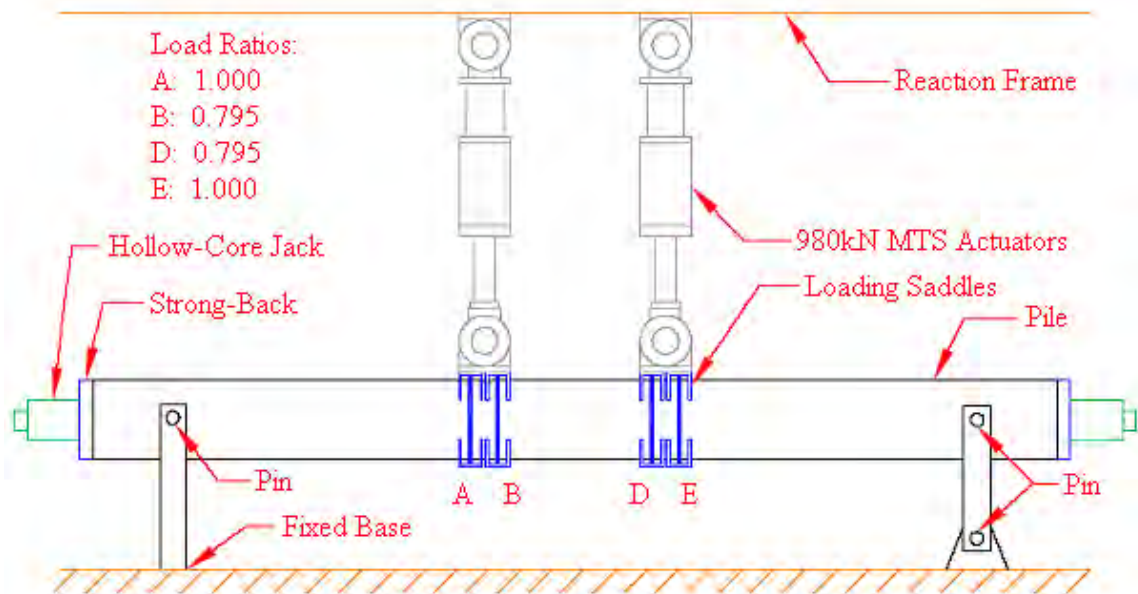


Figure 3.1.1: Arrangement of Test Apparatus

Transverse shear reinforcement was supplied by a 515.7 mm (20.3 in.) diameter W8 A82 wire spiral pitched at 76 mm (3 in.), resulting in 41 mm (1.6 in.) of cover concrete and a nominal transverse reinforcement ratio of 0.2 percent. The yield and ultimate strength of the transverse reinforcing steel were reported as 647 MPa (94 ksi) and 816 MPa (118 ksi), respectively. Prestressing steel consisted of sixteen 12.7 mm (0.5 in.) 7-wire strands stressed at 744 MPa (108 ksi) after losses. The yield and ultimate strength of the prestressing strands were reported as 1585 MPa (230 ksi) and 1860 MPa (270 ksi), respectively. The sole difference between the two specimens was the inclusion of longitudinal reinforcement through the plastic hinge region of PS13 using eight M#13 455 MPa (#4 Gr. 60 ksi) nominal yield strength rebars.

A whiffle tree loading apparatus with two actuators was used to simulate the moment pattern expected from lateral earth pressure on the pile. Loading saddles were lined with rubber pads, which were selected to simulate the soil subgrade reaction modulus. An externally applied axial load was supplied to produce a nominal value of  $0.12f_c'A_g$ . It should be noted that the models discussed in this chapter were generated using the International System of units (N, mm, s).

## **3.2 XTRACT**

### *3.2.1 INTRODUCTION*

XTRACT (TRC/Imbsen Software Systems, Inc., 2001) is a commercially available software package for moment-curvature analysis. It utilizes two dimensional discretization of a cross-section to determine stress, strain, and moment by incrementally increasing the curvature applied to the cross-section. One important assumption is a linear distribution of strain through the cross-section. Since the curvature of the cross-

section is known for each increment, the strain in each discrete area can be computed. Once the strain is known for each discrete area, stresses are determined from the user specified uniaxial stress-strain data for the materials used. Once the stress in each discrete area is known, the resultant force in each area can be computed for the cross-section. Using an iterative solution process, the neutral axis can then be located using a force balance. Finally, once the resultant force and the moment arm to the neutral axis are known for each discretized area, the total moment in the cross-section can be computed. Thus, the moment-curvature response of a cross-section is computed.

### 3.2.2 MODEL FORMULATION

The pile cross-section was modeled to the specifications detailed in the Section 3.1. Nominal properties of the steel models used are predefined options available in XTRACT. Prestressing steel was defined using the high strength prestressing steel model with nominal properties corresponding to A416 Gr. 270 ksi steel. Longitudinal rebar was defined using a bilinear steel model with strain hardening and nominal properties of A615 Gr. 60 ksi steel.

In order to fully define the concrete in the model, the tensile strength, elastic modulus, yield stress, crushing, spalling, and failure strains must be supplied. Stress and strain values at yield, maximum compressive stress, and ultimate compressive stress were obtained from a standard reference (Collins and Mitchell, 1991). The elastic modulus was defined using Equation 3-1, a metric conversion of the equation per ACI318-05.

$$E_c = 4733\sqrt{f'_c} \quad (3-1)$$

where:

$$f'_c = \text{Unconfined concrete compressive strength (MPa)}$$

The tensile strength, taken as the cylinder splitting strength defined by Iravani (1996), is presented in Equation 3-2, with  $f_c'$  as previously defined.

$$f_{sp}' = 0.57\sqrt{f_c'} \quad (3-2)$$

Based on the results from Budek, et al. (1997b), it was observed that sudden catastrophic failure of the pile specimen occurred shortly after cover concrete began to spall. Therefore, the spalling strain is an important indicator of failure and both it and crushing strain were taken as  $\varepsilon_{cu} = 0.0027$  from recommendations by Bae and Bayrak (2003). The strain at which the analysis was terminated, the failure strain, was thus defined as 0.003.

Moment-curvature analysis was carried out until the failure strain of 0.003 was achieved. Loading for the cross-sectional analysis was applied in the form of a constant 890 kN (200 kips) initially applied axial load with an incrementing moment about the x-axis.

### 3.2.3 XTRACT RESULTS

The section behavior at failure for the XTRACT models of PS12 and PS13 is shown in Figure 3.2.1 and Figure 3.2.2, respectively. Note that the overall performance of the model was governed by the tensile behavior of the concrete. Once tensile cracks form through the wall thickness, the size of the compression zone rapidly decreases as moment about the  $x$ -axis is increased. Results from the analysis show that once the compressive region was reduced to the extent that the compressive peak fiber strain is equivalent to the spalling strain, failure occurs. Moreover, the analysis becomes unstable and is terminated once concrete spalls to a depth roughly equivalent to the depth of cover, as illustrated in Figure 3.2.1 and Figure 3.2.2.

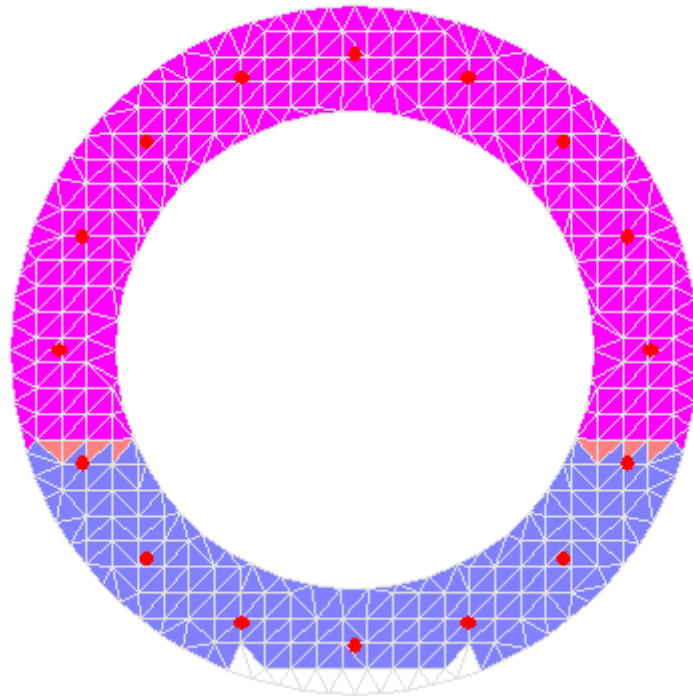
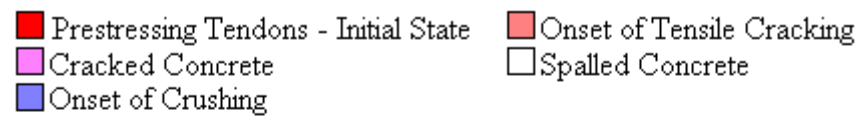


**Figure 3.2.1: Stress at Failure for Specimen PS12**



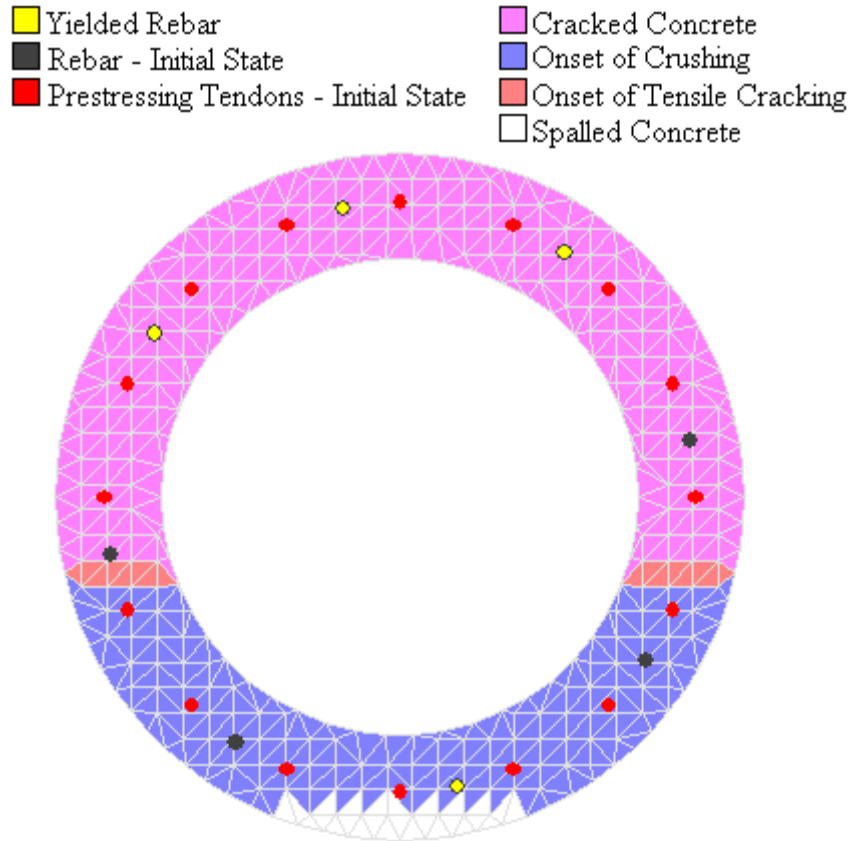


**Figure 3.2.2: Stress at Failure for Specimen PS13**

The moment-curvature ductility response for specimen PS12 is given in Figure 3.2.3, compared with results transcribed from hysteretic curves reported by Budek, et al (1997b). It should be noted that, in the experimental work, the yield curvature values for specimens PS12 and PS13 were defined as  $0.0065 \text{ m}^{-1}$  ( $0.0019 \text{ ft}^{-1}$ ) and  $0.007 \text{ m}^{-1}$  ( $0.0021 \text{ ft}^{-1}$ ), respectively. Curvature ductility is defined as the ratio of the curvature of the cross-section at any time,  $t$ , to curvature at yielding. Upon examination of the plot, one will see that XTRACT is able to accurately capture the elastic response of specimen PS12. Once curvature ductility of approximately 0.3 is reached, the results from the predictive model begin to diverge from those of Budek, et al (1997b). It is important to note that the moment predicted for failure was within eight percent of that observed in the test. The

model predicted only about half of the ultimate curvature ductility of the test, but damage from the cyclic loading of the test may have led to reduced stiffness after initial cracking that was not considered in the model. The variation in the response for hollow core piles of similar configurations subjected to cyclic and monotonic loading is presented in Figure 3.2.4 (Tuladhar et al., 2007). Upon inspection of Figure 3.2.4, one can see that for a cyclically loaded pile the load carrying capacity and displacement ductility are reduced by roughly 30 percent and 50 percent, respectively, when compared to monotonic loading.

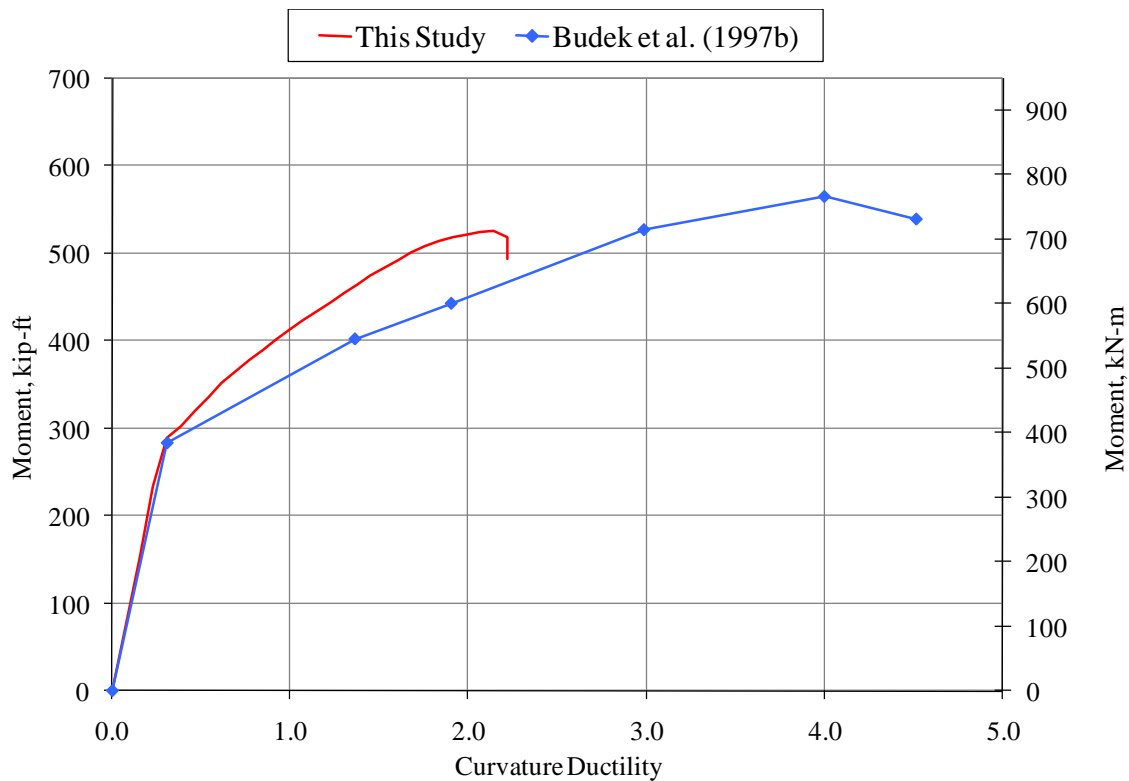


**Figure 3.2.3: Comparison of XTRACT and Test Results for Specimen PS12**

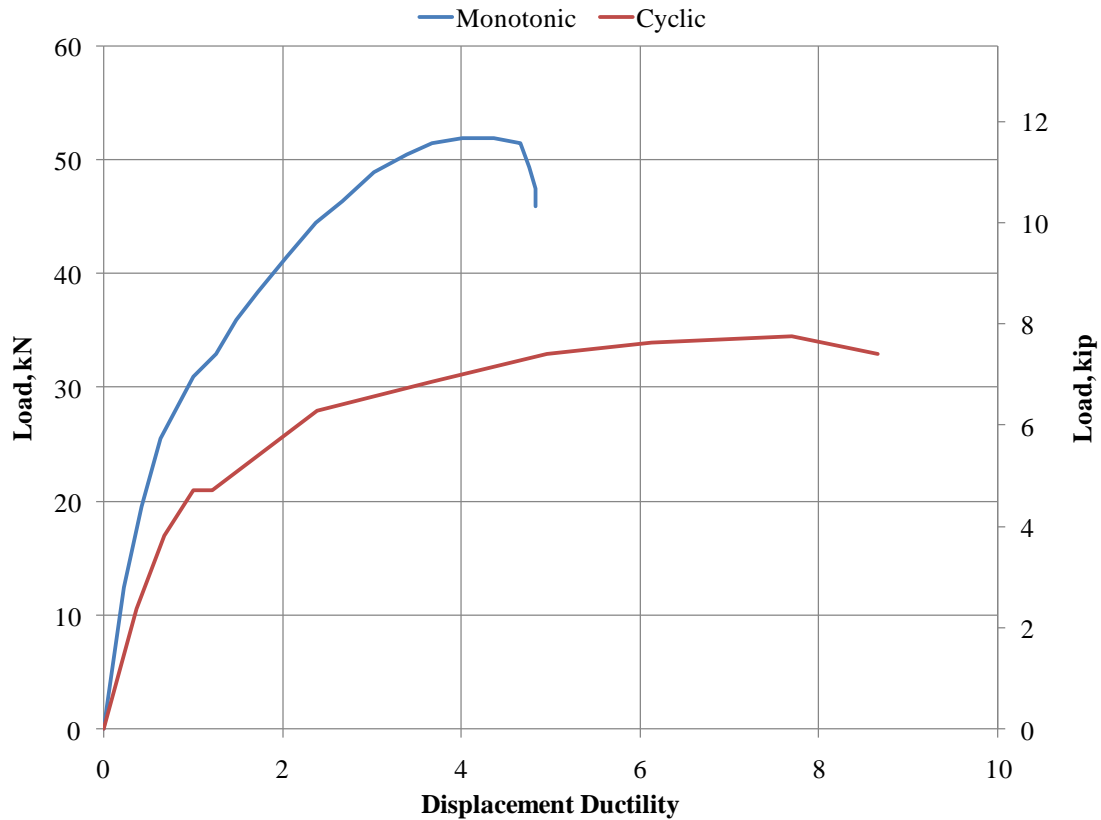


**Figure 3.2.4: Effect of Cyclic Loading on Pile Response**

The section behavior at failure of the XTRACT model for specimen PS13 was nearly identical to that of PS12. Similar to the XTRACT model for specimen PS12, performance was governed by the tensile capacity of the concrete. Failure of specimen PS13 occurred when the peak fiber strain was equivalent to the spalling strain. At that juncture, the depth of spalling was roughly equivalent to the depth of concrete cover. In addition, the model became unstable and the analysis was terminated. The moment-curvature ductility response of specimen PS13 is provided in Figure 3.2.5, again compared to the results of from Budek, et al. (1997b). Much closer agreement was obtained, possibly due to reduced concrete damage during cyclic loading with the added reinforcement. Examination of the plot illustrates the fact that the model is able to reasonably capture the elastic and inelastic response of the pile. Analytical results for the moment capacity and

curvature ductility are accurately predicted up to  $\mu_\phi = 2.0$ , the instance at which softening, followed by failure, would occur.

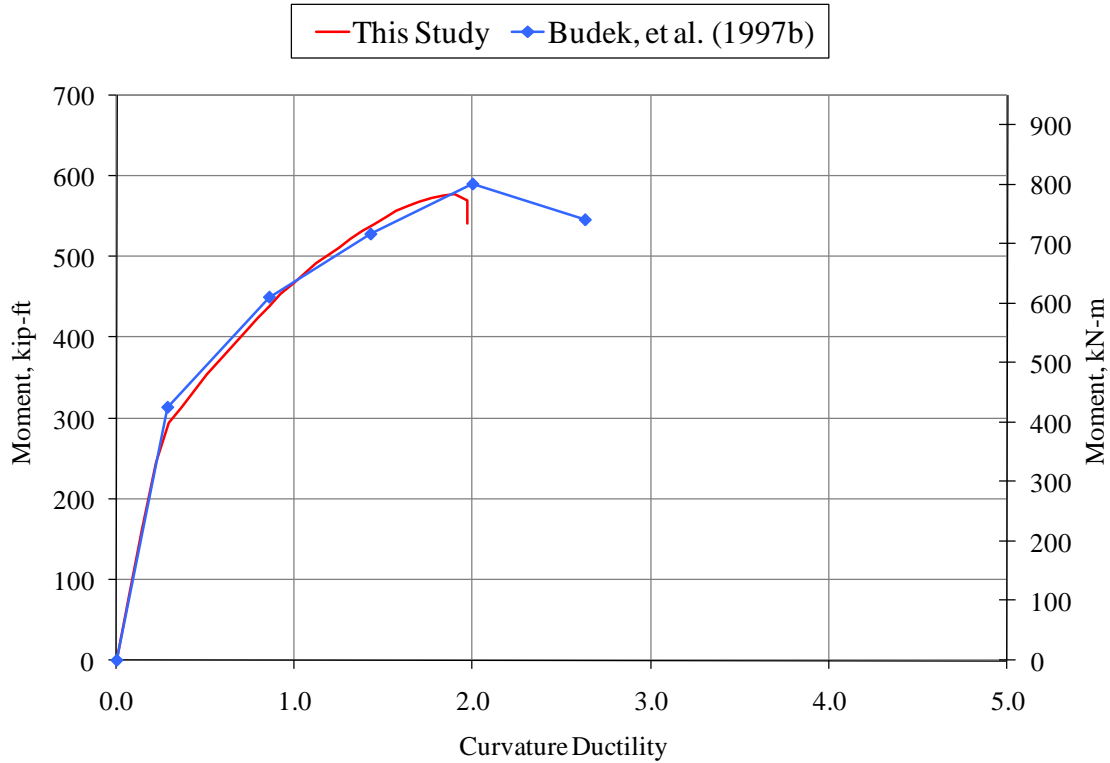


**Figure 3.2.5: Comparison of XTRACT and Test Results for Specimen PS13**

### 3.3 ABAQUS/STANDARD

#### 3.3.1 INTRODUCTION

In order to qualitatively understand failure mechanisms and quantify the onset of failure, static analyses of three dimensional pile models were performed using ABAQUS/Standard version 6.7 (Dassault Systèmes SIMULIA, 2007). Constitutive theories used in development of the finite element models are available in the

ABAQUS/Standard material library and are described in the ABAQUS user's manual (Dassault Systèmes SIMULIA, 2007).

Two concrete constitutive models are available in ABAQUS/Standard version 6.7: the concrete smeared cracking model and a damaged plasticity model. Both models were developed using the endochronic theory of plasticity, or incremental-flow theory, as discussed in Chapter 2. The concrete smeared cracking model is intended to be used for relatively low rates of monotonic loading at low confining stresses, and it is assumed that the predominant failure modes are compressive crushing and tensile cracking. In this constitutive model, associated flow is assumed and cracks are considered to be irrecoverable once formed.

The damaged plasticity model presented in the ABAQUS user's manual (2007) utilizes additive strain rate decomposition of the elastic and inelastic portions of strain to obtain the total strain rate. The yield function is defined based on the methodologies proposed by Lubliner, et al. (1989) and by Lee and Fenves (1998). The flow rule is assumed to be nonassociated, thus characterizing plastic flow by flow potential. The stress-strain relationships for tensile and compressive behavior are defined in terms of scalar damaged elasticity. The scalar damage value, specified by the user, defines the degradation of initial elastic stiffness based on the state of inelastic tensile and compressive strain. Damaged material states in tension and compression are handled by independent hardening laws defined in terms of equivalent plastic strain. Compression hardening is provided in terms of compressive stress as a function of inelastic strain and the inelastic compressive strain rate.

The post-cracking tensile stress-strain behavior can be characterized using one of three methods: (1) specifying stress as a tabular function of inelastic strain, (2) specifying stress as a tabular function of crack width or, (3) specifying stress as a tabular function of fracture energy associated with the initiation of cracking. The first method is primarily used when a concrete body has significant amounts of reinforcing steel since mesh sensitivity can become problematic. The reason for the mesh sensitivity is that failure can often occur in localized regions of unreinforced concrete. Consequently, if the mesh is refined, narrower cracking bands will result in energy dissipation that depends on element size, causing the finite element predictions to fail to converge to a unique solution. Therefore, if a concrete body has reinforcement sufficient enough to evenly distribute cracking, mesh sensitivity is less of a concern and post-cracking tensile behavior can be characterized using tabular stress and inelastic strain data. For analysis of concrete bodies that are not heavily reinforced, it is suggested that either the second or third previously mentioned methods be used (Dassault Systèmes SIMULIA, 2007). For this work, stress was specified as a tabular function of fracture energy.

Fracture energy of materials was first conceived by Alan Griffith in 1920. Griffith proposed that the change in strain energy within a body due to crack propagation could be equated to the increase in surface energy due to increased crack surface area. Between the late 1930's and 1960's, a great deal of research was conducted to improve this model in an attempt to incorporate the effects of cohesion within materials and frictional forces between the newly formed fracture surfaces. Much of the research was based on linear elastic fracture mechanics (LEFM). Arne Hillerborg (1967) proposed a fracture model in which the crack could be defined using two distinct zones: (1) the physical crack

surfaces where no stress is transferred between the newly formed surfaces and, (2) a damaged zone at the crack tip where stresses are transferred. Hillerborg defined the fracture energy of a brittle material as the energy required to open a crack of unit area. He later proposed in 1985 that a simple three point bending test of a notched beam would allow one to quantify the fracture energy of a brittle material by calculating the area under the force-crack-mouth-opening-displacement (CMOD) curve. The method for determining fracture energy based on LEFM for high strength concrete is outlined by Shah (1990). Note that this method is commonly referred to as the work-of-fracture method, and the *total* fracture energy is denoted by  $G_F$ .

In order to define fracture energy as a material property, the calculation of fracture energy must be independent of specimen size. Bažant (1984) introduced a size effect law that accounts for the brittleness of a material and allows one to separate size effects from other influences in brittle fracture. One should note that the fracture energy determined using the size effect method (SEM), is denoted by  $G_f$ , and is often referred to as the *initial* fracture energy.

Jenq and Shah (1985) introduced a two parameter fracture model (TPFM) for concrete to accurately determine the critical stress intensity factor in order to account for size effects when determining fracture energy. The TPFM is based on the so-called compliance measurement, which is defined as the value of the CMOD per unit applied load. Many researchers have tested plain concrete sections in order to determine the total fracture energy based on Hillerborg's proposal and initial fracture energy based on the SEM or TPFM (e.g. Gettu, et al., 1990; Darwin, et al., 2001; Appa Rao and Raghu Prasad, 2002; Ensfield and Velasco, 2006; Roesler, et al., 2007; Martin, et al., 2007).

Four general conclusions were drawn from the aforementioned researchers: (1) fracture energy increases as concrete compressive strength increases, (2) fracture energy increases as coarse aggregate strength increases, (3) as compressive strength increases, concrete becomes more brittle, and (4) as maximum coarse aggregate size is increased, ductility of the concrete mixture increases.

### 3.3.2 *MODEL FORMULATION*

#### 3.3.2.1 Concrete Properties

Material assumptions for the pile concrete utilized the density, elastic, and concrete damaged plasticity models defined in the ABAQUS material library. Unit weight of the concrete was taken as  $22.8 \text{ kN/m}^3$  ( $145 \text{ lb}_f/\text{ft}^3$ ). The elastic properties were defined by a Poisson's ratio of 0.15 and Young's modulus of 38741 MPa (5619 ksi) from Equation 3-1. The concrete damaged plasticity option was used to define the yield surface, viscosity parameters, and flow potential for plastic behavior. In addition, the concrete compression and concrete tension damage options were also incorporated in the constitutive model to simulate damage of the concrete due to tensile cracking and compressive crushing.

Five parameters are required to fully describe the damaged plasticity model: the dilation angle in degrees, the flow potential eccentricity, the ratio of initial equibiaxial compressive yield stress to initial uniaxial compressive yield stress, the ratio of the second stress invariant on the tensile meridian to that on the compressive meridian, and the viscosity parameter that defines visco-plastic regularization (Dassault Systèmes SIMULIA, 2007). The aforementioned parameters were set to  $15^\circ$ , 0.1, 1.16, 0.66, and 0.01, respectively, as recommended (Dassault Systèmes SIMULIA, 2007).



Compression behavior of the concrete was defined by compressive stress and corresponding inelastic strain data. Stress-strain data was obtained by selecting four points from a typical stress strain curve (Collins and Mitchell, 1991). The four points selected correspond to yield, maximum compressive stress, ultimate compressive stress, and ~7 percent of maximum compressive stress, which defined the concrete behavior after crushing. A complete loss of strength in compression was not considered, primarily to avoid any potential convergence issues that would arise once compressive stress reached zero in a given element. Strain values obtained from the stress-strain curve were then defined in terms of plastic strain by subtracting the strain at yield from the values of total strain. An example of the idealized stress-strain definition is provided in Figure 3.3.1. The last two points defining the idealized curve in Figure 3.3.1 were selected to facilitate solution convergence. Dashed lines in Figure 3.3.1 represent stiffness degradation (moduli  $E_1$ ,  $E_2$ , and  $E_3$ ) in terms of compressive damage ( $d_c$ ), which is discussed later.

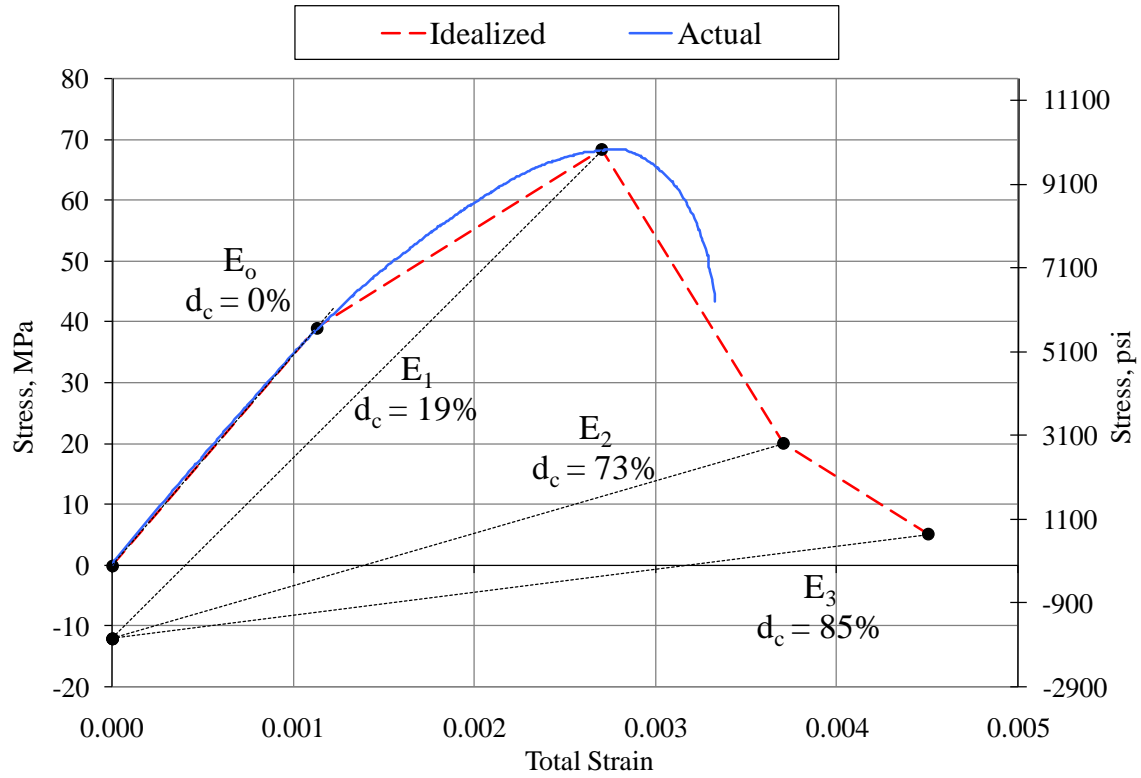


**Figure 3.3.1: Idealized Compressive Stress-Strain Relationship**

Tensile behavior of the concrete was defined using a fracture energy cracking criterion since significant regions of the models do not contain reinforcing steel. In this case, the brittle behavior of concrete is described using a stress-displacement relationship based on Hillerborg's (1976) fracture energy proposal, which defines fracture energy,  $G_f$ , as the energy required to open a crack of unit area. The fracture energy cracking model available in ABAQUS can be invoked in two ways: specifying fracture energy as a material property in which tensile stress is a linear tabular function of fracture energy, or specifying postfailure stress as a tabular function of crack displacement (SIMULIA, 2007). The former definition was used in development of the PS12 and PS13 FEA models. The use of the selected definition for tensile behavior requires the following three parameters: fracture energy, tensile stress associated with initiation of cracking ( $f_{sp}$ ),

and the crack opening displacement at which a complete loss of strength is specified to occur ( $u_0$ ). A schematic of the tensile stress-displacement relationship is presented in Figure 3.3.2.

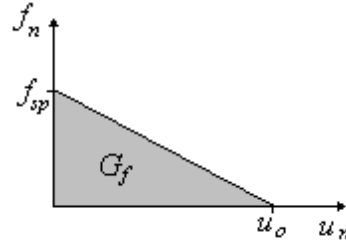


**Figure 3.3.2: Tensile Stress-Displacement Behavior**

To determine the fracture energy associated with the 67 MPa (9700 psi) concrete, a fracture mechanics approach was used. From fracture mechanics in plane stress applications (Roesler, et al., 2007), fracture energy is defined in Equation 3-3 as:

$$G_f = \frac{K_{if}^2}{E} \quad (3-3)$$

where:

$G_f$  = Fracture energy required to initiate tensile cracking (Force/Length)

$K_{if}$  = Stress intensity factor for a plate of infinite size (Force/Length<sup>3/2</sup>)

$E = E_c$  = Elastic modulus for concrete (Force/Length<sup>2</sup>)

The stress intensity factor for a plate of infinite size (Boresi, 1993) is defined by Equation 3-4:

$$K_{if} = 1.12\sigma\sqrt{\pi a} \quad (3-4)$$

where:

$\sigma = f_{sp}$  = Concrete cylinder splitting strength (Force/Length<sup>2</sup>)

$a$  = Crack depth (Length)

Equations 3-3 and 3-4 are applicable for any consistent set of units. The elastic modulus of concrete and the tensile splitting strength were calculated per Equations 3-1 and 3-2, respectively. The crack depth used to define the stress intensity factor was taken as 43 mm (1.69 in.) which corresponds to the depth of concrete cover to transverse reinforcing steel. The resulting calculated value of fracture energy was 0.095 N/mm (0.542 lb<sub>f</sub>/in.). It was found that the calculated value for  $G_f$  agreed with results presented by Roesler, et al. (2007), Darwin, et al. (2001), Appa Rao and Raghu Prasad (2002), and Einsfeld and Velasco (2006) for concrete mixes of similar design strength. Using the calculated values for fracture energy and concrete cylinder splitting strength, the crack displacement associated with complete loss of tensile capacity,  $u_o$ , was calculated from Equation 3-5. The resulting crack displacement was calculated as 0.041 mm ( $1.61 \times 10^{-3}$  in.).

$$u_o = \frac{2G_f}{f_{sp}} \quad (3-5)$$

Compression damage of the concrete is prescribed by tabular data which specifies the decimal percentage of stiffness degradation at corresponding values of plastic strain. Values of stiffness degradation,  $d_c$ , were calculated via Equation 3-6. A graphic representation of stiffness degradation can be viewed in Figure 3.3.1 represented by moduli  $E_1$ ,  $E_2$ , and  $E_3$ .

$$d_c = 1 - \frac{E_n}{E_o} \quad (3-6)$$

Where:

$E_n = E_1, E_2, E_3$  = Values of degraded elastic modulus

$E_o$  = Initial elastic modulus

Values for the degraded elastic modulus were calculated as the slope of the line connecting points  $(0, \sigma_{ret})$  and  $(\varepsilon_{c,i}, \sigma_{c,i})$  where  $\sigma_{ret}$  is the value of tensile stress to ensure that negative plastic strain values will not evolve and  $(\varepsilon_{c,i}, \sigma_{c,i})$  are the total strain and stress values for a given point on the idealized stress-strain curve. It was determined for this work that  $\sigma_{ret}$  should be taken as approximately 18 percent of the concrete compressive strength and an additional five percent reduction in the compression damage values was necessary in order to avoid numerical convergence issues. The resulting value for stiffness degradation for plastic strains of 0, 0.0017, 0.0027, and 0.0035 were 0, 19, 73, and 85 percent, respectively. It was assumed that under cyclic loading, recovery of tensile stiffness after crack formation would not occur, therefore, the scalar multiple for tension recovery was nil.

Since the fracture energy type of tension stiffening was employed, tension damage criteria were prescribed as a tabular function of crack displacement,  $u_n$ . It was assumed that, at a complete loss of tensile strength ( $u_n = u_o$ ), stiffness of cracked elements would undergo a 50 percent degradation. In addition, once  $u_n$  was equivalent to  $2u_o$ , it was assumed that cracked elements would experience a 98 percent degradation in stiffness. One hundred percent degradation in stiffness was not utilized since values greater than 99 percent can drastically affect convergence (SIMULIA, 2007). It was assumed that full

recovery of compression stiffness would occur in the event of cyclic loading; that is, tensile cracking has no effect on recovery of compression stiffness. As a result, the scalar multiple of compression recovery was assumed to be unity.

#### 3.3.2.2 Elastic Concrete & Saddle Steel

To avoid unnecessary material nonlinearity at points of support, the material at the ends of the specimen was modeled as linearly elastic, with elastic properties equivalent to those previously specified for concrete. In addition, loading saddles were assumed to be nearly rigid with linear elastic properties.

#### 3.3.2.3 Hoop and Longitudinal Reinforcement

An elasto-plastic constitutive model was used to define the behavior of the hoop reinforcement and longitudinal steel. Unit weight of the steel was set as  $77.0 \text{ kN/m}^3$  ( $490 \text{ lb}_f/\text{ft}^3$ ). An elastic modulus of  $209 \times 10^3 \text{ MPa}$  ( $30.3 \times 10^3 \text{ ksi}$ ) and a Poisson's ratio of 0.3 defined the elastic response. Plastic behavior was defined in terms of tabular stress-strain data obtained from a standard reference (Collins and Mitchell, 1991).

#### 3.3.2.4 Prestressing Strands

The material used to define the prestressing tendon behavior incorporated the same options mentioned in the hoop and longitudinal reinforcement discussion. The material density prescribed was that stated for the longitudinal and hoop reinforcement. A Poisson's ratio of 0.3 was implemented, with an elastic modulus of  $189.6 \times 10^3 \text{ MPa}$  ( $27.5 \times 10^3 \text{ ksi}$ ). Plastic behavior of the prestressing steel was defined in terms of tabular stress-strain data obtained from a standard reference (Collins and Mitchell, 1991).

### 3.3.2.5 Rubber Pads

The constitutive model for the rubber pads was defined using only the elastic option since their contribution to gravity loads was both negligible and undesired. Since the manufacturer and rubber grade used in Reference 2 was undisclosed, a rubber material with a nominal durometer hardness of 70 was selected. Geolast® 701-70 Thermoplastic Rubber was the rubber selected for the FEA models. Material data was retrieved from MatWeb (2008). The elastic modulus was reported as 5.9 MPa (856 psi) with a Poisson's ratio of approximately 0.5.

### 3.3.3 *MODEL GEOMETRY*

Finite elements for the pile consisted of standard eight-node linear hexahedral 3D continuum elements with full integration. In order to simplify the modeling process, the rubber pads and loading saddles were modeled as part of the pile geometry. This eliminated the need for surface contact definitions between the rubber pads and the pile and loading saddles. It was expected that this simplification would be reasonable since the stiffness of the rubber pads was much less than the concrete and saddle stiffnesses.

The pile was meshed such that the approximate global size of each element was 30 mm (1.18 in.). In addition, 90 mm (3.54 in.) of each end of the pile were partitioned as cells to facilitate the use of the boundary conditions, which will be discussed later and will be referred to as the 'elastic ends'.

Spiral reinforcement was simplified into hoop reinforcement consisting of 80 discrete hoops with 76 mm (3 in.) spacing between each one. The end most hoops were placed 48 mm (1.89 in.) from the pile ends to facilitate symmetric spacing. Elements comprising the hoops were standard two-node 3D truss elements. The reinforcing hoop

section had a cross-sectional area of  $51.5 \text{ mm}^2$  ( $0.08 \text{ in.}^2$ ) and the hoop reinforcement material definition.

Discrete prestressing tendons and longitudinal reinforcing bars were also composed of standard two-node 3D truss elements. The tendons measured 6100 mm (240 in.) in length, while longitudinal reinforcing bars measured 536.8 mm (21 in.) in length based on the estimated length of plastic hinge formation as presented in Reference 2. Meshes for the tendons and longitudinal rebar were automatically generated. The tendon section was assigned a cross-sectional area of  $74 \text{ mm}^2$  ( $0.115 \text{ in.}^2$ ) and the prestressing steel constitutive model. Similarly, the rebar section was characterized using the hoop reinforcement material model and a  $129 \text{ mm}^2$  ( $0.2 \text{ in.}^2$ ) area of cross-section. The use of the hoop reinforcement constitutive model for the longitudinal rebar was deemed appropriate due to the variability in standard grades of reinforcing steel.

Prestressing tendons, transverse reinforcement, and longitudinal rebar (in the case of pile PS13) were included in the model assembly as embedded elements. Representations of the reinforcement layout and pile model assembly are presented in Figure 3.3.3 and Figure 3.3.4, respectively.



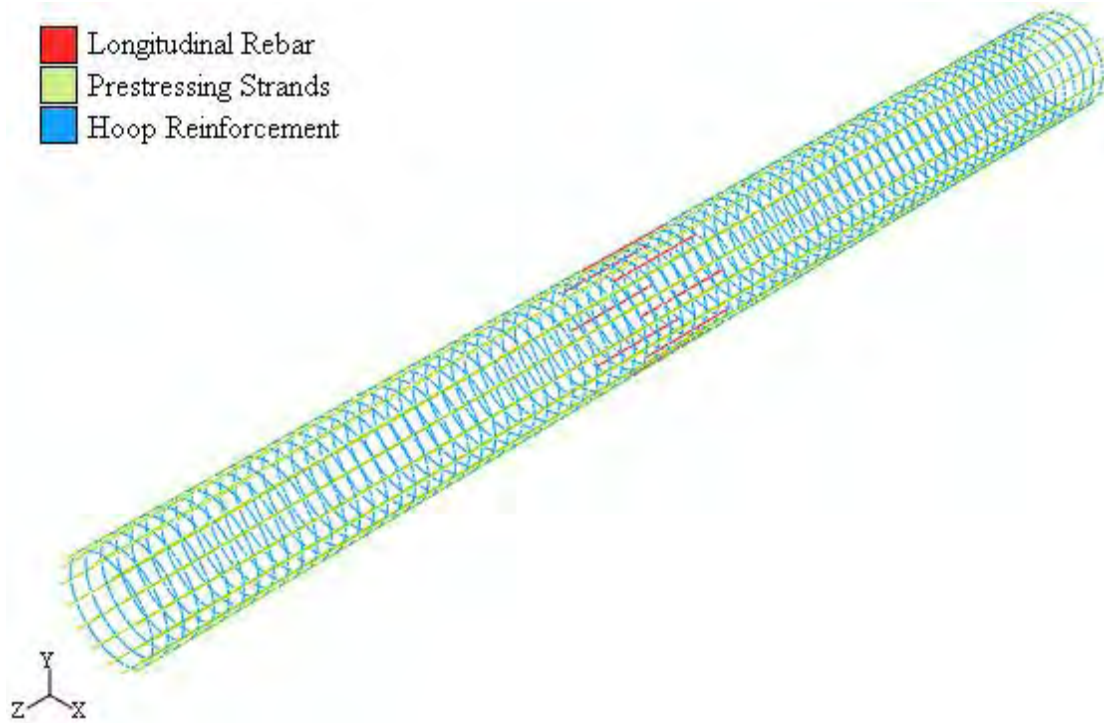


**Figure 3.3.3: Reinforcement Layout**

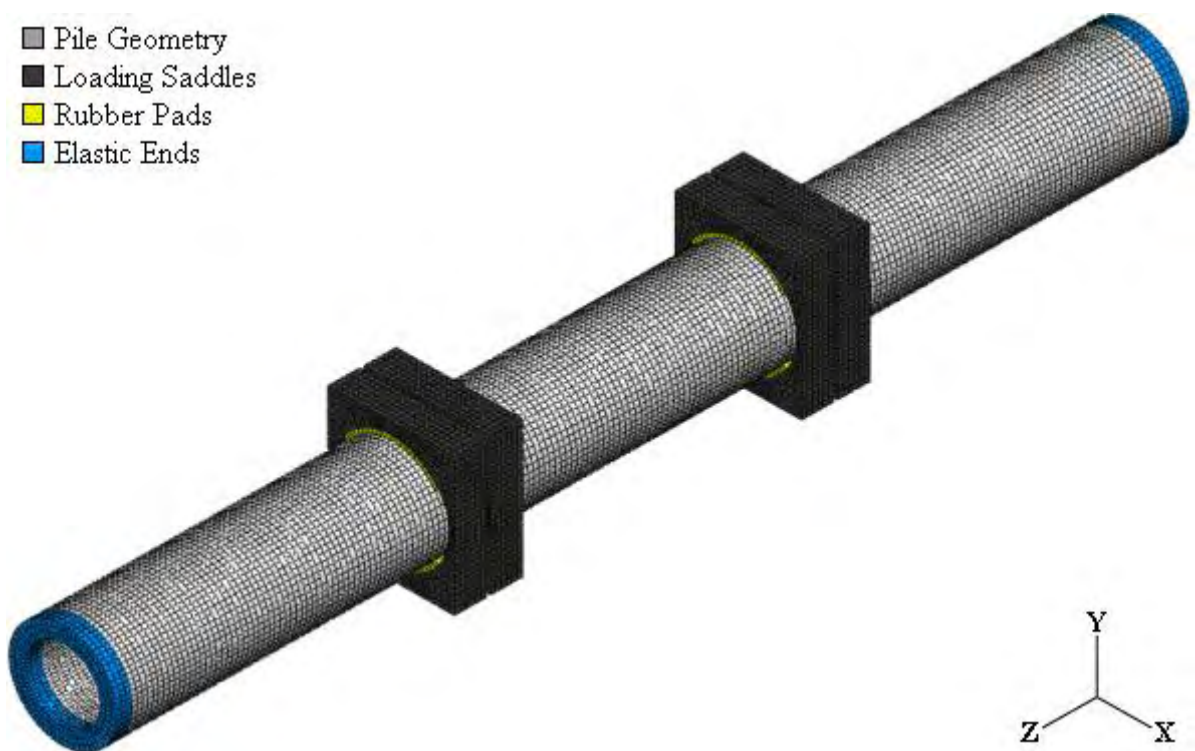


**Figure 3.3.4: Pile Assembly**

### 3.3.4 BOUNDARY & INITIAL CONDITIONS

One should refer to Figure 3.3.4 throughout the description of the boundary conditions and loading. To simulate the support conditions as described by Budek, et al. (1997b), the  $U_x$ ,  $U_y$  and  $U_z$  degrees of freedom (DOF) were constrained for selected centroidal nodes at the left end of the pile to simulate a pin support, while DOF  $U_x$  and  $U_y$  at the right end were similarly constrained to simulate the roller support. In order to avoid erroneous results and stress concentrations at the constrained boundary condition nodes, 90 mm (3.54 in.) at each end of the pile were defined by the aforementioned elastic concrete constitutive model. To facilitate generation of load-displacement plots, mid-span displacement in the  $y$ -direction was monitored during each increment of each loading step.

Prestressing was applied using a stress-type initial condition. Prestressing was applied to the sixteen tendons at a magnitude of 744 MPa (107.9 ksi) in the  $z$ -direction. Although it was not expected to be significant, nonlinear geometry was considered during application of initial conditions. Gravity loads were also applied as an initial condition in the negative  $y$ -direction.

### 3.3.5 LOADING

Two loading steps were used for the analysis of the 3D pile model. For the first step, an axial load of 890 kN (200 kips) was applied at the roller supported end of the pile as a 5.84 MPa (847 psi) uniformly distributed pressure on the pile cross-section in the positive  $z$ -direction. This loading was prescribed as a non-following surface traction in order to

remove any effect of end rotation. Nonlinear geometry due to large deformations and deflections was also included in the step definition.

The second loading step consisted of a monotonic push in the negative  $y$ -direction. The monotonic push was symmetric in nature about the  $x$ - $y$  plane of symmetry at mid-span. Loading was defined as uniformly distributed ramped pressures applied to the top of each saddle. The maximum magnitude applied to each of the two outer saddles was prescribed as 1.656 MPa (240 psi) and 79.5 percent of that for the interior two saddles. Nonlinear geometry due to extreme deformations and displacements was also considered during the monotonic push step of the analysis.

### 3.3.6 ABAQUS RESULTS

The performance of both specimens was governed by the tensile capacity of the concrete. Tensile cracks propagated into the cross-section leading to softening of the post-yield stiffness. Once tensile cracks extended through the tension side of the pile up to the neutral axis, a nearly linear response followed until compressive failure began at the opposite pile surface. At that point, convergence was unattainable and the analysis was terminated.

Load is plotted against displacement ductility for both PS12 and PS13 specimens in Figure 3.3.5 and Figure 3.3.6, respectively. Displacement ductility is defined as the ratio of displacement at any time,  $t$ , to displacement at yield. It should be noted that displacement ductility of one for specimens PS12 and PS13 was specified in the experimental work as 13 mm (0.5 in.) and 20 mm (0.79 in.), respectively. The performance of both specimens was governed by the tensile capacity of the unconfined concrete. Tensile cracks propagated into the cross-section, which was indicated by the

incremental reduction in stiffness in the initial post-yielding region of the curves. Once tensile cracks extended through the tension side of the pile up to the neutral axis which had, in the process, shifted upward, a nearly linear response followed until compressive failure began at the opposite pile surface. At that point, convergence was unattainable and the analysis was terminated. Incipient formation of tensile cracks occurred immediately after yielding in both models at an end reaction of approximately 150 kN (33.7 kips). These results agreed well with those from testing. From the slope of the curves, it is apparent that the post-cracking stiffness of the model and the ductility at failure also match those of the experiments. The difference in the experimental and analytical curves is that damage initiated earlier in the test specimens. Figure 3.3.5 and Figure 3.3.6 illustrate that both FE models are able to accurately predict the initial and post-yield stiffness of the experimental results. Both models, however, over-predict the yield load by approximately 14 percent. In addition, both models over-predict the peak load by 8 percent for specimen PS12 and 20 percent for specimen PS13. These over-predictions could again be attributed to the fact that the analytical model was loaded monotonically rather than cyclically.

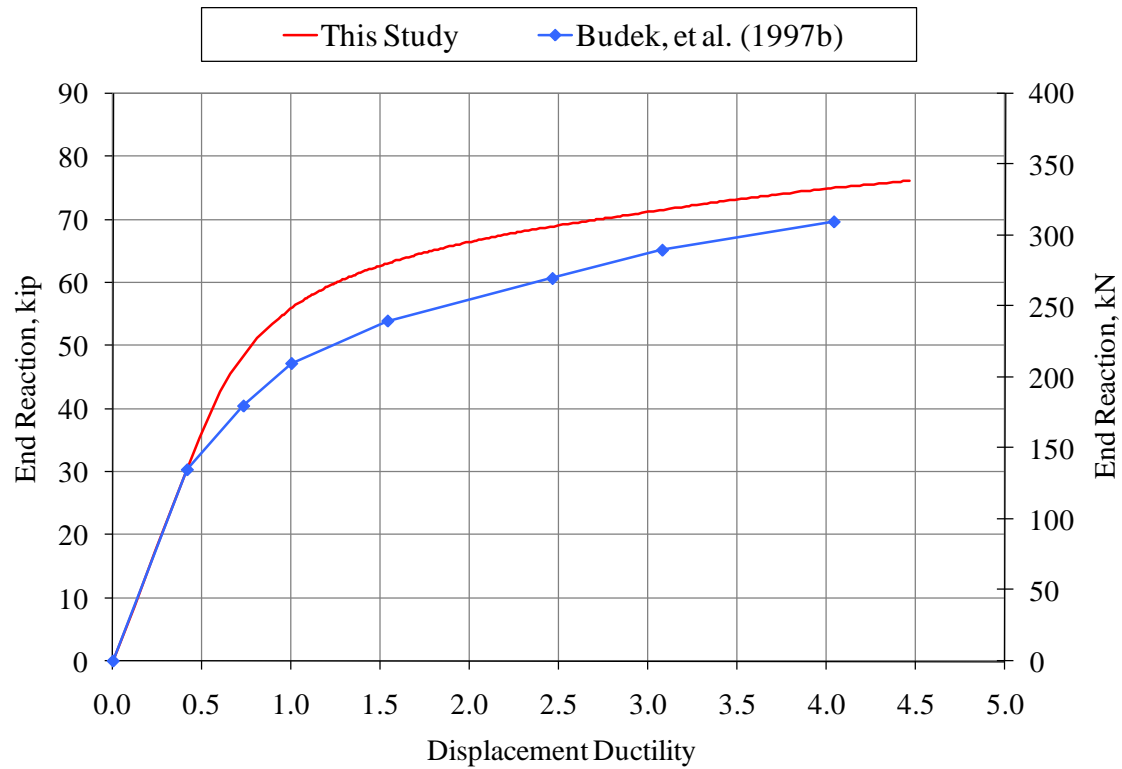


**Figure 3.3.5: Comparison of Finite Element and Test Results for Specimen PS12**

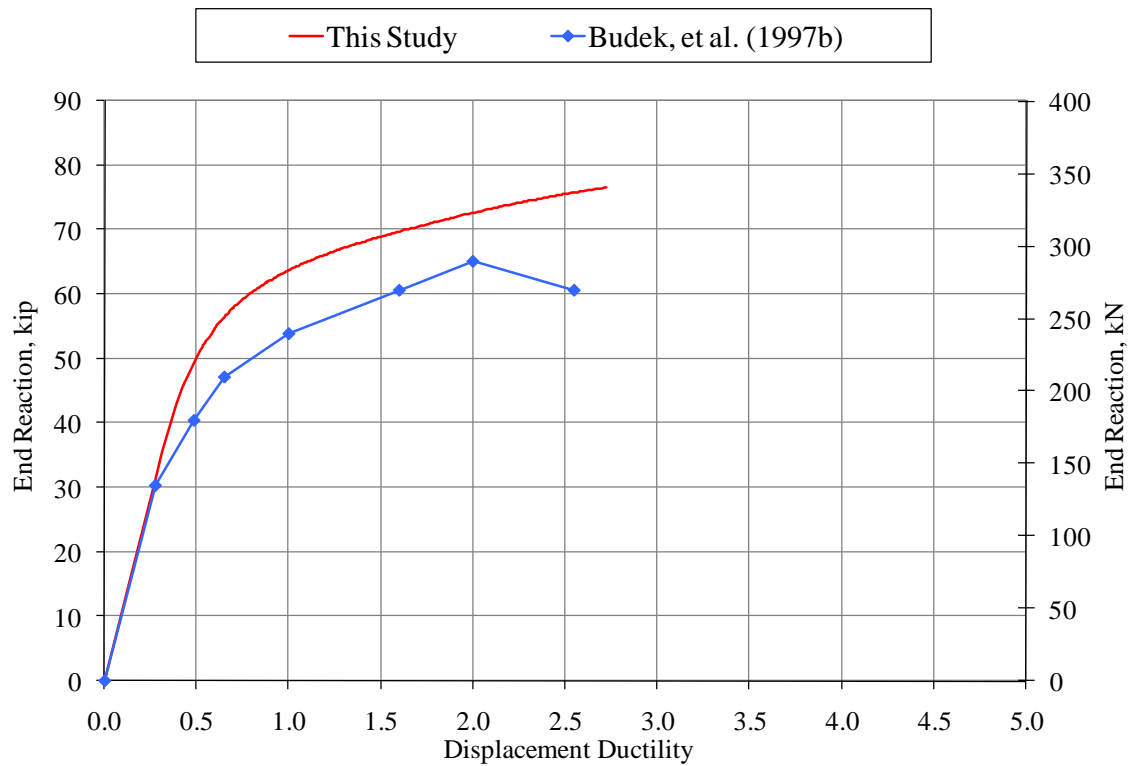


**Figure 3.3.6: Comparison of Finite Element and Test Results for Specimen PS13**

Failure in both 3D finite element models was quantified by monitoring the compression damage variable in the output database. Compression damage is calculated based on equivalent plastic strain, thus, it includes multiaxial strain behavior. To facilitate this discussion, Specimen PS12 will be the model in reference. As previously mentioned in the discussion of the concrete constitutive model, spalling of concrete occurred at a compressive strain of 0.0027, which corresponds to 19 percent compression damage. In addition, once concrete spalled to the depth of the tendons and hoop reinforcement, failure was noted for the experimental specimens. By setting an upper limit for the contour plot of compression damage to 19 percent and looking at the last increment of the monotonic push phase, the distribution of compression damage in the pile cross-section can be seen in Figure 3.3.7 and Figure 3.3.8. By inspection of these figures, one can see that the compressive damage during the last increment of the analysis is over 16 percent. The analysis of the model was not able to progress any further due to material convergence issues. This indicated that the current condition of the model is unstable and spalling of the concrete to the depth of the prestressing tendons and hoop reinforcement is imminent.

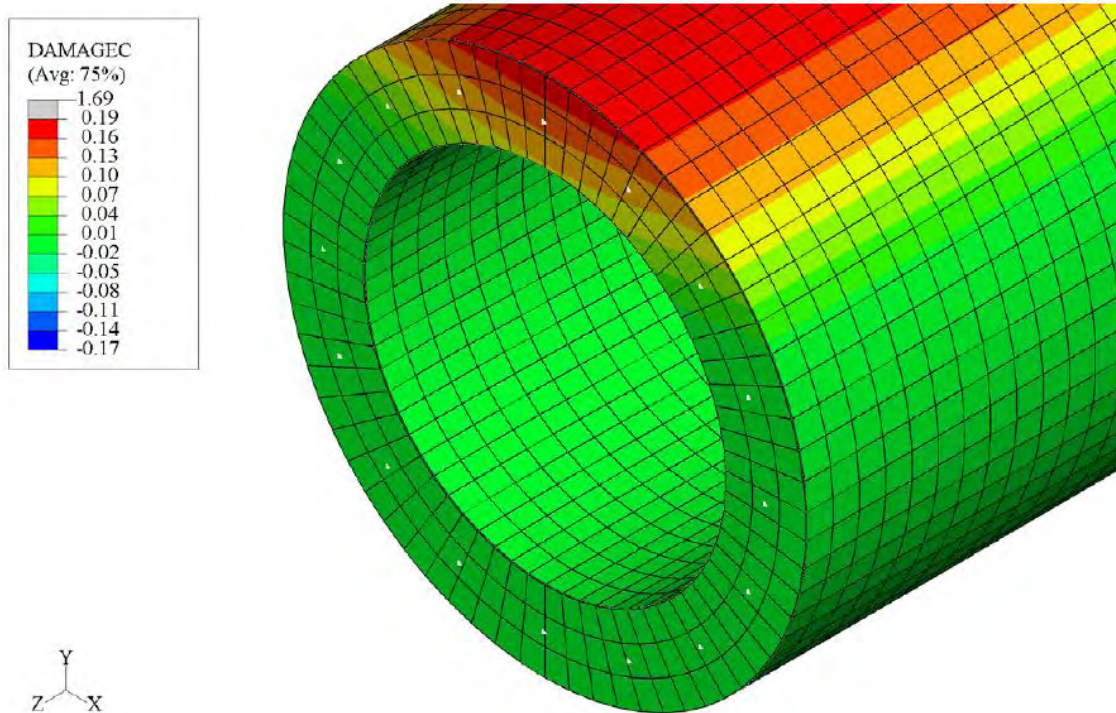


**Figure 3.3.7: Contour Plot of Compressive Damage,  $d_c$ , (x-y section)**

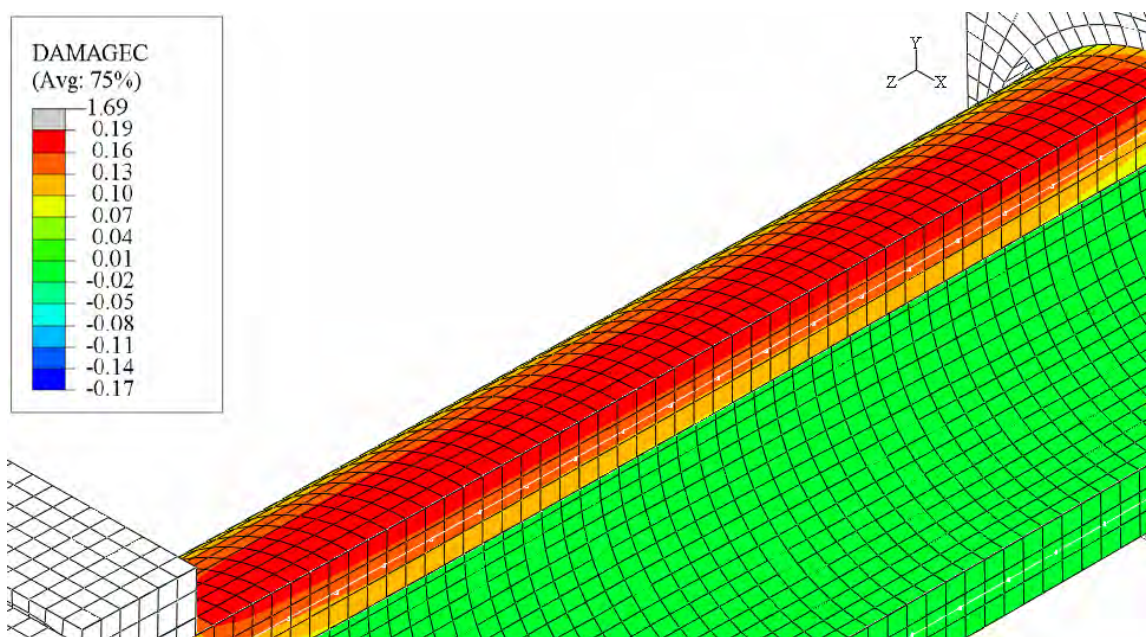


**Figure 3.3.8: Contour Plot of Compressive Damage,  $d_c$ , (y-z section)**

To supplement the analytical evidence that failure in the FE models agrees with mechanisms observed by Budek, et. al (1997b), vector plots of plastic strain were also generated. Typical vector plots of this nature for specimen PS12 are given in Figure 3.3.9 and Figure 3.3.10. When looking at the plot of plastic strain for the final increment of the analysis, it is important to note that on the outer surface along the  $y$ - $z$  plane, the maximum principal plastic strain, minimum principal plastic strain, and mid principal plastic strain occur in the  $y$ -,  $z$ - and  $x$ -axis directions, respectively. This indicates that the concrete on the exterior surface was being thrust away from the reinforcing steel and prestressing strands due to large compressive stress in the longitudinal direction. Upon examination of the inner surface of the pile along the  $y$ - $z$  plane, the maximum principal plastic strain changes to the  $x$ -direction, while the minimum and mid principal plastic strains occur in the  $z$ - and  $y$ - directions, respectively. This three dimensional behavior and the resulting effect on damage is not included in the cross-sectional analysis of XTRACT and it suggests that the concrete inside the confines of the hoop reinforcement responds similarly to confined concrete with respect to direction of plastic strain, but not appreciably so in terms of stress capacity.



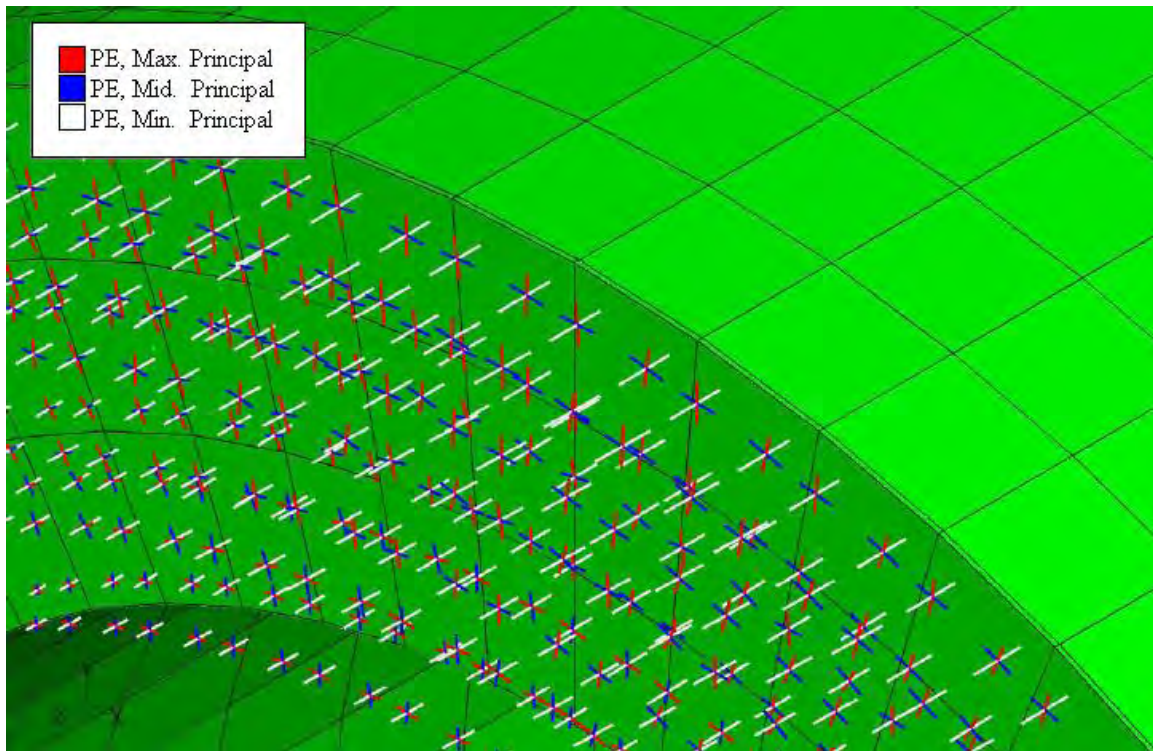


**Figure 3.3.9: Principal Plastic Strain Distribution (x-y section)**

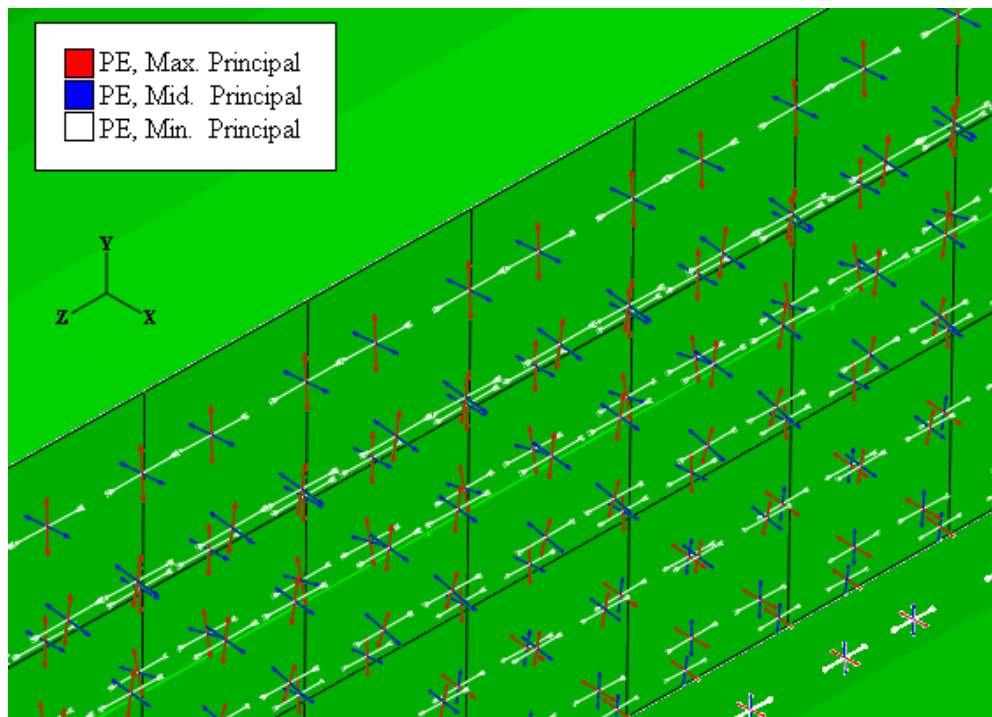


**Figure 3.3.10: Principal Plastic Strain Distribution (y-z section)**

### 3.3.7 SENSITIVITY ANALYSIS

Five parameters were varied through a series of analyses to understand their effect on model performance. Volumetric transverse reinforcement ratio ( $\rho_t$ ), compressive damage ( $d_c$ ), fracture energy ( $G_f$ ), tensile strength ( $f_{sp}$ ), and prestressing force ( $P_s$ ) were the parameters investigated. Table 3.3.1 summarizes the additional analyses performed for the sensitivity analysis.

**Table 3.3.1: Summary of Analyses for Sensitivity Analysis**

Parameter	Description	Value Used
Volumetric Transverse Reinforcement Ratio	Nominal: used 8.1 mm diameter wire	0.20%
	Increased: used 9.91 mm diameter wire	0.40%
	Decreased: used 4.03 mm diameter wire	0.03%
Fracture Energy	Nominal: based on crack depth, $a = 43 \text{ mm}$	0.095 N/mm
	Increased: based on crack depth, $a = 86 \text{ mm}$	0.190 N/mm
	Decreased: based on crack depth, $a = 21.5 \text{ mm}$	0.048 N/mm
Concrete Compression Damage	Nominal: defined using -12 MPa return stress	19% @ $f'_c$
	Increased: defined using -18 MPa return stress**	22% @ $f'_c$
	Decreased: defined using -9 MPa return stress	14% @ $f'_c$
Concrete Tensile Strength	Nominal: defined by splitting strength per (12)	4.67 MPa
	Increased: defined by modulus of rupture per (12)	7.69 MPa
	Decreased by using 50% of nominal value	2.33 MPa
Prestressing Force	Nominal: 16 – 12.7 mm strands, 744 MPa stress	73 kN / tendon
	Increased: 16 – 15.24 mm strands, 744 MPa stress	104 kN / tendon
	Decreased: 16 – 9.53 mm strands, 744 MPa stress	41 kN / tendon

\*\* Analysis could not be completed.

Modifying transverse reinforcement ratio had a negligible effect on the performance of the pile, which was consistent with observations of Budek, et al. (1997b). This can be attributed to the fact that modifying the volumetric transverse reinforcement ratio provides an increase in compressive strength for confined concrete. Furthermore, since there is an absence of core concrete, confining hoop reinforcement provides no

modification to concrete compressive strength. The results from the analyses are presented in Figure 3.3.11.

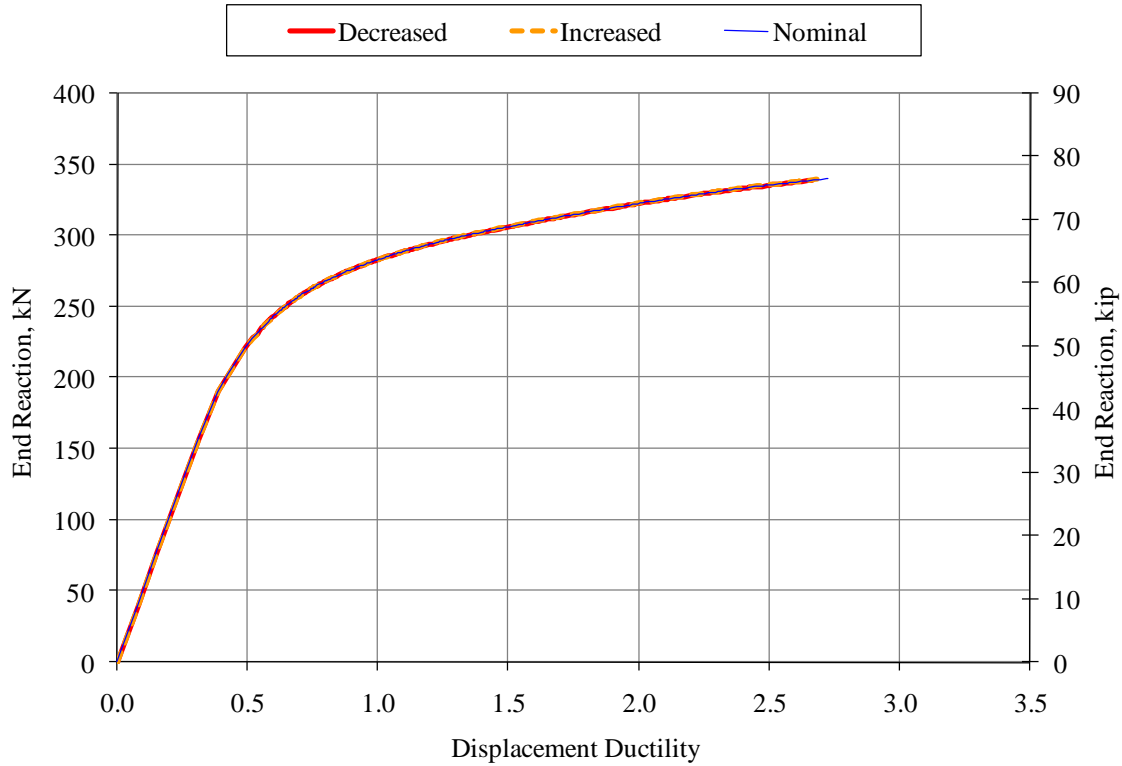


**Figure 3.3.11: Effect of Volumetric Transverse Reinforcement Ratio ( $\rho_t$ )**

Modifying compressive damage also had little effect on displacement ductility and load capacity. In addition, it had no effect on post-yield stiffness. This occurs since the overall performance of the model is driven by the tensile behavior of the concrete whereas the compression damage governs global failure.

Fracture energy was found to be one of the most influential parameters of the FE model. As shown in Figure 3.3.12, adjusting fracture energy affects the post-yield stiffness of the model, as well as displacement ductility. Doubling the value of fracture energy increases the post-yield stiffness by roughly 17 percent. The increase in strength, however, reduces the maximum ductility of the model. Decreasing fracture energy causes

a slight reduction in the yield load and apparently causes a significant loss in peak strength and ductility. This occurs because the energy which must be accumulated to initiate tensile cracking is much less, hence, tensile cracking initiates much earlier in the model. However, one would expect ductility to increase when fracture energy is decreased since tensile cracks initiate earlier and propagate to a greater depth more rapidly. The rapid propagation of tensile cracks causes a vertical shift in the neutral axis, decreasing stiffness and the size of the compression zone, while increasing maximum ductility. This is not the case in Figure 3.3.12 but it should be noted that the model with decreased fracture energy did not fail as expected. Hence, the analysis was terminated due to material nonconvergence which indicates numerical instability rather than physical failure. Therefore, it is imperative that fracture energy be carefully specified based on the concrete strength.

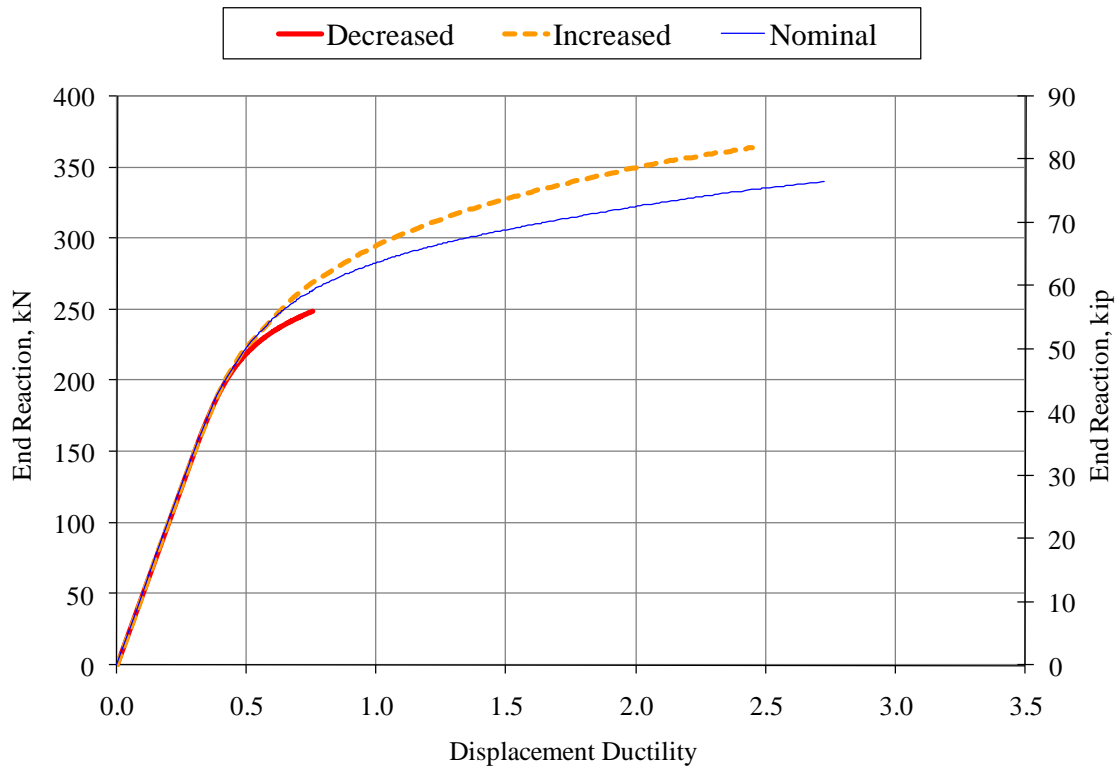


**Figure 3.3.12: Effect of Fracture Energy,  $G_f$**

The effect of modifying tensile strength is shown in Figure 3.3.13. As shown, decreasing the tensile strength of the concrete apparently significantly affects ductility and load capacity, while increasing the tensile strength only affects load capacity. It is also evident that yielding is controlled by the tensile strength of the concrete. Similar to fracture energy, one would expect a decrease in tensile strength to increase maximum ductility, but this is not the case for the analytical model. As before, results indicated that material nonconvergence issues prevented the analysis from being completed and physical failure was not observed.

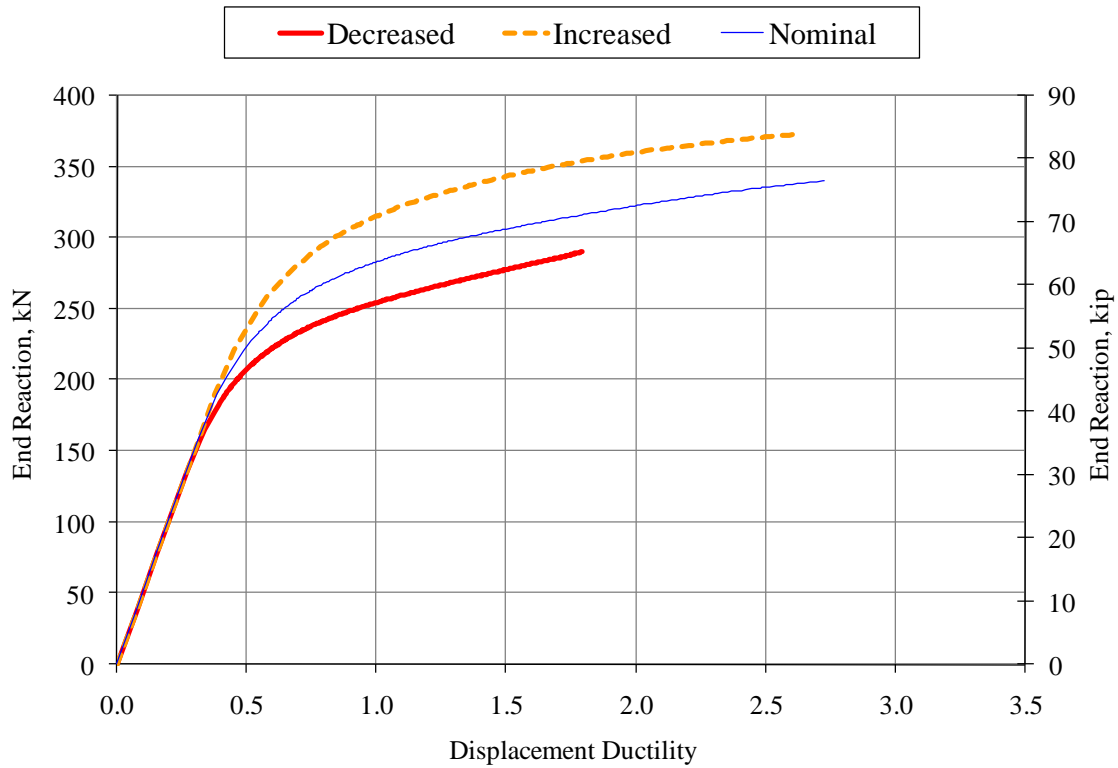


**Figure 3.3.13: Effect of Concrete Tensile Strength,  $f_{sp}$**

The effect of prestressing force on load and ductility is presented in Figure 3.3.14. It is important to note that changing the prestressing force modifies the post-yielding stiffness of the pile and maximum displacement ductility. As the prestressing force increases, displacement ductility decreases while load capacity increases. Also, post-yielding stiffness for this case is increased by approximately 15 percent. Conversely, as prestressing force decreases, displacement ductility increases while load capacity decreases. In addition, post-yielding stiffness was reduced by nearly 20 percent for this case.

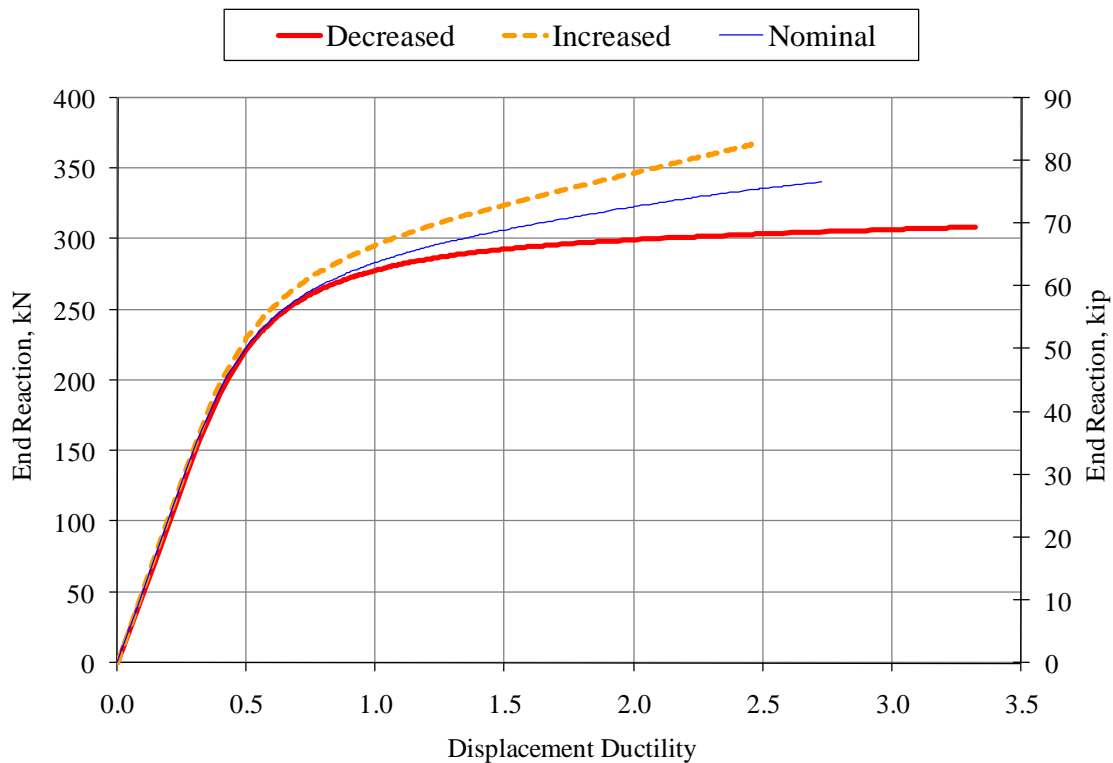


**Figure 3.3.14: Effect of Prestressing Force**

### **3.4 SAP2000 ADVANCED NONLINEAR**

#### *3.4.1 INTRODUCTION*

In order to determine the force-displacement response of specimens PS12 and PS13, which is crucial for displacement based design, the moment curvature relationships developed in XTRACT were implemented in a simple pile model in SAP2000. The general procedure for doing so is to model the pile as a simply supported beam under four-point-bending with a point plastic hinge. Note that, since the specimen was subjected to four-point-bending, it was assumed that the plastic hinge would form at the center of the region of constant moment, or midspan of the pile. The behavior of the beam elements were defined in terms of the effective moment-curvature response of the pile, with the yield surface defined as the axial load-effective moment interaction diagram.

#### *3.4.2 PLASTIC HINGE DEFINITION*

As previously mentioned, the pile was modeled as a simply supported beam subjected to four-point bending with an 890 kN (200 kips) axial load applied at the roller supported end. The model consisted of a single beam element with a point plastic hinge at midspan. The plastic hinge was defined as a P-M type hinge, which requires a yield surface, location of the plastic hinge, length of plastic hinge ( $L_p$ ), and cross-section behavior under inelastic deformation.

The yield surface was defined as an axial load-effective yield moment interaction diagram based on XTRACT output. In order to generate the yield surfaces for Specimens PS12 and PS13, bilinearized moment-curvature relationships were determined for various

tensile (T) and compressive (C) axial loads using XTRACT. From the collection of bilinearized or, effective, moment-curvature data for each specimen, the effective yield point was transcribed from each relationship, as shown in Figure 3.4.1 and Figure 3.4.2.

The transcribed values for effective yield moment are then plotted against their respective values of axial load in order to formulate the basis of the axial load-effective yield moment (P-M) interaction diagram for each specimen. Once the values are plotted, a parabolic regression is fitted to the data in order to generate the remainder of the yield surfaces. The 2D yield surface definitions are presented in Figure 3.4.3.

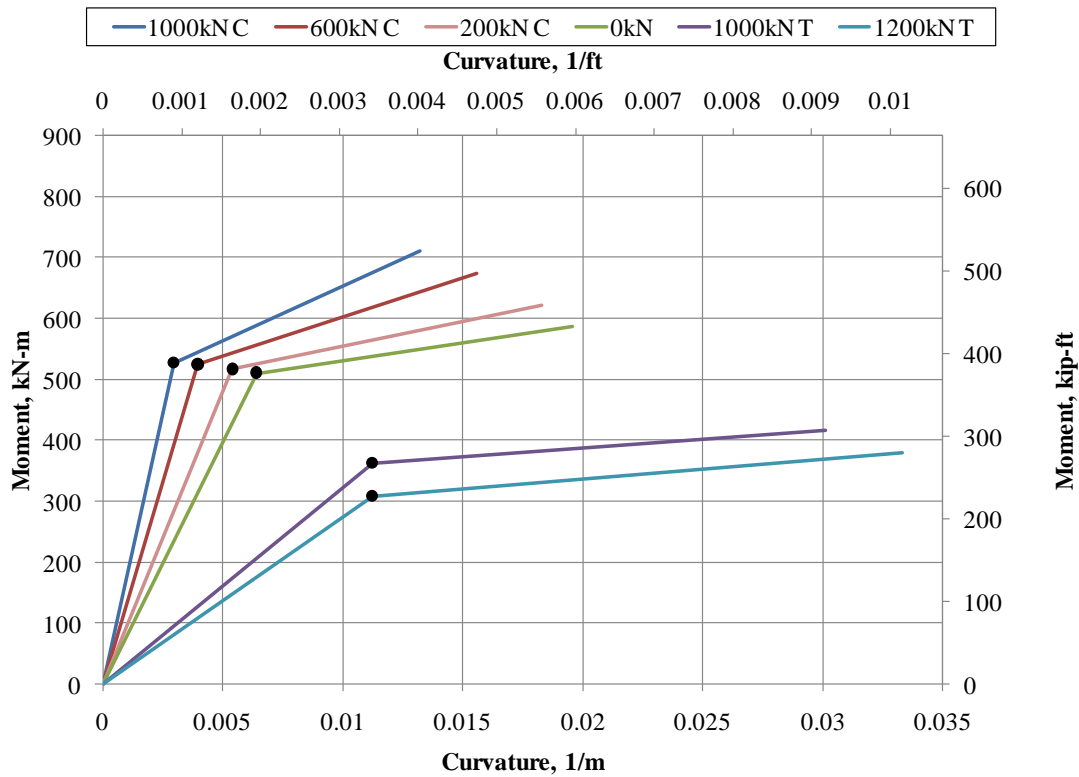


**Figure 3.4.1: Effective Moment-Curvature Relationships, Specimen PS12**



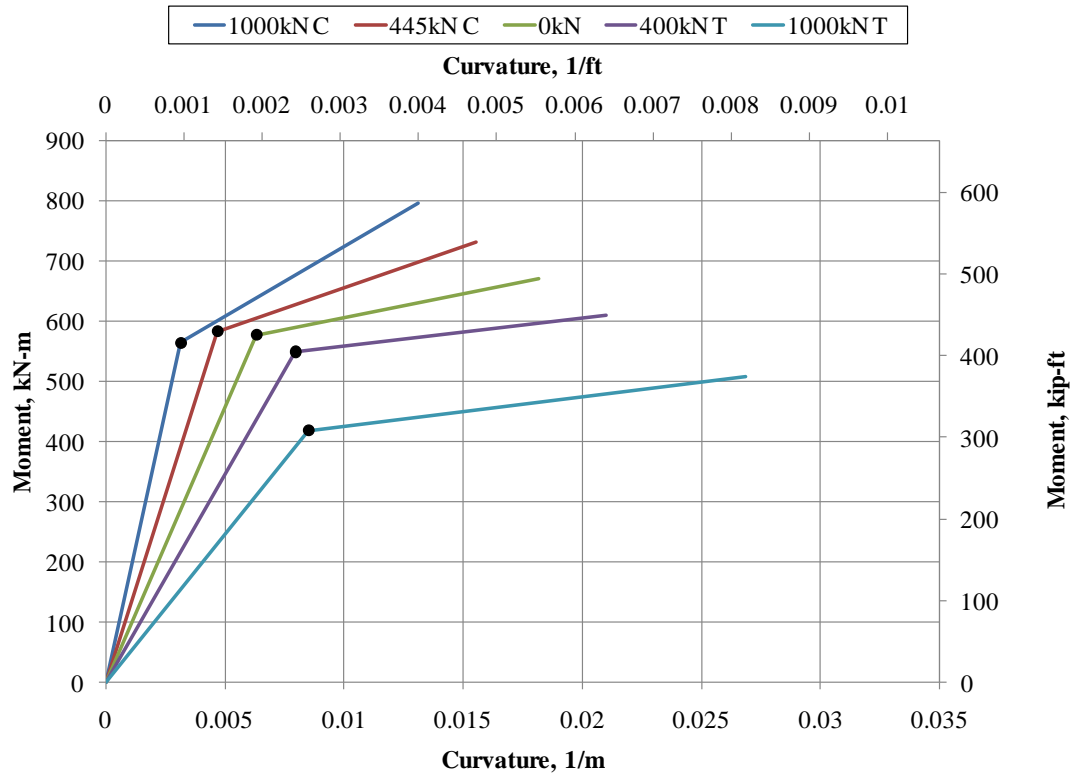


**Figure 3.4.2: Effective Moment-Curvature Relationships, Specimen PS13**

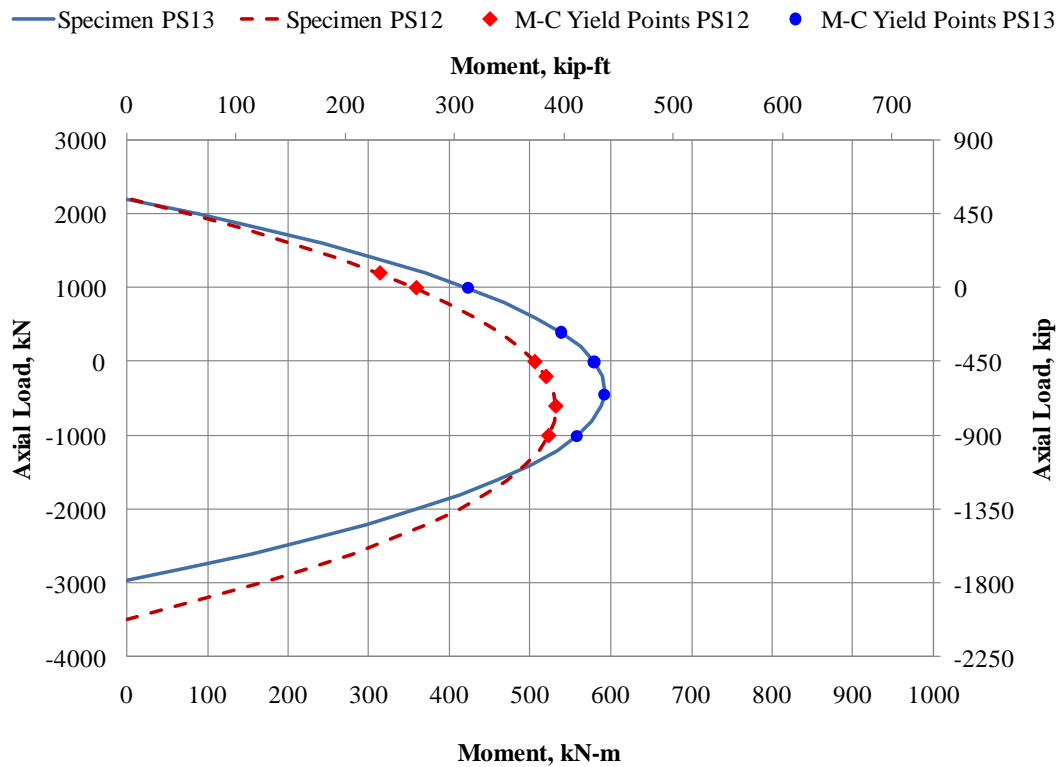


**Figure 3.4.3: P-M Interactions (Yield Surfaces) for Specimens PS12 and PS13**

The plastic hinge length was defined as  $1.4-D$ ,  $D$  being the outer diameter of the pile, per Caltrans recommendations for non-cased Type I pile shafts (Caltrans, 2006). To investigate sensitivity of the plastic hinge length, analyses were also carried out for lengths of  $2.64D$ , based on ABAQUS results,  $2.8-D$ ,  $1.4-D$  (for Specimen PS12), and  $1.45-D$  (for Specimen PS13), based on experimental observations (Budek, et al., 1997b). It should be noted that the plastic hinge length observed in ABAQUS was taken as the length of the compressive zone where incipient spalling was observed; that is to say, the region where the compressive damage variable was in excess of 16 percent, as discussed in Section 3.3.6.

Post yielding behavior was defined by effective moment-curvature responses from XTRACT for axial loads of 204, 890, and 1634 kN (46, 200, and 367 kips, respectively). The moment-curvature relationships for specimens PS12 and PS13 were generated by XTRACT and are presented in Figure 3.4.4, and Figure 3.4.5, respectively. Three moment-curvature relationships are supplied to SAP2000 in order for it to linearly interpolate between the provided curves for the inelastic response of the cross-section based on curvature in the event of an increase or decrease in axial load. Hence, the axial loads specified in moment-curvature analyses encompassed the minimum and maximum expected moment values throughout the analyses. However, since the analyses were nonlinear static pushover analyses only the nominal axial load need be applied in this case.

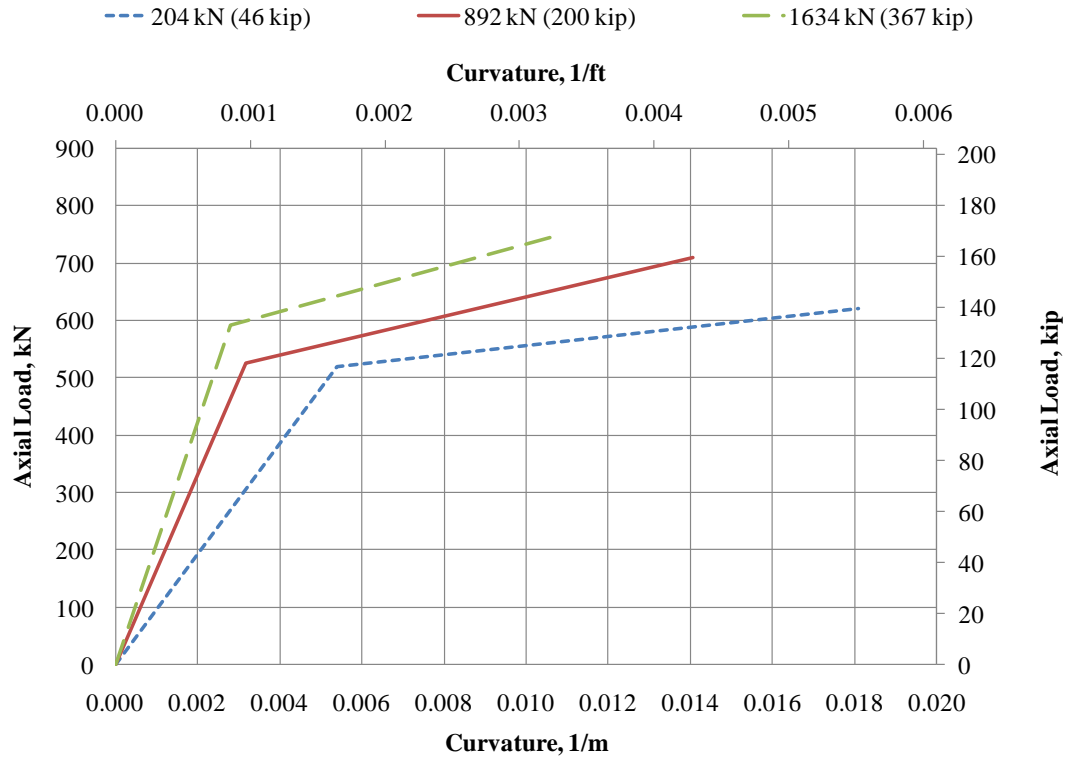


**Figure 3.4.4: Moment-Curvature Relationships for Specimen PS12**

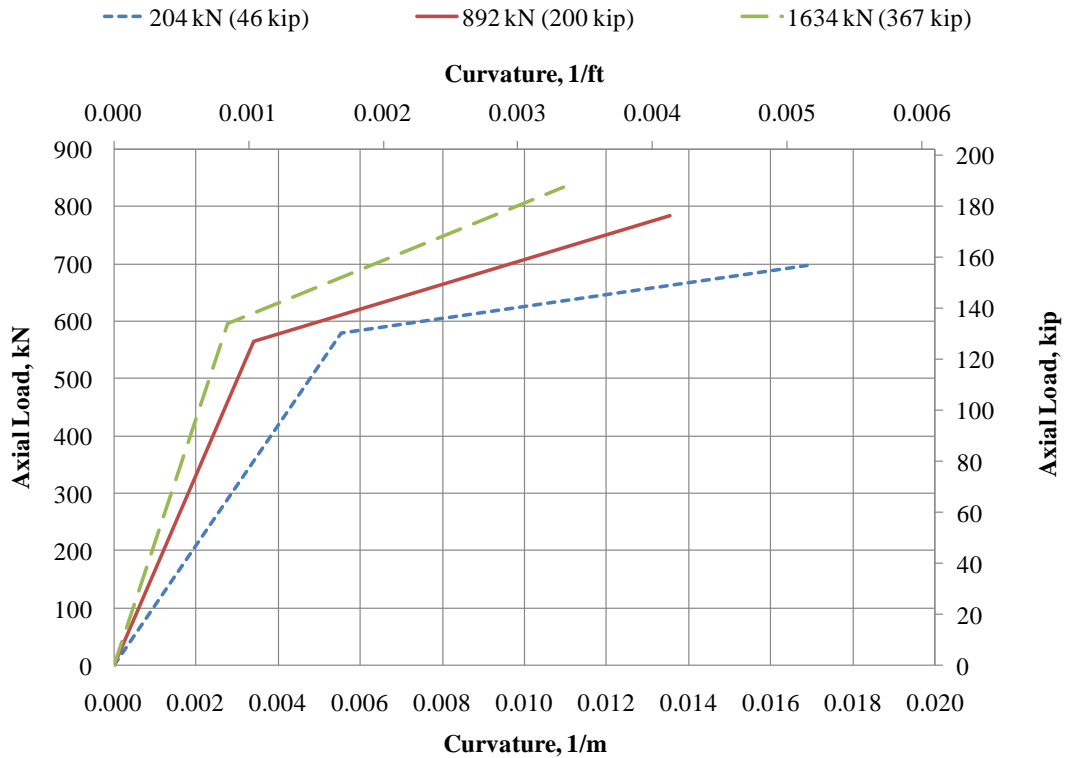


**Figure 3.4.5: Moment-Curvature Relationships for Specimen PS13**

### 3.4.3 SAP2000 RESULTS

Results from the SAP2000 Advanced Nonlinear analyses using a plastic hinge length of  $1.4D$  are compared to experimental results in Figure 3.4.6 and Figure 3.4.7 for specimens PS12 and PS13, respectively. Figure 3.4.6 clearly indicates that using a plastic hinge length based on Caltrans (2006) recommendations results in an underestimation of displacement ductility by nearly 50 percent and a slight overprediction of load capacity. Similarly for specimen PS13, Figure 3.4.7 illustrates that displacement ductility is underestimated by roughly 40 percent with negligible difference in load capacity.

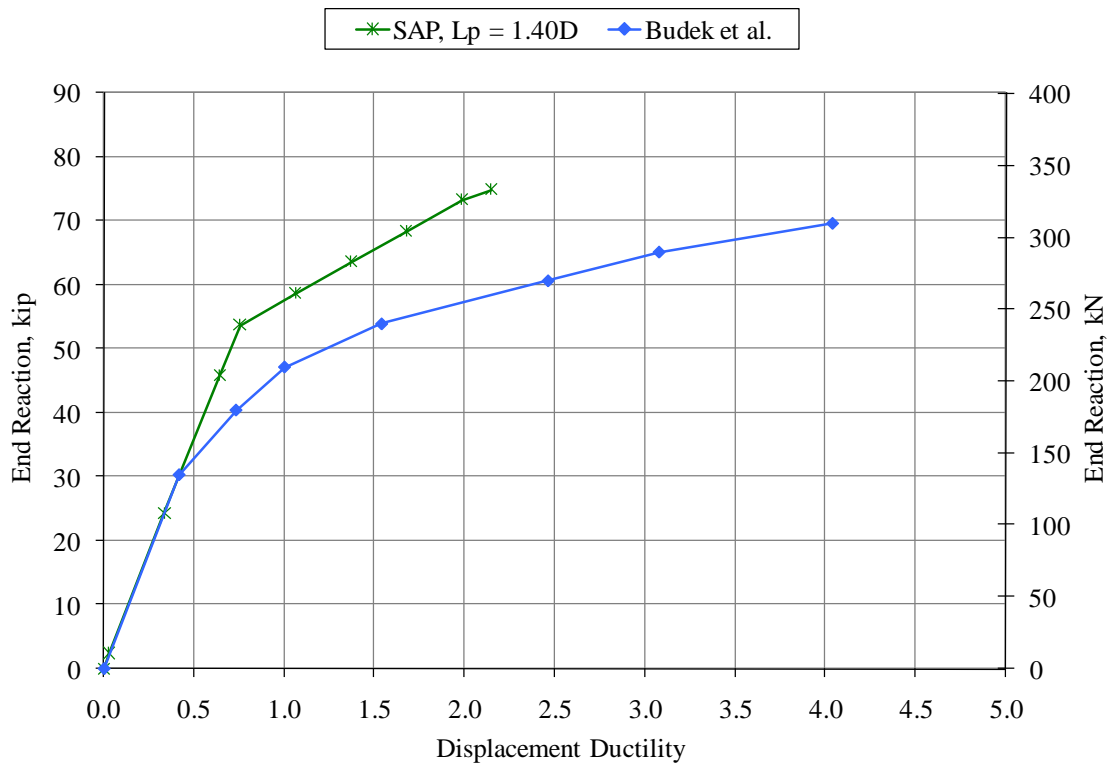


**Figure 3.4.6: Comparison of SAP2000 and Experimental Results for Specimen PS12**

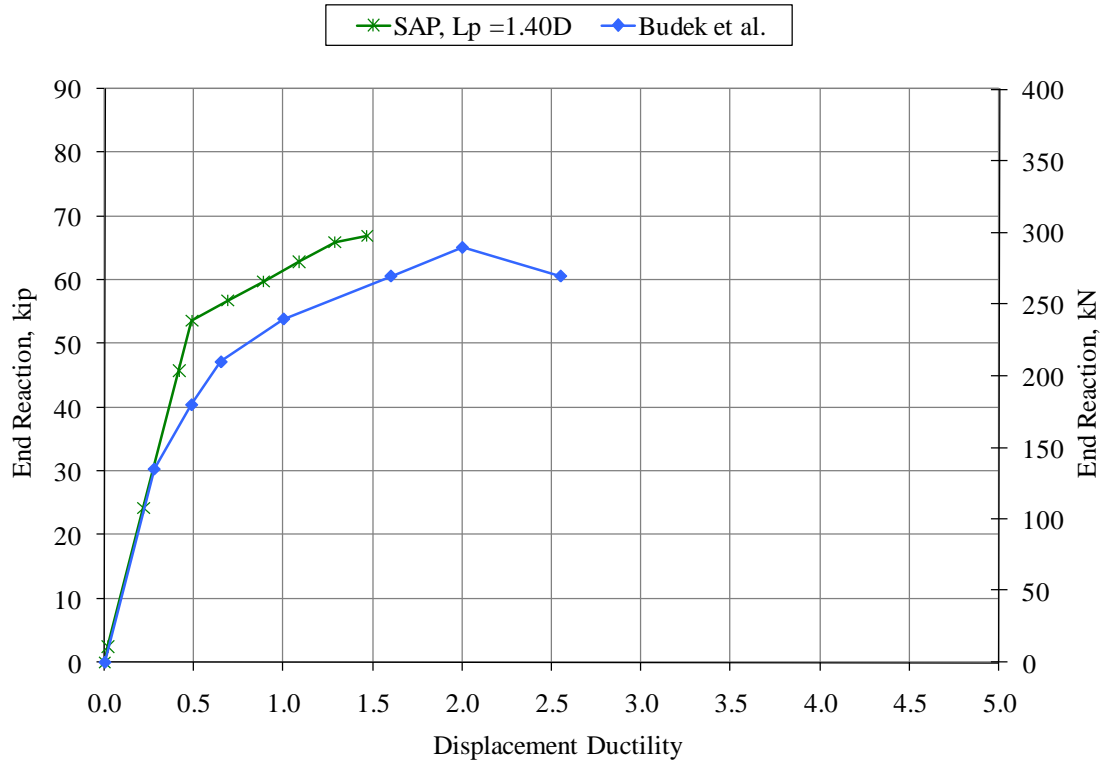


**Figure 3.4.7: Comparison of SAP2000 and Experimental Results for Specimen PS13**

The results for the SAP2000 analyses for plastic hinge lengths of  $2.64-D$ , and  $2.8-D$  for specimens PS12 and PS13 are presented in Figure 3.4.8 and Figure 3.4.9, respectively. One should note that results from the analysis of specimen PS13 with  $L_p = 1.45-D$  are not shown since they varied negligibly compared to the that of  $L_p = 1.4-D$ . Upon examination of Figure 3.4.8, one can see that the prediction of displacement ductility is greatly improved when the plastic hinge length is specified based on ABAQUS results or twice the Caltrans Seismic Design Criteria recommended length (2006). In the case of specimen PS12, displacement ductility was underestimated by roughly 20 percent, yet load capacity is predicted within about eight percent.

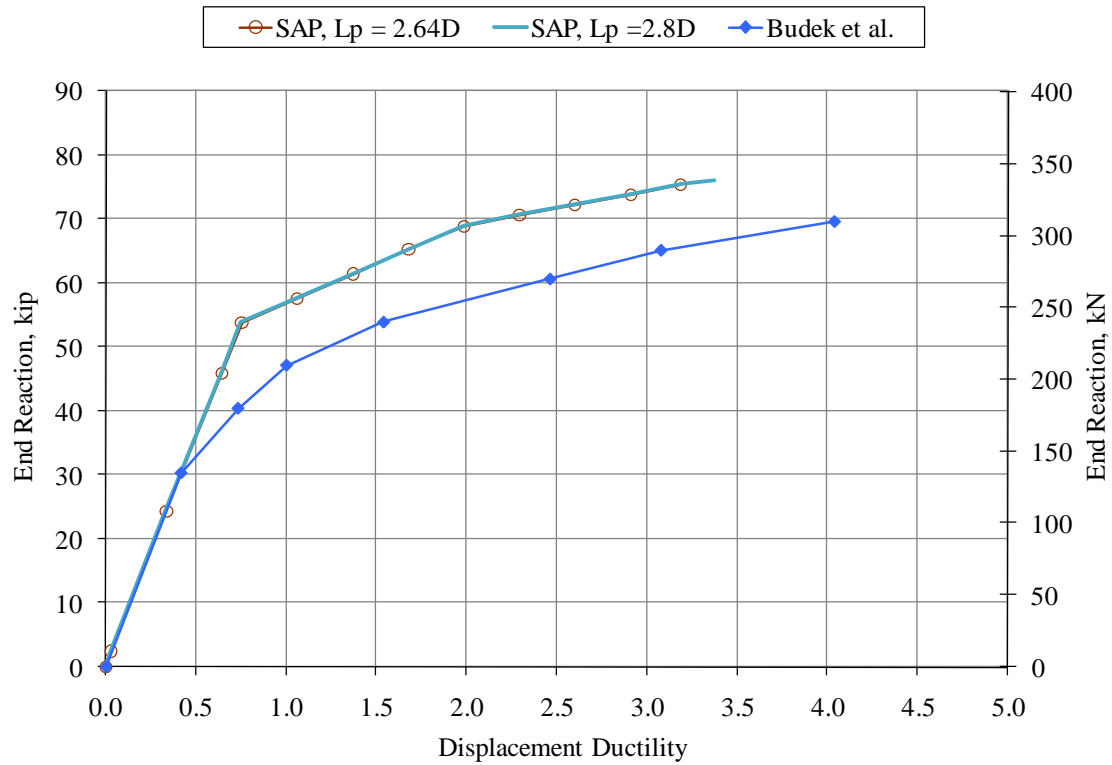


**Figure 3.4.8: Comparison of SAP2000 and Experimental Results, Specimen PS12**

When viewing the results for specimen PS13, similar observations are noted. The increase in the specified plastic hinge length provides predictions for displacement ductility and load capacity that more accurately predict experimental results. In Figure 3.4.9, the predictions for displacement ductility at failure and load capacity at softening are within approximately ten percent. Therefore, the results from Figure 3.4.6, Figure 3.4.7, Figure 3.4.8, and Figure 3.4.9 clearly indicate that the plastic hinge length will govern the performance of the analytical model when all other parameters are held constant.

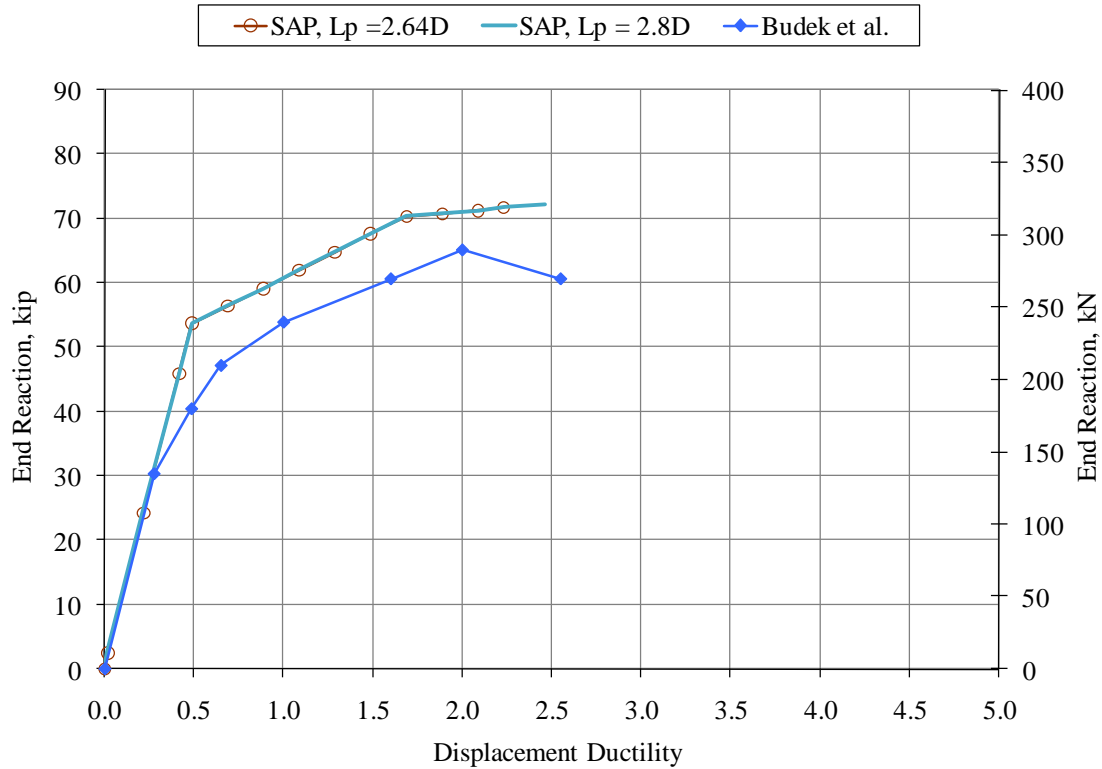


**Figure 3.4.9: Comparison of SAP2000 and Experimental Results, Specimen PS13**

The results from the SAP2000 analyses using  $L_p = 2.64-D$  are compared to those from ABAQUS and experimental testing for specimens PS12 and PS13 in Figure 3.4.10 and Figure 3.4.11, respectively. Both figures clearly indicate that the simplified analyses which incorporate XTRACT moment-curvature data to define post-yielding behavior in SAP2000 can reasonably predict the response of the tested specimens. In addition, the simplified analyses provide reasonable approximations of the much more complex finite element analyses.

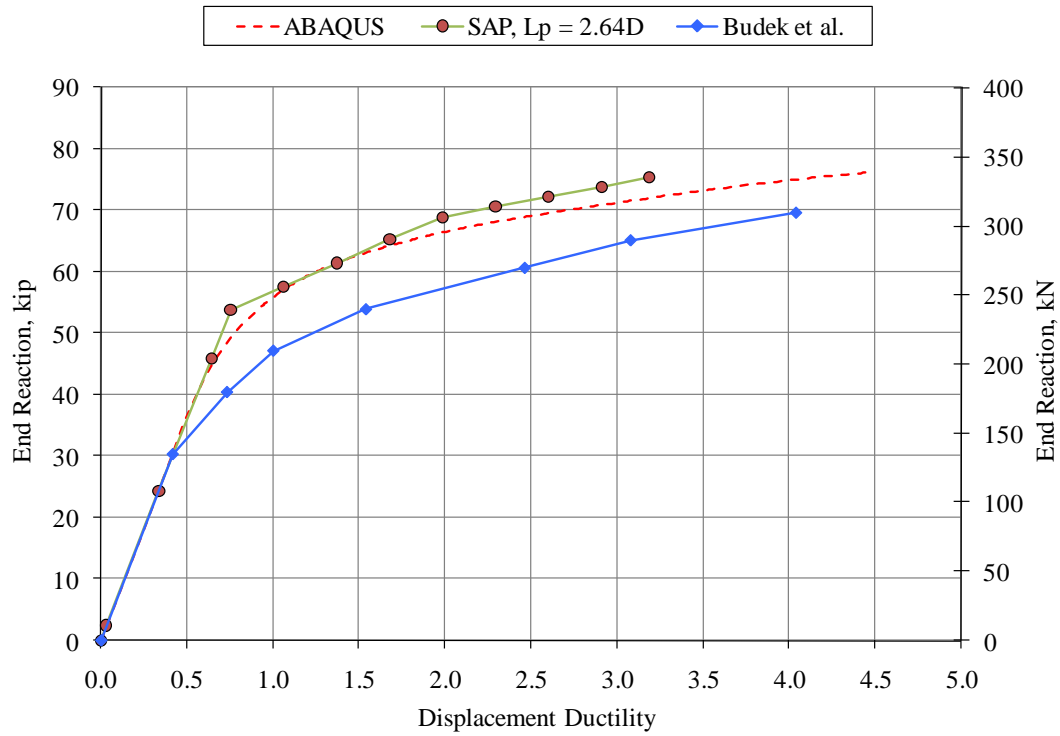


**Figure 3.4.10: Comparison of ABAQUS, SAP2000, and Experimental Results (Specimen PS12)**

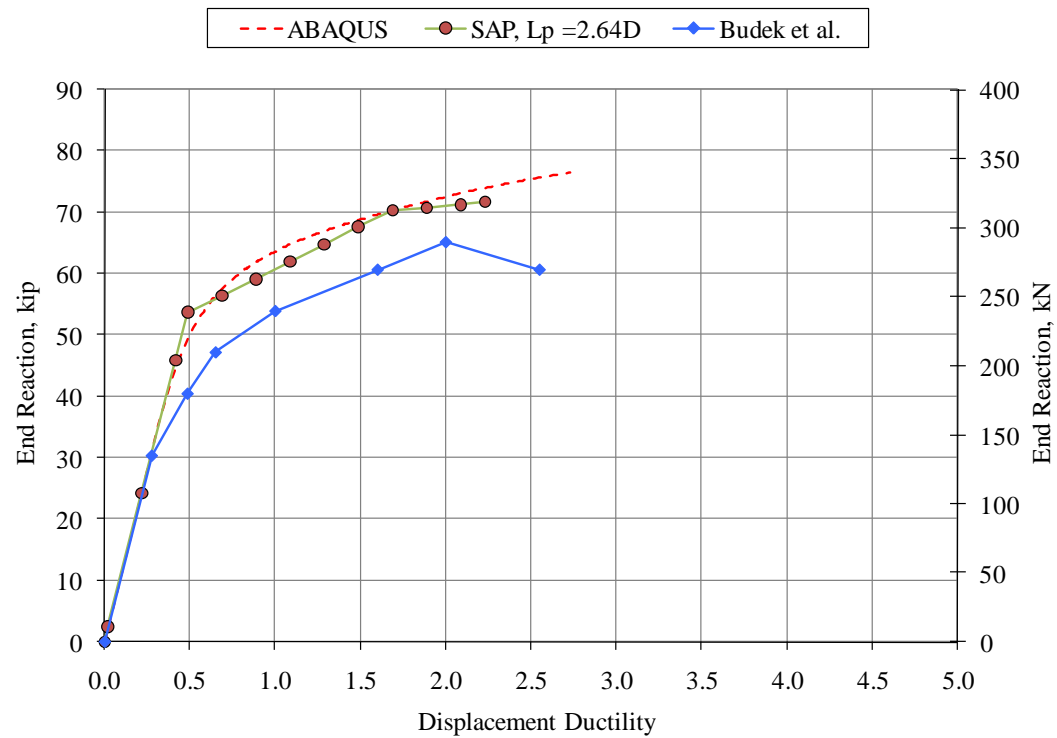


**Figure 3.4.11: Comparison of ABAQUS, SAP2000, and Experimental Results (Specimen PS13)**



### 3.5 CONCLUSIONS

This chapter was devoted to presenting the formulation of analytical models for tested specimens denoted as PS12 and PS13 by Budek, et al. (1997b). The objectives of this portion of the research were to (1) outline a systematic method for defining material parameters for each of the analytical models developed, and (2) qualitatively and quantitatively understand the failure mechanisms associated with hollow precast prestressed reinforced concrete piles. In order to accomplish these major tasks, the analytical models were verified against experimental results (Budek, et al., 1997b). The analytical models which were developed and discussed in this chapter are to be applied to *in situ* piles of similar construction in Washington State in order to understand their performance under lateral loading.

In Section 3.2, the formulation of the XTRACT models for the two specimens was discussed, and the method for defining them was detailed. Section 3.3 contained a discussion of pertinent details of the finite element model proposed and also presented a systematic method for defining input parameters for the concrete damaged plasticity model available within ABAQUS. In addition, a sensitivity analysis was carried out on the finite element model in order to better understand the behavior of the model. Section 3.4 presented a method for comparing analytical results from XTRACT and ABAQUS analyses by means of SAP2000 Advanced Nonlinear pushover analyses. A sensitivity study was also carried out for the definition of the plastic hinge length.

Based on the analytical results obtained using the method discussed in this chapter, the following conclusions are set forth:

- Cross sectional analysis appears to be adequate for predicting moment capacity. However, it does not reflect the damage and loss of stiffness from cyclic loading of the concrete without longitudinal reinforcement.
- ABAQUS provides more accurate results for ductility than those of XTRACT. This could be attributed to the fact that ABAQUS includes the effect of multiaxial stress from hoop reinforcement in the concrete failure response, while XTRACT only considers uniaxial behavior.
- The finite element analyses, cross-section analyses, and experimental work (Budek, et al., 1997b) have shown that failure occurs once concrete in the compression zone spalls, exposing the reinforcing steel and prestressing tendons, allowing them to buckle.
- The proposed 3D finite element model is capable of capturing the behavior of prestressed hollow core concrete piles. Load capacity and displacement ductilities at yield and failure for both pile specimens appear to be well-predicted by the ABAQUS model, with an overprediction in strength of roughly 20 percent. This overestimation could be attributed to the fact that the analytical model was loaded monotonically while the experimentally tested piles were subjected to cyclic loading, as indicated by Tuladhar, et al. (2007).
- Excessive values for fracture energy can lead to convergence issues; therefore, a systematic approach to calculate the fracture energy is set forth. The proposed methodology utilizes concrete cylinder splitting strength to define tensile strength of the concrete and concrete cover thickness to define the crack depth.

- The sensitivity analysis has shown that the concrete tensile strength, fracture energy, and prestressing force are the most influential parameters on the performance of the pile model. Transverse reinforcement ratio has negligible effect on load capacity and displacement ductility which agrees with experimental observations (Budek, et al., 1997b). This is attributed to the fact that, due to the hollow core, confining steel does not improve concrete compressive strength or ultimate strain.
- Based on results from the sensitivity analysis, it is evident that the values used to define the concrete constitutive model have resulted in the most accurate predictions for displacement ductility and lateral load capacity. Overall, the systematic approach used in defining constitutive parameters provides accurate predictions for strength, ductility, and mode of failure.
- The series of simplified analyses discussed in this section were found to provide reasonable approximations to both the complex finite element analyses and experimental results. Although the plastic hinge length does not adversely affect load capacity predictions, careful consideration must be taken when specifying the plastic hinge length for SAP2000 analyses since inaccurate values can lead to drastic over or underestimation of displacement ductility.
- XTRACT cross section analyses combined with SAP2000 nonlinear pushover analyses provide conservative approximations for pile performance when the plastic hinge length is defined per Caltrans Seismic Design Criteria (2006). In these analyses, displacement ductility capacity was under-estimated by an

average of 35 percent when using this simplified approach based on current design practice.

## CHAPTER FOUR

### 4. IN SITU PILE MODELING

#### 4.1 INTRODUCTION

As mentioned in Section 1.2, the analytical models presented in Chapter 3 were developed in order to be applied to *in situ* piles of similar construction in the I-5 Ravenna Bridge located in the Puget Sound region of Washington State. Specifically, the three research objectives for the *in situ* pile models were: (1) develop a model using two soil types in order to understand the influence of confining pressure from the soil on the exterior surface of the pile, (2) determine whether or not confining pressure is great enough such that the cover concrete in the pile behaves as confined concrete, and (3) determine the location and length of the subgrade plastic hinge. In addition, the previously discussed simplified analytical method based on current design practice was used to compare 2D cross-section analyses to results from the Finite Element Analyses. It should be noted that the models discussed in this chapter were generated using U.S. Customary units (lbs, in., s).

#### 4.2 PILE DESCRIPTION

The piles used in the I-5 Ravenna Bridge have an outer diameter of 1220 mm (48 in.) with an inner diameter of 965 mm (38 in.), resulting in a wall thickness of 127 mm (5 in.). The piles were specified to be constructed with concrete having a compressive strength no less than 41.4 MPa (6000 psi). However, Chapter 7.5 Part 1 of the FHWA Seismic Retrofitting Manual for Highway Structures (2006) specifies that it is

permissible to increase the design strength of concrete structures by 30 percent to accommodate long term curing. Therefore, the compressive strength of the piles was taken as 53.8 MPa (7800 psi). The overall length of each pile in the bridge varies depending on the required elevation of the bents, but they measure roughly 13.7 m (45 ft.) in length. The above ground height of the piles also varies depending on ground and bent elevation, but ranges from 5.5 m (18 ft.) to 7.0 m (23 ft.). For this work, the above ground height of the pile was taken as 5.5 m (18 ft.). The piles were specified to be driven to a bearing capacity of 2310 kN (520 kips). The applied axial load for the pile was calculated to be 1180 kN (266 kips) based on the tributary area of the deck, girders, and cross beam. One should note that this well agrees with the minimum factor of safety of two, which is common for foundation design.

In the design drawings of the hollow precast piles, longitudinal reinforcement was specified to be provided, at a minimum, as one-half of one percent of the gross cross section area, with spacing and bar size specified at the contractor's option. Thus, the minimum area of longitudinal reinforcement required is  $2180 \text{ mm}^2$  ( $3.38 \text{ in}^2$ ). Since the specific details of the contractor's decision were not available, longitudinal reinforcement was specified in the form of 12 M#16 280 MPa (#5 Gr. 40 ksi) rebar, resulting in  $2374 \text{ mm}^2$  ( $3.68 \text{ in}^2$ ) of longitudinal reinforcement. The prestressing steel was specified as twelve 15.25 mm 1725 MPa (0.6 in. Gr. 250 ksi) 7-wire strands, each initially post-tensioned to 270 kN (61 kips). Details of the pile cross-section are presented in Figure 4.2.1.

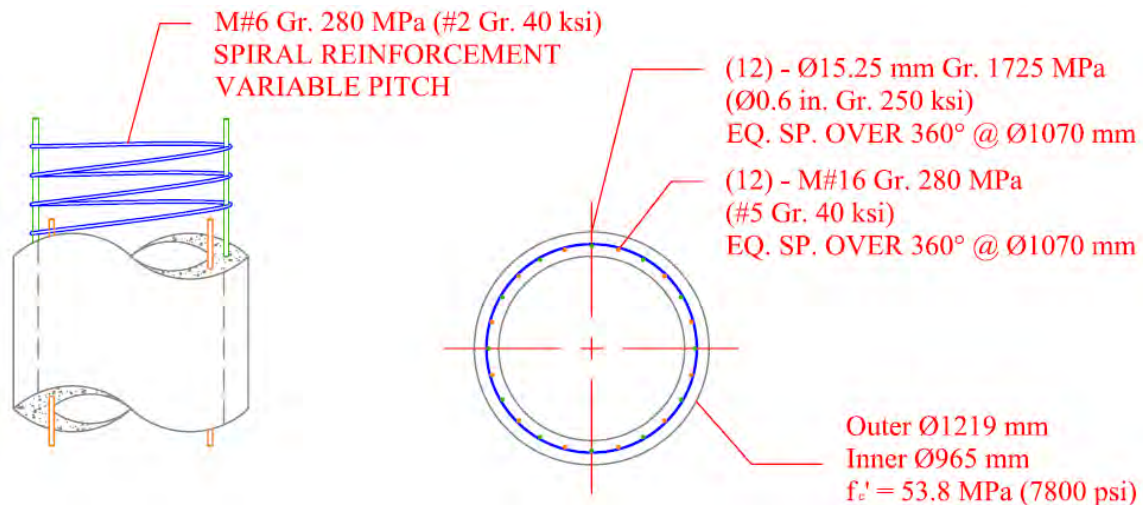


**Figure 4.2.1: Cross-Section of *In situ* Piles**

Transverse reinforcement was provided using M#6 280 MPa (#2 Gr. 40 ksi) spiraled reinforcement with a variable pitch, depending on the location along the pile length. Specifically, the spiral was to have 5 turns in the first 76 mm (5 in.), a pitch of 76 mm for 1219 mm of length (3 in. for 48 in. of length), followed by a pitch of 152 mm (6 in.) through the mid-section of the pile. In addition, the transverse reinforcement was specified to be symmetric with respect to mid-span of the pile with an end spacing of 51 mm (2 in.). An overview of the transverse reinforcement layout is presented in Figure 4.2.2.

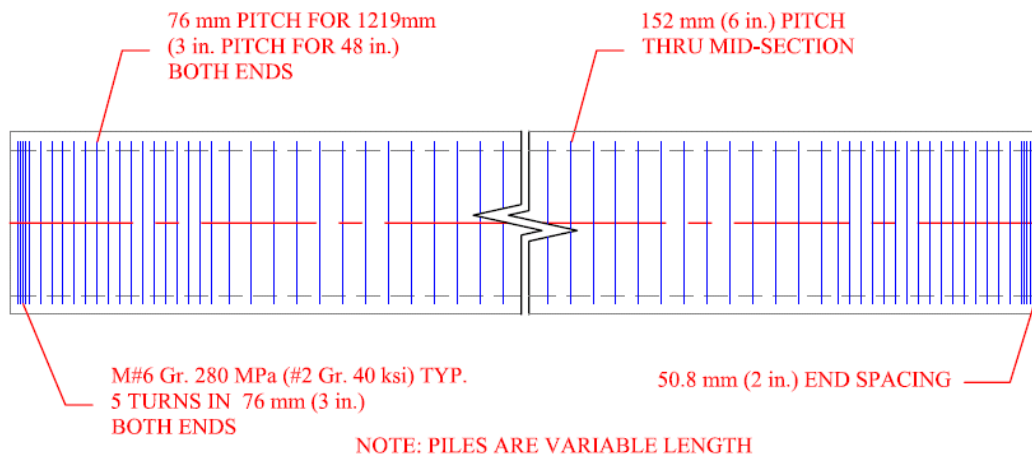


**Figure 4.2.2: Transverse Reinforcement Details of *In situ* Piles**

### 4.3 XTRACT MODELING

The *in situ* pile was modeled in XTRACT according to the aforementioned specifications using the method presented in Section 3.2.2 to define the unconfined concrete material properties. Reinforcing steel was modeled using the predefined parabolic-hardening steel model for A615 Gr. 60 ksi steel available within XTRACT. Prestressing steel behavior was defined using the A416 Gr. 250 ksi high strength prestressing steel model available in the XTRACT material library. The input parameters for the unconfined concrete, longitudinal reinforcement, and prestressing strands are provided in Table 4.3.1, Table 4.3.2, and Table 4.3.3, respectively.

**Table 4.3.1: Unconfined Concrete Properties**

Elastic Modulus	34.71 GPa	5034 ksi
Compressive Strength	53.78 MPa	7800 psi
Post Crushing Strength	0 MPa	0 psi
Tensile Strength	4.18 MPa	606.3 psi
Yield Strain	0.00103	
Crushing Strain	0.00250	
Spalling Strain	0.00250	
Failure Strain	0.00250	

**Table 4.3.2: Longitudinal Reinforcement Properties**

Elastic Modulus	200 GPa	29000 ksi
Yield Stress	275.8 MPa	40 ksi
Fracture Stress	482.6 MPa	70 ksi
Strain at Hardening	0.015	
Failure Strain	0.120	

**Table 4.3.3: Prestressing Strand Properties**

Elastic Modulus	200 GPa	29000 ksi
Yield Stress	1465 MPa	212.5 ksi
Ultimate Stress	1724 MPa	250 ksi
Strain at Ultimate	0.035	
Failure Strain	0.035	



An overview of the pile cross-section model, before analysis, is presented in Figure 4.3.1. The prestressing strands and longitudinal reinforcement are represented by the red and black circles, respectively, and grey for the unconfined concrete. Loading for the analysis consisted of 1180 kN (266 kips) applied axially at the beginning of the analysis with an incrementing moment about the x-axis. Note that the prestressing force during the analysis was taken as the initially applied post-tension force of 270 kN (61 kips).

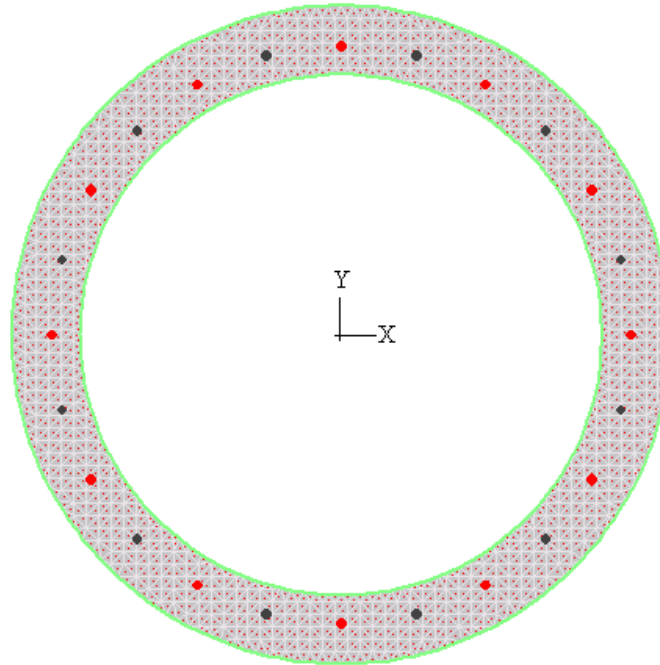


**Figure 4.3.1: *In Situ* Pile Cross-Section Model**

#### 4.3.1 XTRACT RESULTS

The section behavior at failure for the XTRACT model of the *in situ* pile is shown in Figure 4.3.2. Note that the overall performance of the model was governed by the tensile behavior of the concrete, as was the case for the calibration models. The observed failure mechanism for the *in situ* pile is spalling of the cover concrete once strains in the compressive region reach 0.0025. Furthermore, the analysis becomes unstable and is

terminated once the cover concrete spalls to the depth of the tendons, as was the case for the calibrated models in Chapter 3. One should note that the depth of spalling is more pronounced for the *in situ* pile than for the calibrated models. This can be attributed to the fact that there is larger number of discrete fibers in the *in situ* model. Upon inspection of Figure 4.3.2, one can observe that six of the longitudinal reinforcing bars yielded in tension and two in compression, while no yielding occurs in the prestressing strands.

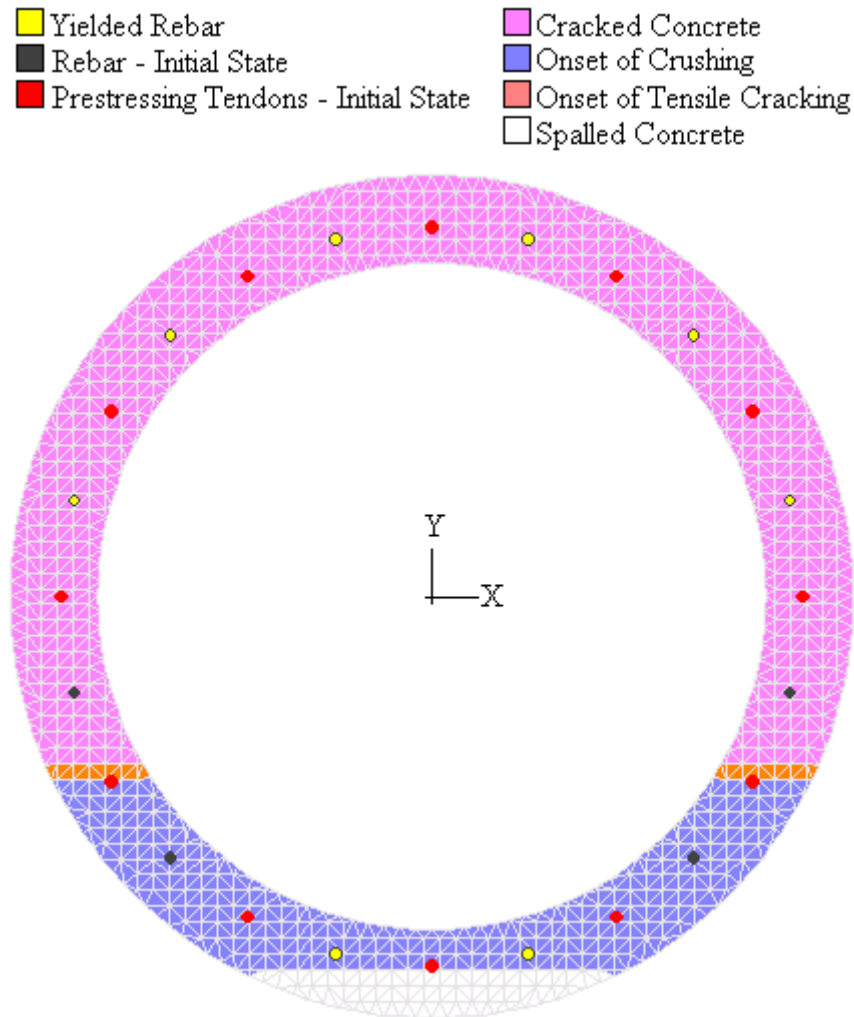


**Figure 4.3.2: Deformed Cross-Section of *In Situ* Pile Model**

The moment-curvature ductility relationship for the *in situ* pile cross-section analysis is provided in Figure 4.3.3. Curvature ductility ( $\mu_\phi$ ) of 1.0 was defined at a curvature of

$7.86 \times 10^{-4} \text{ m}^{-1}$  ( $2.40 \times 10^{-4} \text{ ft}^{-1}$ ) for the 2D model. Upon examination of Figure 4.3.3, it is evident that the cross-section model predicts a curvature ductility capacity of roughly 11 and a moment capacity of approximately 3000 kN-m (2200 kip-ft.).

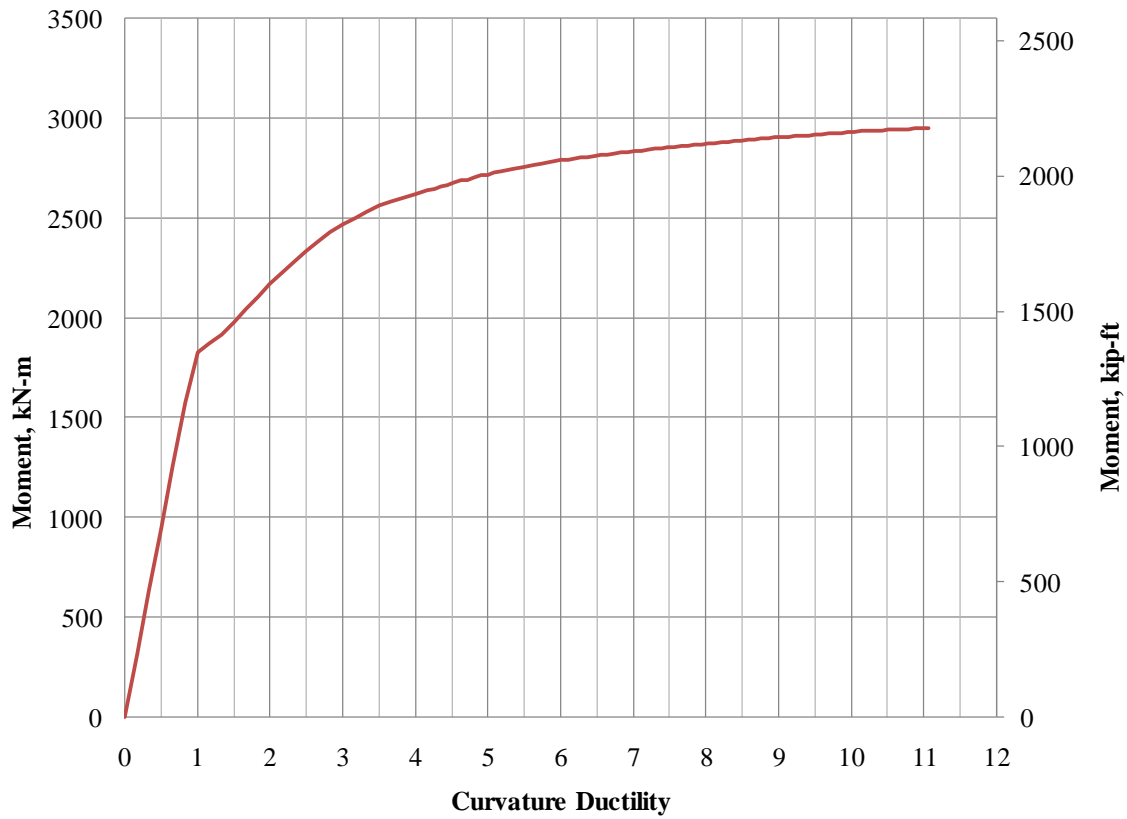


**Figure 4.3.3: Moment-Curvature Ductility Relationship for *In Situ* Pile**

## 4.4 ABAQUS/STANDARD MODELING

### 4.4.1 INTRODUCTION

The first overall step for modeling the *in situ* pile was to determine the sub-grade length of pile which needed to be included in order to minimize the size of the finite element model. In order to do so, the pile was modeled as a Winkler beam on an elastic foundation using LPILE Plus v5.0 (Ensoft, Inc., 2008). To determine the soil types to be used in both the ABAQUS and LPILE models, the available geotechnical data provided

by WSDOT was reviewed. Six standard penetration tests (SPT) were performed prior to the construction of the I-5 Ravenna Bridge in order to classify the soils beneath the superstructure and to obtain soil properties. The locations of the boreholes and the SPT data collected are provided in Appendix A.1. Since a full geotechnical report was not available, standard soils with well documented properties that were representative of the soils found near the I-5 Ravenna Bridge were used. Thus, the analyses utilized properties of Boston Blue Clay, a typical marine clay, and medium dense Ottawa Sand. In addition, it was assumed that the ground water table was located at a depth of 1.83 m (6 ft.). The LPILE analyses revealed that a sub-grade length of 3.66 m (12 ft.) was necessary based on the location of maximum moment and sub-grade deflection.

The critical state plasticity model within ABAQUS, which is an extension of the modified cam clay model, was used to model the behavior of the Boston Blue Clay. The critical state plasticity model uses strain rate decomposition where the total strain rate is decomposed into elastic and plastic strain rates. The model also requires that elastic behavior be defined using either traditional or porous elasticity, depending on the method employed to define the hardening rule. Thus, the model incorporates elastic theory, a yield surface, and flow and hardening rules, which define the change in the yield surface after yielding.

The yield surface of the critical state plasticity model is a function of the first three stress invariants, the slope of the critical state line, the initial size of the yield surface, the flow stress ratio of triaxial tension to triaxial compression, and a cap adjustment factor. The initial size of the yield surface can be defined either directly or indirectly via the hardening rule. The hardening rule is assumed to be a function of inelastic volumetric

strain and the plastic strain rate is defined by the associated flow rule. In this work, the initial size of the yield surface was defined indirectly by specifying the intercept of the virgin consolidation line in a plot of void ratio versus the logarithm of effective pressure. Hence, using the indirect method for specifying the initial yield surface size implies that an exponential hardening law is used and requires the use of porous elastic theory. In addition, the initial void ratio and vertical effective stress must be supplied as initial conditions in order to fully define the initial size of the yield surface at the beginning of the analysis.

#### 4.4.2 MODEL FORMULATION

##### 4.4.2.1 Prestressing Strands and Reinforcement Properties

An elasto-plastic constitutive model was used to define the behavior of the hoop reinforcement, longitudinal reinforcement, and prestressing strands. The input parameters for the steel constitutive models are presented in Table 4.4.1 and Table 4.4.2.

**Table 4.4.1: Prestressing Strand Input**

<b>Elastic Behavior</b>		
<b>Elastic Modulus</b>	190 GPa	27500 ksi
<b>Density</b>	77 kN/m <sup>3</sup>	490 pcf
<b>Poisson's Ratio</b>	0.3	
<b>Plastic Behavior</b>		
<b>Stress (MPa)</b>	<b>Stress (ksi)</b>	<b>Plastic Strain</b>
1465.0	212.5	0.0
1724.0	250.0	0.0273
6.9	1.0	0.0300

**Table 4.4.2: Longitudinal Rebar and Hoop Input**

<b>Elastic Behavior</b>		
<b>Elastic Modulus</b>	200 GPa	29000 ksi
<b>Density</b>	77 kN/m <sup>3</sup>	490 pcf
<b>Poisson's Ratio</b>	0.3	
<b>Plastic Behavior</b>		
<b>Stress (MPa)</b>	<b>Stress (ksi)</b>	<b>Plastic Strain</b>
276.0	40.0	0.0
310.0	45.0	0.0136
483.0	70.0	0.1186
6.9	1.0	0.1300

#### 4.4.2.2 Concrete Properties

Input parameters for the concrete constitutive model were defined using the method outlined in Section 3.3.2.1. As before, the five parameters to define the concrete damaged plasticity yield surface, flow rule, and hardening rule were taken as the recommended values (Dassault Systèmes SIMULIA, 2007). The input parameters to define the density and elastic properties are provided in Table 4.4.3. In addition, the parameters used to define compression hardening, tension stiffening, compression damage, and tensile damage are summarized in Table 4.4.4, Table 4.4.5, Table 4.4.6, and Table 4.4.7, respectively.

**Table 4.4.3: Concrete Density and Elastic Behavior Input**

<b>Elastic Modulus</b>	5034 ksi	34710 MPa
<b>Density</b>	145 pcf	22.8 kN/m <sup>3</sup>
<b>Poisson's Ratio</b>	0.15	

**Table 4.4.4: Concrete Compression Hardening Input**

<b>Stress (MPa)</b>	<b>Stress (psi)</b>	<b>Plastic Strain</b>
31.0	4500	0.0
53.8	7800	0.00158
17.9	2600	0.00251
2.2	320	0.00311

**Table 4.4.5: Concrete Tension Stiffening Input**

<b>Tensile</b>	606.3	4.18 MPa
<b>Fracture Energy</b>	0.683 lb/in	0.120 N/mm
<b>Crack Displacement Rate</b>	$1.0 \times 10^{-8}$ in/s	$2.54 \times 10^{-7}$ mm/s

**Table 4.4.6: Concrete Compression Damage Input**

<b>d<sub>c</sub></b>	<b>in</b>
0%	0.00000
21%	0.00170
72%	0.00238

**Table 4.4.7: Concrete Tension Damage Input**

<b>d<sub>t</sub></b>	<b>mm</b>	<b>in</b>
0%	0.0	0.0
50%	0.05715	0.00225
98%	0.11455	0.00451

#### 4.4.2.3 Boston Blue Clay Properties

As previously mentioned, the Boston Blue Clay was modeled using the critical state plasticity model available within ABAQUS. The material properties for the Boston Blue Clay were taken as those listed by Sathishbalamurugan (2004) and are provided in Table 4.4.8. The input parameters required to define its porous elastic behavior were specified based on the shear modulus of the clay. Thus, the required input parameters are the logarithmic bulk modulus ( $\kappa$ ), shear modulus ( $G$ ), and elastic tensile limit, which were defined as 0.03, 37 MPa (5.37 ksi), and 0 MPa (0 psi), respectively.

The required parameters to define the clay plasticity model when using the exponential hardening law are the logarithmic plastic bulk modulus ( $\lambda$ ), the stress ratio at critical state ( $M$ ), the initial yield surface size ( $a_o$ ), the yield surface size adjustment factor ( $\beta$ ), and the flow stress ratio of triaxial tension to triaxial compression ( $K$ ). The aforementioned parameters were taken as 0.15, 1.2, 0, 1.0, and 0.8, respectively. It should

be noted that the *intercept* option for defining the initial yield surface size as a function of void ratio was employed; hence, the initial yield surface size is calculated at the beginning of the analysis.

**Table 4.4.8: Properties of Boston Blue Clay (Murugaiah, 2004)**

Parameter	Value
Elastic Modulus, E	100 Mpa (14.5 ksi)
Shear Modulus, G	37 Mpa (5.37 ksi)
Dry Density, $\rho_d$	17.7 kN/m <sup>3</sup> (112 lb/ft <sup>3</sup> )
Saturated Density, $\rho_{sat}$	22.6 kN/m <sup>3</sup> (144 lb/ft <sup>3</sup> )
Reference Pressure, $p'_1$	1 MPa (145 psi)
Poisson's Ratio, $\nu$	0.35
Porosity, $\eta$	0.5
Friction Angle, $\phi$	30°
Slope of Elastic Swelling Line, $\kappa$	0.03
Slope of Normal Consolidation Line, $\lambda$	0.15
Soil Constant, M	1.2
Specific Volume at Reference Pressure, $v_1$	2.3

The size of the initial yield surface is computed within ABAQUS using Equation 4-1 if the *intercept* option is specified.

$$a_o = \frac{1}{2} \exp\left(\frac{e_1 - e_0 - \kappa \ln p_o}{\lambda - \kappa}\right) \quad (4-1)$$

where:

$e_1$  = Void ratio axis intercept of virgin compression line

$e_0$  = Initial void ratio of the soil

$p_o$  = Initial value of the equivalent hydrostatic pressure stress (Force/Length<sup>2</sup>)

$\lambda$  = Logarithmic plastic bulk modulus

$\kappa$  = Logarithmic bulk modulus

The initial void ratios for Boston Blue Clay were obtained from a plot of void ratio versus depth, as illustrated in Figure 4.4.1. The void ratio axis intercept was obtained by



extrapolating the slope of the virgin compression line such that it intersects the void ratio axis in a plot of void ratio vs. the logarithm of effective pressure, as depicted in Figure 4.4.2.

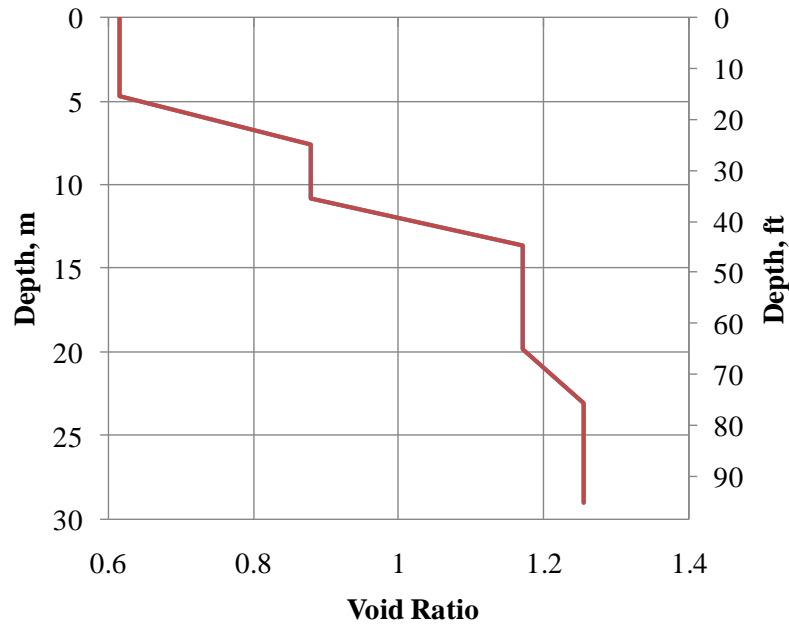


**Figure 4.4.1: Void Ratio vs. Depth, Boston Blue Clay**

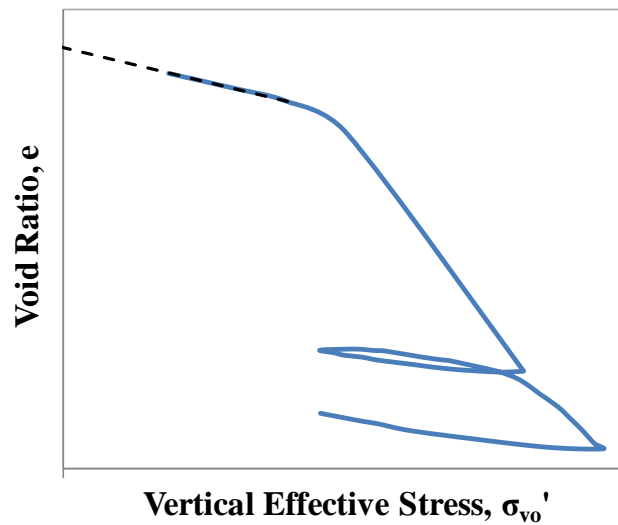


**Figure 4.4.2: Schematic for Determining Void Ratio Axis Intercept**

Using this method, the value of the void ratio axis intercept,  $e_I$ , was found to be 1.45.

The initial value of equivalent hydrostatic pressure was calculated using Equation 4-2.

$$p_o = \frac{1}{3}(\sigma'_{vo} - K_o \cdot \sigma'_{vo}) \quad (4-2)$$

where:

$\sigma'_{vo}$  = Vertical Effective Stress (Force/Length<sup>2</sup>)

$K_o$  = Lateral earth pressure coefficient at rest

The lateral earth pressure coefficient at rest was calculated based on a standard geotechnical reference, as presented in Equation 4-3 (Das, 2004), where  $\varphi$  is the soil friction angle.

$$K_o \approx 1 - \sin(\varphi) \quad (4-3)$$

#### 4.4.2.4 Ottawa Sand Properties

The Ottawa Sand was modeled as a linear elastic material. The material properties used were obtained from standard geotechnical references (Das, 2004; Holtz & Kovacs, 1981) and are presented in Table 4.4.9.

**Table 4.4.9: Summary of Ottawa Sand Properties**

Parameter	Value
Elastic Modulus, E	55.2 Mpa (8.0 ksi)
Dry Density, $\rho_d$	18.6 kN/m <sup>3</sup> (118 lb/ft <sup>3</sup> )
Saturated Density, $\rho_{sat}$	21.1 kN/m <sup>3</sup> (134.3 lb/ft <sup>3</sup> )
Poisson's Ratio, $\nu$	0.45
Friction Angle, $\varphi$	34°

#### 4.4.3 MODEL GEOMETRY

The model of the *in situ* pile was comprised of five major parts: the pile, soil, longitudinal reinforcement, transverse reinforcement, and prestressing tendons. Overviews of the assembled pile model and the reinforcing/prestressing steel layout are provided in Figure 4.4.3 and Figure 4.4.4, respectively. The model utilized a *y-z* plane of symmetry, parallel to the direction of lateral loading. The pile measured 9.14 m (30 ft.) in overall length with 5.5 m (18 ft.) above ground and 3.66m (12 ft.) below ground. Finite elements for the pile consisted of standard eight-node linear hexahedral 3D continuum elements with full integration. It was meshed such that the approximate global size of the elements measured 42 mm (1.66 in.) in order to have three elements through the thickness. To eliminate unnecessary material nonlinearity at points of support, each end of the pile was modeled as linearly elastic, with elastic properties equivalent to those listed in Table 4.4.3.

The transverse reinforcement was simplified into 88 discrete hoops having a diameter of 1090 mm (43 in.) and the hoops were spaced according to details provided in Section 4.2. Six prestressing tendons and six longitudinal reinforcing bars were included in the model and spaced with radial symmetry about the longitudinal axis according to details in Section 4.2. The hoops, prestressing strands, and longitudinal reinforcing bars were meshed using standard two node 3D truss elements with an approximate element length of 100 mm (4 in.). The cross-sectional area of the hoops, strands, and longitudinal rebars were specified as 31.7 mm<sup>2</sup> (0.0491 in.<sup>2</sup>), 224.5 mm<sup>2</sup> (0.348 in.<sup>2</sup>), and 200 mm<sup>2</sup> (0.31 in.<sup>2</sup>), respectively.

The outer boundary of the soil measured 3.66 m (12 ft.) in diameter. The finite elements for the soil consisted of standard-eight node linear hexahedral 3D continuum elements with full integration. A biased mesh was used for the soil such that the soil elements near the pile surface were smaller than those in the far field region. All of the soil elements had a constant thickness of 152 mm (6 in.). The soil was partitioned into twelve, 305 mm (12 in.) thick layers to facilitate application of initial conditions. The top six and bottom six soil layers were defined as element sets to represent the dry and saturated regions of the soil, respectively. It is important to note that, although the piles used in the I-5 Ravenna Bridge were driven, the soil within the hollow core of the pile was neglected since it may have contracted over the past decades and would thus be unable to provide internal confining pressure. This was considered to be a conservative assumption with respect to the influence on failure mechanisms.

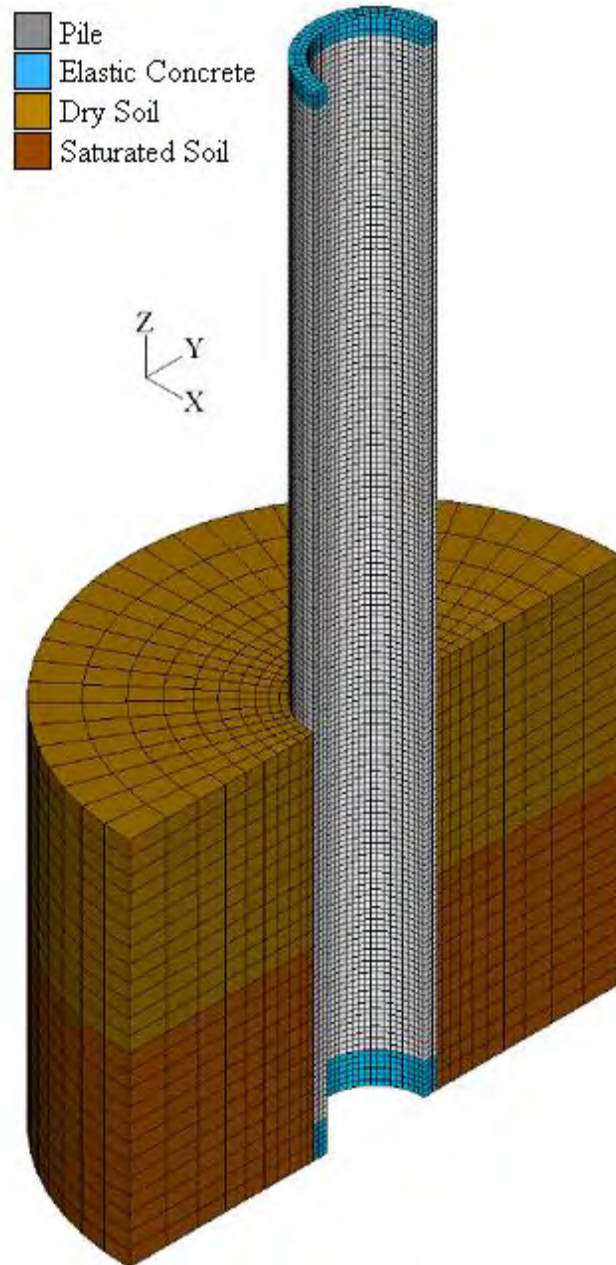


**Figure 4.4.3: *In Situ* Pile Model Assembly and Mesh**

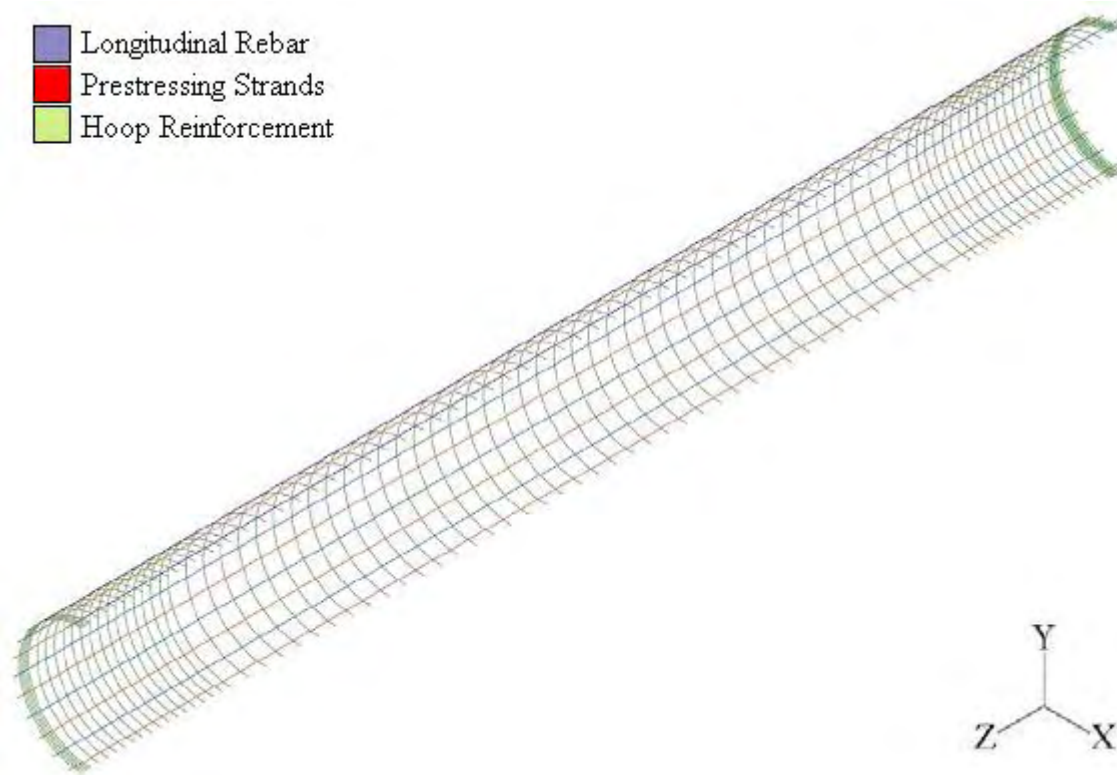


**Figure 4.4.4: *In Situ* Pile Reinforcement and Tendon Assembly**

#### 4.4.4 BOUNDARY & INITIAL CONDITIONS

As previously stated, the pile was modeled as a cantilever, partially surrounded by soil, with a longitudinal plane of symmetry. The  $U_x$ ,  $U_y$  and  $U_z$  degrees of freedom (DOF) were constrained for all of the nodes at the base of pile to simulate a cantilevered support. The  $U_x$  and  $U_y$  DOF were constrained for all of the nodes on the outer perimeter of the soil surface and the  $U_z$  DOF was constrained for all of the nodes on the bottom of the soil. To facilitate symmetry, the  $U_x$  DOF was constrained for all of the nodes on the plane of symmetry. An overview of the imposed boundary conditions is presented in Figure 4.4.5. To facilitate generation of load-displacement plots, displacement at the top of the pile in the y-direction was monitored during each increment of each loading step.

Note that the origin of the global coordinate system was located at the intersection of the base of the pile and the longitudinal centroidal axis of the pile.

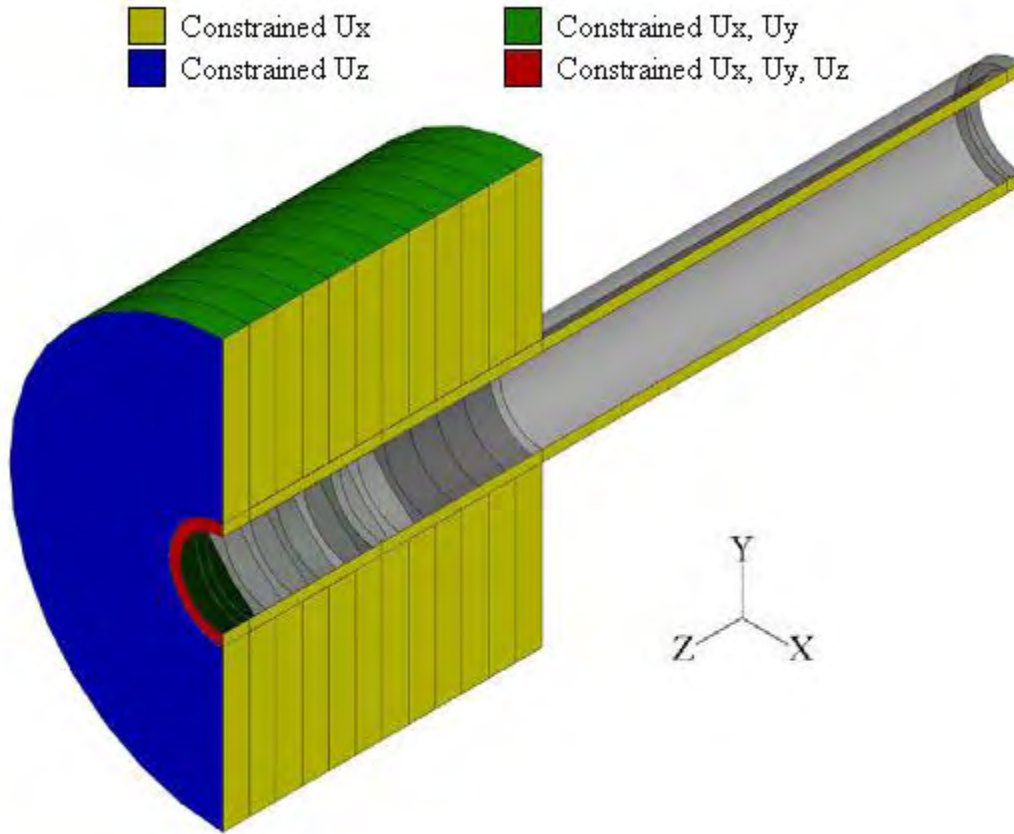


**Figure 4.4.5: *In Situ* Pile Boundary Conditions**

To facilitate the application of the 270 kN (61 kips) prestressing force, a stress-type initial condition was utilized to apply an initial stress to the six tendons at a magnitude of 1210 MPa (175.3 ksi) in the  $z$ -direction. Since the constitutive model for the Boston Blue Clay was defined using porous elasticity, exponential hardening, and the intercept option, the initial stresses and void ratios within the soil must be specified to generate the initial yield surface with respect to depth (Dassault Systèmes SIMULIA, 2007). Therefore, vertical effective stress and initial void ratios were defined using the geostatic stress and ratio-type initial conditions. To define the distribution of vertical effective stress using

the geostatic stress initial condition, the user must define seven parameters: element number or element set, the vertical coordinate and value for the first vertical effective stress, the vertical coordinate and value for the second vertical effective stress, and the lateral stress coefficient in the  $x$ - and  $y$ -directions ( $K_x$  and  $K_y$ , respectively). The input parameters used to define the initial geostatic stresses are summarized in Table 4.4.10. In addition, the computed approximate values for the lateral earth pressure coefficient for Boston Blue Clay well agreed with past experimental test data (Ling, et al., 2002).


**Table 4.4.10: Input Parameters for Initial Geostatic Stresses**

Element Set	Elevation	Stress	$K_x = K_y$
Dry Soil	3658 mm (144 in.)	0 kPa (0 psi)	0.5
	1829 mm (72 in.)	-32.3 kPa (-4.68 psi)	
Saturated Soil	1829 mm (72 in.)	-32.3 kPa (-4.68 psi)	0.5
	0 mm (0 in.)	-55.6 kPa (-8.07 psi)	

The initial void ratio can be specified to remain constant or vary linearly with depth for a user specified set of nodes. Since the soil was discretized into twelve layers, the initial void ratio for each layer of soil was assumed constant. Therefore, to define a constant initial void ratio, the user must specify the node set and value for the initial void ratio. The input parameters used to define the initial void ratios are provided in Table 4.4.11. It should be noted that initial void ratios and geostatic stresses were not defined in the case of the *in situ* pile embedded in medium dense sand since the soil was assumed to be a linear elastic material.



**Table 4.4.11: Input Parameters for Initial Void Ratio**

	Node Set	Void Ratio, $e_o$
	Layer 1	0.616
	Layer 2	0.616
	Layer 3	0.616
	Layer 4	0.616
	Layer 5	0.651
	Layer 6	0.744
	Layer 7	0.834
	Layer 8	0.880
	Layer 9	0.880
	Layer 10	0.880
	Layer 11	0.910
	Layer 12	1.012

#### 4.4.5 *LOADING*

Loading was applied in three steps: equilibrium, axial loading, and the lateral push. The loading increment was held constant through all steps of the analysis and the minimum time increment was specified as 1e-8. A small minimum time increment was used to ensure that the analysis would be carried out long enough such that failure could be quantified. The equilibrium step was used to allow for geostatic equilibrium in the soil and equilibrium of the pile due to prestressing. The axial load step was used to apply the 1183 kN (266 kips) axial load at the free end of the pile as a uniformly distributed non-following surface traction in the negative  $z$ -direction. The lateral push step was used to apply a lateral load of 1200 kN (270 kips) at the free end of the pile as a uniformly distributed surface traction in the negative  $y$ -direction. The lateral load applied was based on the expected moment capacity of the pile obtained from XTRACT. Nonlinear geometry due to large deformations and deflections was included in all three steps of the analysis. In addition, the discontinuous analysis control was used during each step since

the analysis incorporates frictional sliding and concrete cracking (Dassault Systèmes SIMULIA, 2007).

#### 4.4.6 SOIL-PILE INTERACTION PROPERTIES

The soil-pile interaction for the *in situ* model was simulated using a surface-to-surface based contact definition. The contact definition utilized surface-to-surface discretization with finite sliding. The contact constraints were imposed on nodes of the contact surfaces with no adjustment to slave or surface nodes. Contact interactions within ABAQUS require the user to specify a master and slave surface, with the master surface being defined on the stiffer body of the two in contact. Thus, the master surface was defined as the region of the outer surface of the pile in contact with the soil and the slave surface was defined as the inner surface of the soil, as depicted in Figure 4.4.6.

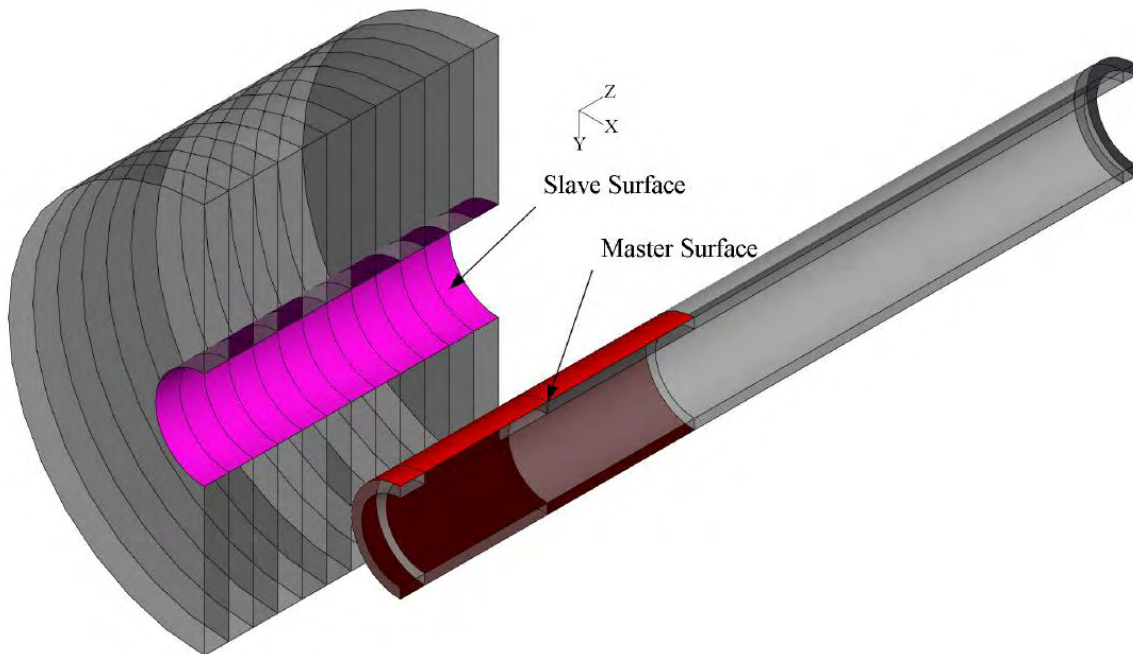


**Figure 4.4.6: *In Situ* Pile Contact Surface Definitions**

Two contact interaction properties were used during the analysis of the *in situ* pile, and will be referred to as the *initial* and *final* interaction properties. The *initial* interaction was defined using frictionless tangential behavior and Augmented Lagrange normal behavior. The surface normal contact allowed for separation after contact and was defined using the default contact stiffnesses. The initial interaction was utilized during the equilibrium and axial load steps of the analysis. The purpose of the initial interaction was to minimize shear stresses transferred to the soil from the pile during equilibrium of the applied prestress and axial load. That is to say, the frictionless tangential interaction allowed the soil and pile to achieve equilibrium independently.

The *final* interaction was defined using an isotropic penalty friction formulation for tangential behavior and Augmented Lagrange normal contact behavior. As with the initial interaction, the surface normal contact allowed for separation after contact and was defined using the default contact stiffnesses. The tangential friction interaction was slip-rate and contact-pressure independent with coefficients of friction of 0.364 and 0.418 for the Boston Blue Clay and Ottawa Sand, respectively. The coefficients of friction were calculated per Equation 4-4 (Useugi, et al., 1988).

$$\mu_{\text{tan}} = \tan\left(\frac{2}{3} \cdot \varphi\right) \quad (4-4)$$

No maximum shear stress between the soil and pile was specified for either analysis since shear failure of the soil was not expected, or observed. It should be noted that all other options not discussed herein were taken as the default values within ABAQUS.

#### 4.4.7 RESULTS, BOSTON BLUE CLAY

As with the calibrated models, the performance of both *in situ* pile models was governed by the tensile capacity of the concrete. Once tensile cracks extended through the tension side of the pile a nearly linear response followed until compressive failure began at the opposite pile surface. A general overview of the deformed shape of the pile is provided in Figure 4.4.7.

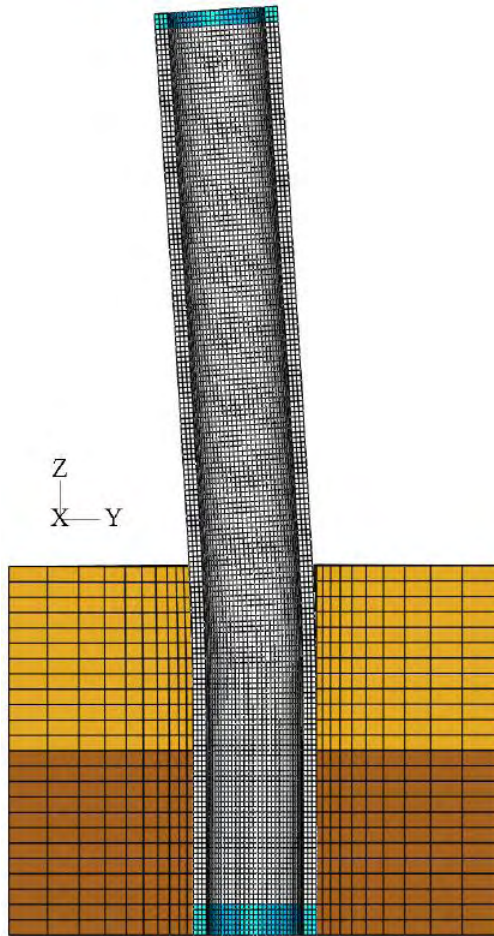


**Figure 4.4.7: *In Situ* Pile Deformed Shape (Boston Blue Clay)**

Failure in the pile was characterized by inspection of the compressive damage distribution in the pile, as was the case for the calibrated models. Failure was said to occur when compressive damage exceeded 21 percent, the value corresponding to the

multiaxial spalling strain, through the depth of cover concrete. The distribution of compression damage in the pile cross-section can be seen in Figure 4.4.8 and Figure 4.4.9. As a reference, the pile elements measure approximately 50.8 mm (2 in.) in each direction. By inspection of Figure 4.4.8 and Figure 4.4.9, it is evident that the compression damage in the pile wall has exceeded the 21 percent limit indicating that the concrete has spalled to the depth of reinforcing steel and prestressing tendons over a region measuring approximately 1400 mm (55 in.) in length. The plastic hinge length was taken as the region of longitudinal reinforcement that yielded in tension at failure. The plastic hinge length was found to measure  $2.88-D$  in length and was centered 710 mm (28 in.) below the soil surface.

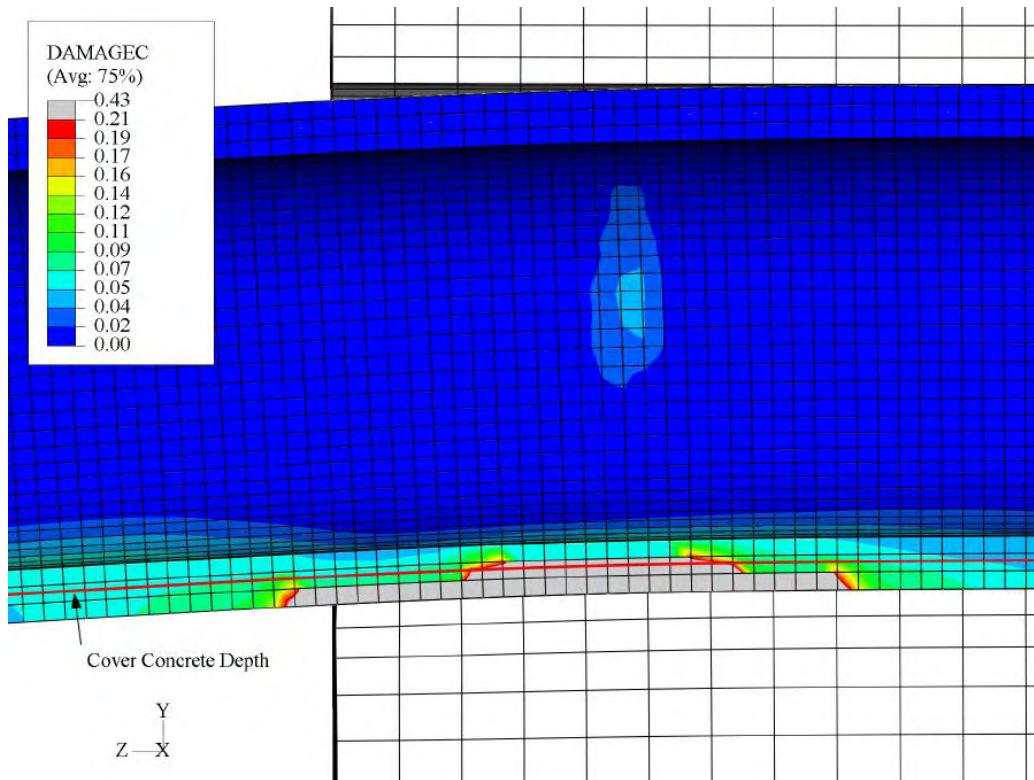


**Figure 4.4.8: Pile Compression Damage, Side View (Boston Blue Clay)**

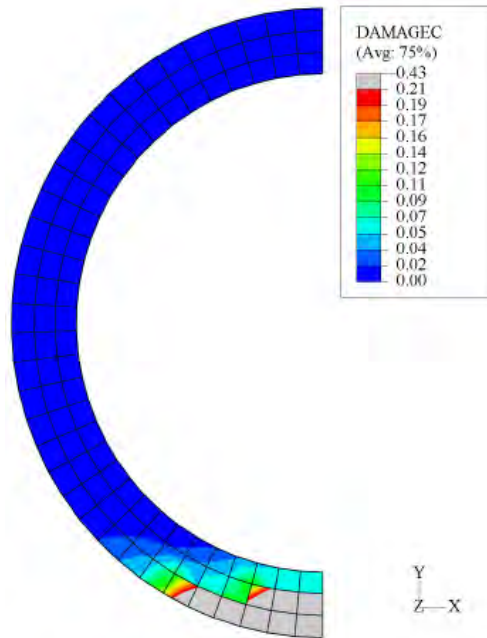


**Figure 4.4.9: Pile Compression Damage, End View (Boston Blue Clay)**

In order to understand the performance of the pile if failure is defined based on the state of uniaxial strain in the pile wall, the distribution of the  $z$ -component of inelastic strain was plotted, as shown in Figure 4.4.10. In this case, failure was said to occur when the  $z$ -component of inelastic strain exceeded 0.00158 through the depth of cover concrete. By inspection of Figure 4.4.10, it is evident that the region of spalled concrete based on this definition of failure measures roughly 1070 mm (42 in.).



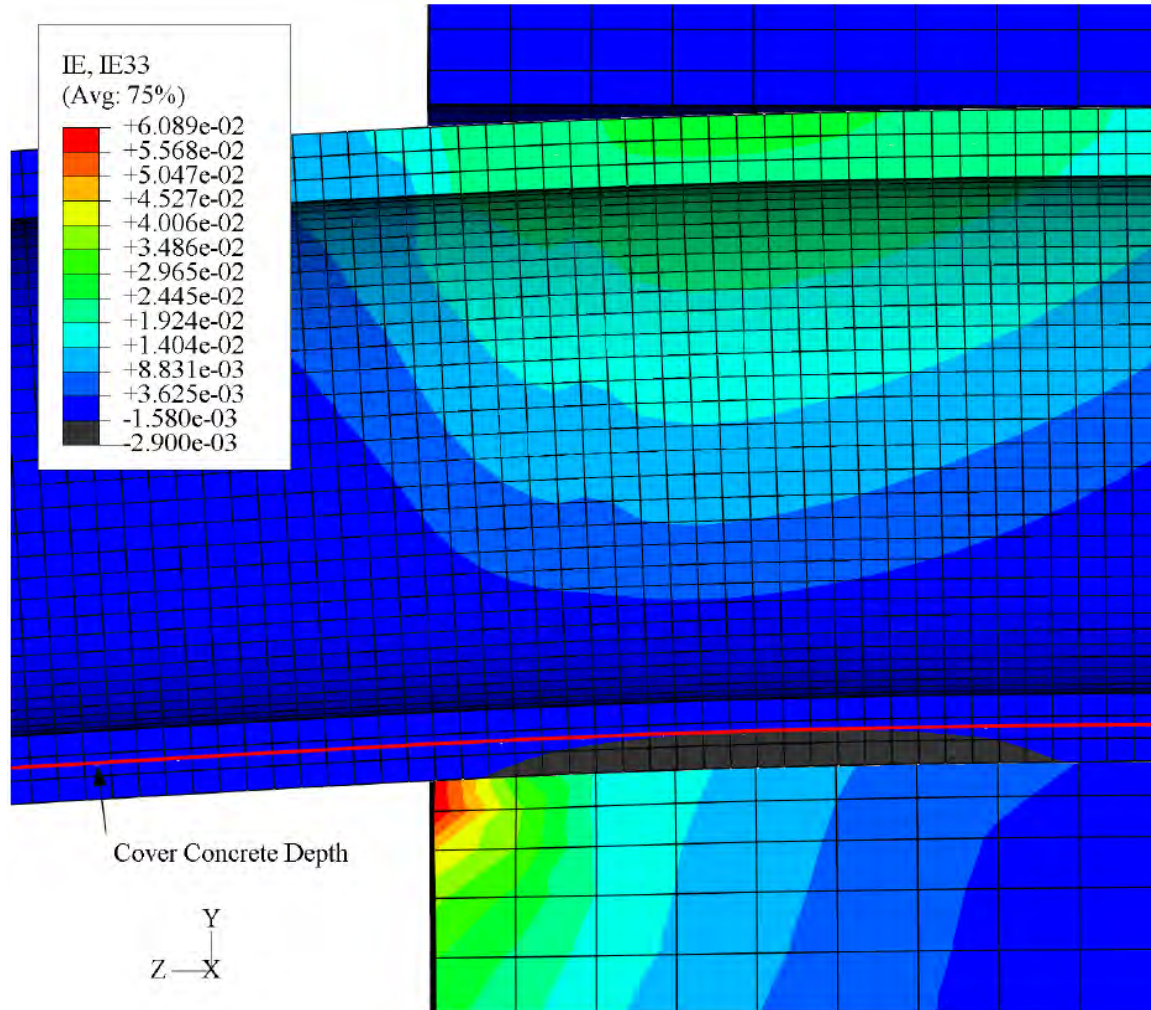


**Figure 4.4.10: Inelastic Strain Distribution, z-component (Boston Blue Clay)**

The two failure definitions are compared in terms of the applied shear force versus pile head displacement ductility, as shown in Figure 4.4.11. By inspection of Figure 4.4.11, one can see that the prediction for displacement ductility is approximately 4.5 if failure is defined using the axial component of inelastic strain (uniaxial failure limit). In comparison, if failure is defined based on the compression damage (multiaxial failure limit), displacement ductility is predicted as 6.5.

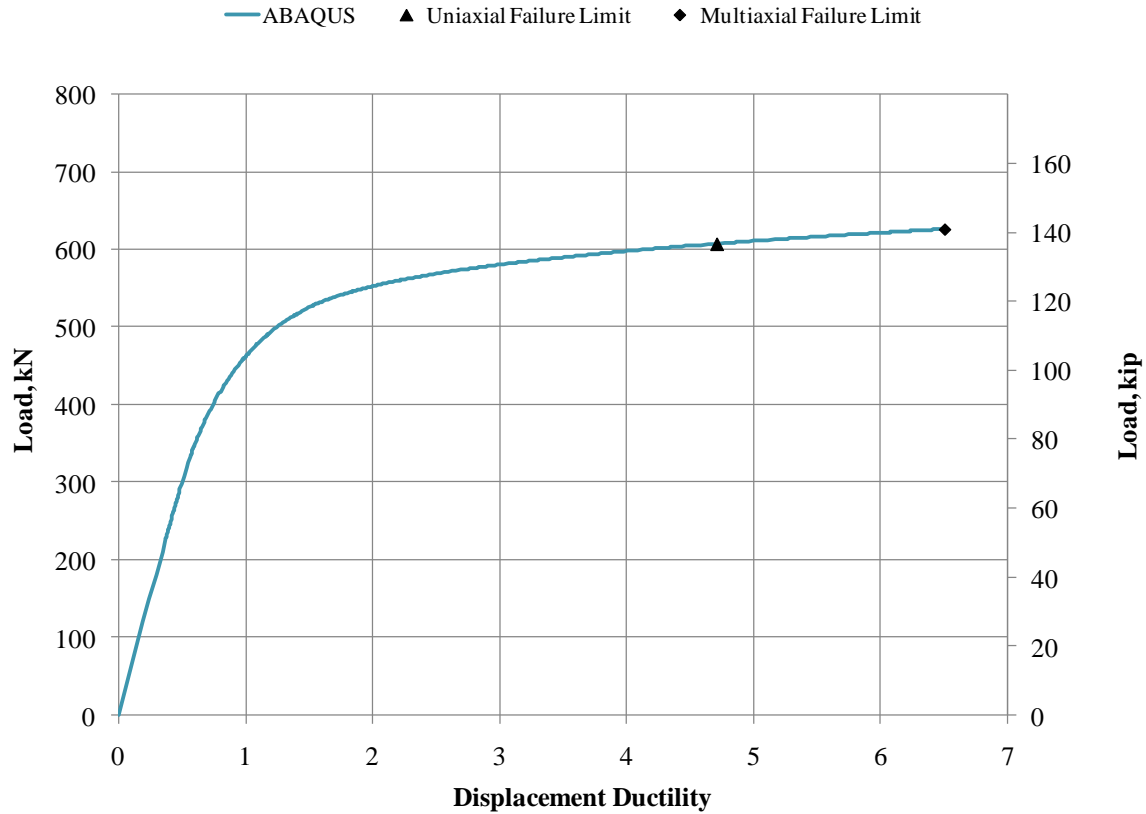


**Figure 4.4.11: Comparison of Failure Measures**

As mentioned in Section 4.1, the two research objectives for the *in situ* piles are to understand the influence of confining pressure from the soil on the exterior surface of the pile, and determine whether or not confining pressure is great enough such that the cover concrete in the pile behaves as confined concrete. In order to quantify the confining pressure supplied to the pile around the plastic hinge region, a contour plot of the normal component of surface contact pressure on the inner surface of the soil was generated, as shown in Figure 4.4.12. Note that Figure 4.4.12 depicts only the soil surrounding the region of spalled concrete based on compressive damage failure.



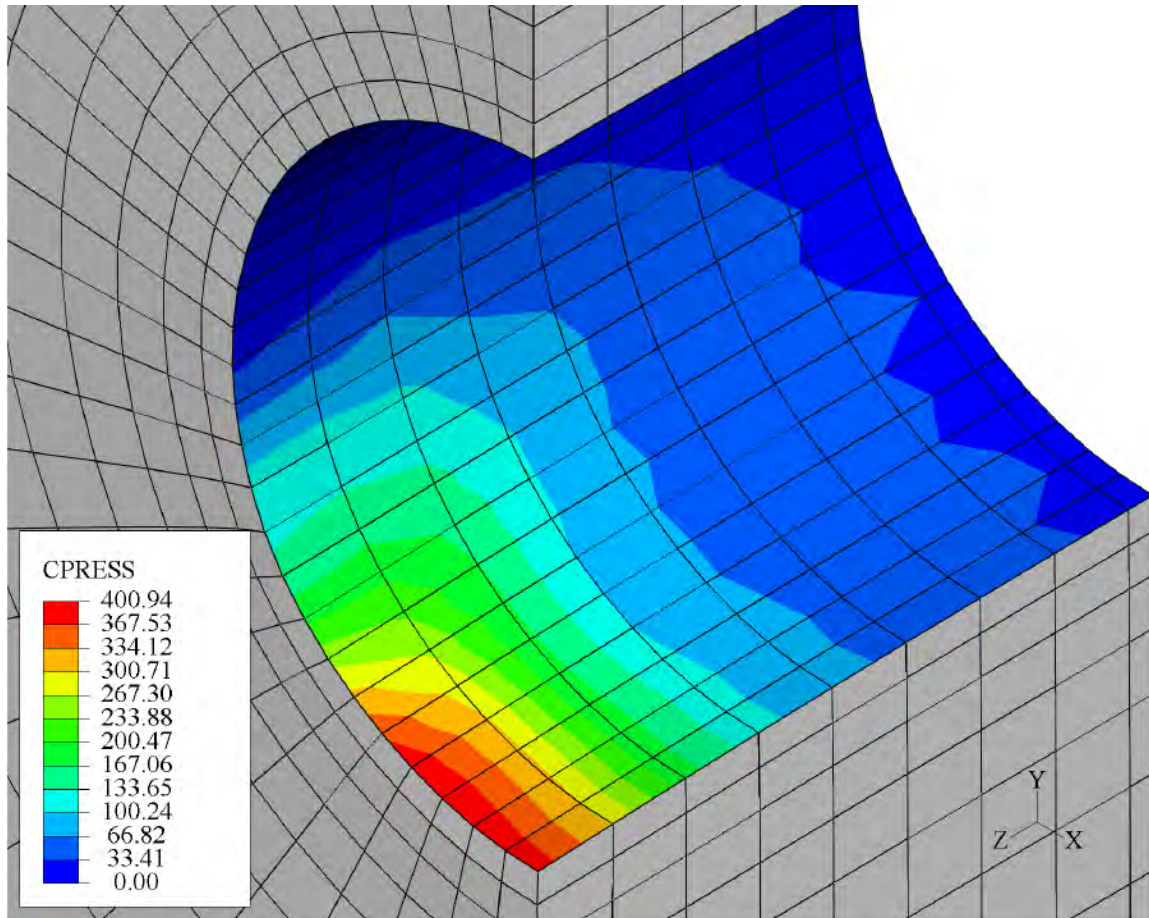


**Figure 4.4.12: Soil Confining Pressure on Plastic Hinge Region (Boston Blue Clay)**

By equating forces from lateral confining pressures to hoop tension forces, as in the Mander model (Mander, et. al, 1988), and assuming an average confining stress per layer of soil elements, the increase in concrete compressive strength can be approximated by determining an equivalent amount of transverse reinforcement per layer of soil elements. Hence, depending on the confinement effectiveness coefficient, it was found that the concrete compressive strength would increase by merely 0.1 – 0.2 percent. Therefore, no appreciable increase in compressive strength of the concrete occurs due to confining pressures supplied by the Boston Blue Clay.

#### 4.4.8 RESULTS, OTTAWA SAND

Observations similar to those for the pile embedded in Boston Blue Clay were made for the pile embedded in Ottawa Sand. The response of the pile was controlled by tensile cracking and, as before, failure was said to occur when compressive damage exceeded 21 percent. The distribution of compression damage in the pile wall is presented in Figure 4.4.13 and Figure 4.4.14.

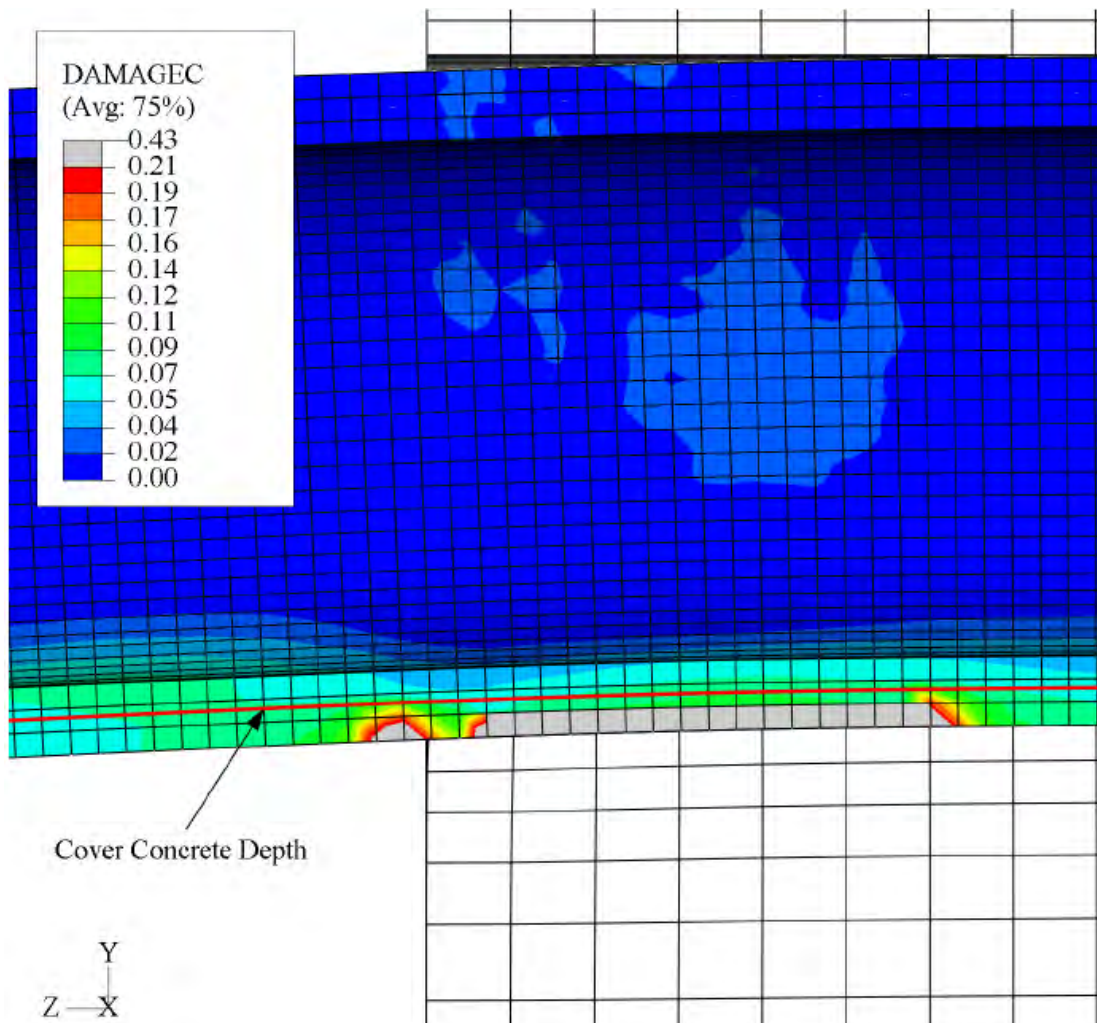


**Figure 4.4.13: Pile Compression Damage, Side View (Ottawa Sand)**

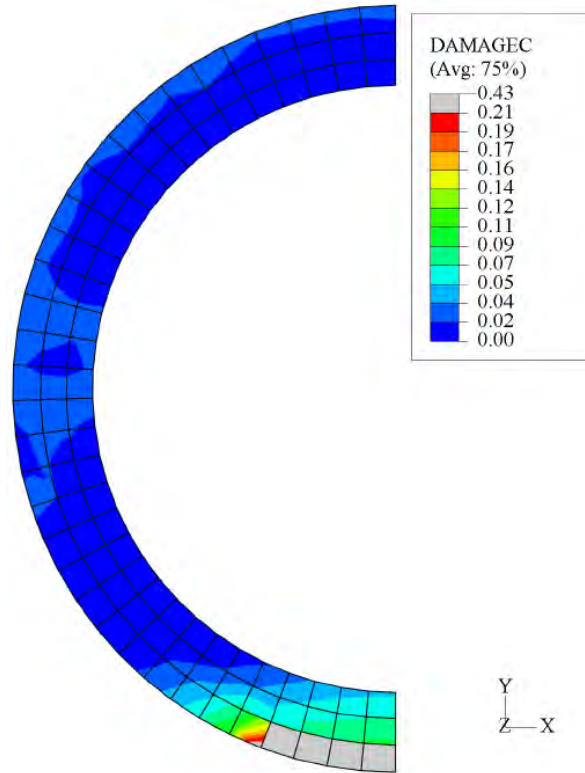


**Figure 4.4.14: Pile Compression Damage, End View (Ottawa Sand)**

By inspection of Figure 4.4.13 and Figure 4.4.14, it is evident that the compression damage in the pile wall has exceeded the 21 percent limit indicating that the concrete has spalled through the first layer of concrete elements over a region measuring approximately 1070 mm (42 in.) in length. The plastic hinge length was found to measure  $3.0\text{-}D$  in length and was centered approximately 510 mm (20 in.) below the soil surface.

As before, in order to quantify the increase in concrete compressive strength based on confining pressure provided by the soil, the surface normal contact pressure distribution was inspected. Figure 4.4.15 shows the distribution of the normal component of surface contact pressure for the soil surrounding the region of spalled concrete based on compressive damage failure. Using the method discussed in the previous section it was found that, depending on the confinement effectiveness coefficient, the concrete

compressive strength would increase by 0.08 – 0.3 percent. Thus, as with the pile embedded in Boston Blue Clay, no appreciable increase in compressive strength of the concrete occurs due to confining pressures supplied by the Ottawa Sand.

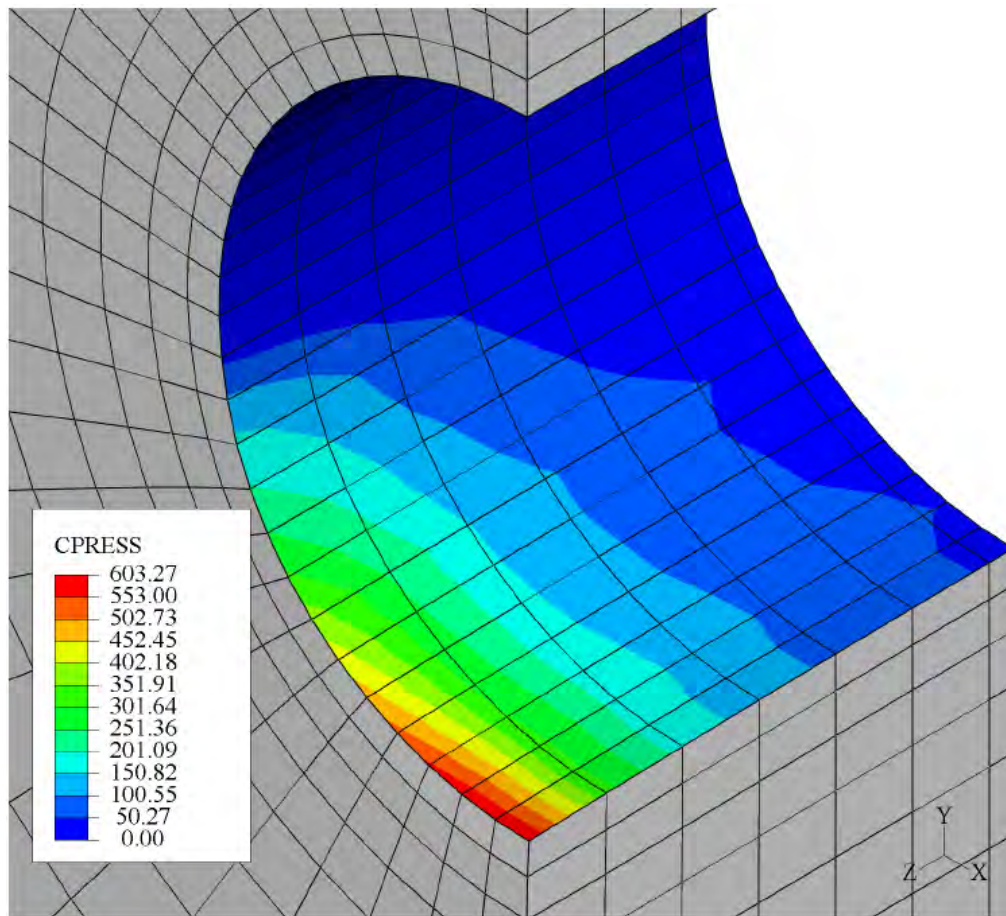


**Figure 4.4.15: Soil Confining Pressure on Plastic Hinge Region (Ottawa Sand)**



## 4.5 SAP2000 MODELING

The SAP2000 beam models were generated in order to understand if simplified analytical methods commonly used in design reasonably approximate the response of the 3D finite element model. The pile was modeled as a Winkler beam on a nonlinear elastic foundation. In order to accurately represent the 3D finite element model, the pile was modeled using the above ground and embedded lengths specified in Section 4.4.3. The beam model was generated using the methodology outlined in Section 3.4, with one exception. Although the method outlined in Section 3.4 utilized a P-M type hinge, the plastic hinge definition can be defined solely as a function of the effective moment-curvature response since the axial load remains constant throughout the static analyses. Therefore, the plastic hinge was defined as a symmetric M3 type hinge rather than a symmetric P-M type hinge.

### 4.5.1 FOUNDATION MODELING

The soil surrounding the pile was modeled as a Winkler foundation comprised of 18 nonlinear elastic springs. The foundation was modeled using uniform soft, medium, or stiff clay with the ground water table located at 1.83 m (6 ft.) below the soil surface. The foundation stiffness was obtained from pressure-displacement ( $p$ - $y$ ) analyses using LPILE Plus version 5.0 (Ensoft, Inc., 2008). The pile measured 13.7 m (45 ft.) in overall length with an above ground height of 5.5 m (18 ft.), corresponding to an average overall length and embedment depth of the *in situ* piles. The *in situ* pile length was modeled in LPILE in order to accurately capture the  $p$ - $y$  response of the top 3.66 m (12 ft.) embedded length, which is the region of interest. Static loading was applied to the pile in the form of a 4.45 kN (1 kips) lateral load and 1180 kN (266 kips) axial load. It is important to note

that the  $p$ - $y$  response is independent of the magnitude of the lateral load. The clay was modeled in LPILE using the material formulation for stiff clay without free water. The material input used for the LPILE analyses is presented in Table 4.5.1, where  $\gamma_d$  is the dry unit weight,  $\gamma'$  is the buoyant unit weight,  $c$  is the undrained shear strength, and  $\varepsilon_{50}$  is the strain at which 50 percent of the undrained shear strength is developed. It is important to note that the input parameters specified for the soft clay were specified such that they would represent Boston Blue Clay. In addition, the input parameters for medium and stiff clay were specified based on recommendations in the LPILE user's manual (Ensoft, Inc., 2008).

**Table 4.5.1: LPILE Input Parameters for Soft, Medium, and Stiff Clay**

Parameter	Soft Clay	Medium Clay	Stiff Clay
$\gamma_d$	17.6 kN/m <sup>3</sup> (0.065 lb/in <sup>3</sup> )	17.6 kN/m <sup>3</sup> (0.065 lb/in <sup>3</sup> )	17.6 kN/m <sup>3</sup> (0.065 lb/in <sup>3</sup> )
$\gamma'$	12.8 kN/m <sup>3</sup> (0.047 lb/in <sup>3</sup> )	12.8 kN/m <sup>3</sup> (0.047 lb/in <sup>3</sup> )	12.8 kN/m <sup>3</sup> (0.047 lb/in <sup>3</sup> )
$c$	20.0 kPa (2.9 psi)	47.8 kPa (6.94 psi)	95.8 kPa (13.9 psi)
$\varepsilon_{50}$	0.02	0.01	0.007

Pressure-displacement output was requested at every 152 mm (6 in.) of depth in the soil to a depth 1.98 m (6.5 ft.), and at depths of 2.29, 2.59, 2.90, 3.05, and 3.35 m (7.5, 8.5, 9.5, 10, 11, and 12 ft., respectively). The  $p$ - $y$  results from LPILE and calculated nonlinear force-displacement responses used in the beam models are provided in Appendix B. The nonlinear force-displacement responses were calculated using the methodology outlined by Priestley, et al. (1996).

#### 4.5.2 PLASTIC HINGE DEFINITION

As previously mentioned, the pile was modeled as a Winkler beam on a nonlinear elastic foundation with an axial load of 1180 kN (266 kips) and 4.45 kN (1 kips) lateral load applied at the free end. It is also important to note that the magnitude of the lateral

load does not have an effect on the response from a nonlinear pushover analysis. The model consisted of two beam elements to model the above ground and embedded lengths of the pile, a M3 type point plastic hinge located at 710 mm (28 in.) below the ground surface, and 18 nonlinear elastic springs to model the foundation. Note that the location and length of the plastic hinge were not modified during any of the simplified analyses.

The M3 type hinge is defined in terms of the effective yield moment, effective yield curvature, curvature ductility, and the overstrength factor corresponding to the applied axial load. The overstrength factor is defined as the ratio of the effective moment at failure to the effective moment at yielding. The input parameters to define the M3 type plastic hinge are presented in Table 4.5.2.

**Table 4.5.2: SAP2000 M3 Hinge Input Parameters**

Moment		Curvature	
kN-m	kip-in.	1/m	1/in.
0	0	0	0
2794	24730	0	0
2945	26065	8.68E-03	2.20E-04
559	4946	8.68E-03	2.20E-04
559	4946	1.30E-02	3.31E-04

Note: Symmetric response for negative moment

The plastic hinge lengths specified for the analyses were based on results from ABAQUS and Caltrans Seismic Design Criteria recommendations for non-cased Type I pile shafts (Caltrans, 2006). Thus, the plastic hinge length for the pile embedded in Boston Blue Clay was taken as  $2.88-D$  from ABAQUS, or  $1.40-D$  from Caltrans recommendations. An overview of the beam model is presented in Figure 4.5.1.

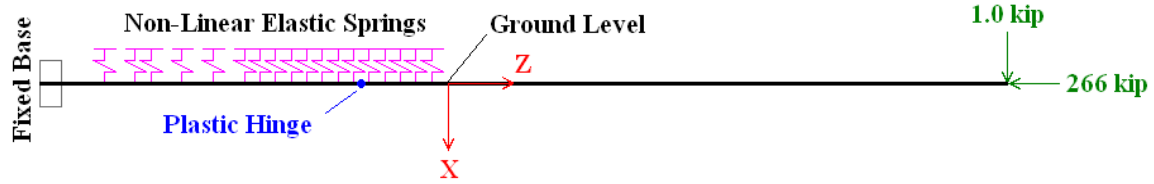


**Figure 4.5.1: SAP2000 Beam Model of *In Situ* Pile**

#### 4.5.3 RESULTS

The force-displacement ductility responses from the nonlinear pushover analyses for soft, medium, and stiff clay are presented in Figure 4.5.2. One key observation is that the response, regardless of foundation stiffness, is elasto-plastic. This is due to the fact that the inelastic behavior of the beam model is governed by an elasto-plastic effective moment-curvature response obtained from XTRACT. Upon examination of Figure 4.5.2, it is evident that the foundation stiffness has negligible effect on the response of the pile beam model when the plastic hinge length and location are unaltered. The comparison of the three force-displacement ductility response curves does, however, illustrate that the foundation stiffness can affect the prediction of maximum displacement ductility. Furthermore, as the foundation stiffness increases the maximum displacement ductility also increases, but not appreciably in this case.



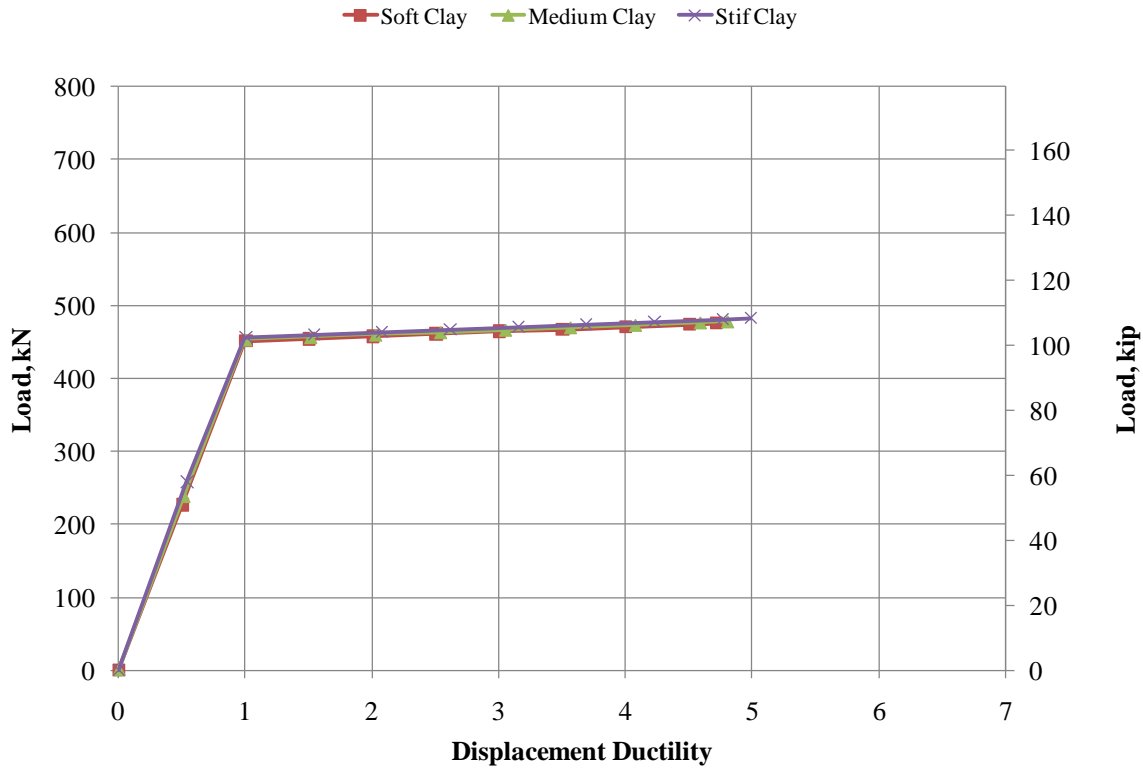


**Figure 4.5.2: Effect of Varying Foundation Stiffness,  $L_p = 1.4-D$**

The effect of varying the plastic hinge length from  $2.88-D$  to  $1.40-D$  for the soft clay foundation is illustrated in Figure 4.5.3. Upon examination, Figure 4.5.3 clearly illustrates that as the plastic hinge length is increased, the maximum displacement ductility is increased, as was the case in Section 3.4.3. Furthermore, if the plastic hinge length is specified per Caltrans recommendations, the predicted displacement ductility is approximately 60 percent of that predicted using a plastic hinge length based on results from the finite element model. Overall, the Caltrans recommendation provides a conservative estimate for the plastic hinge length of the hollow core piles.

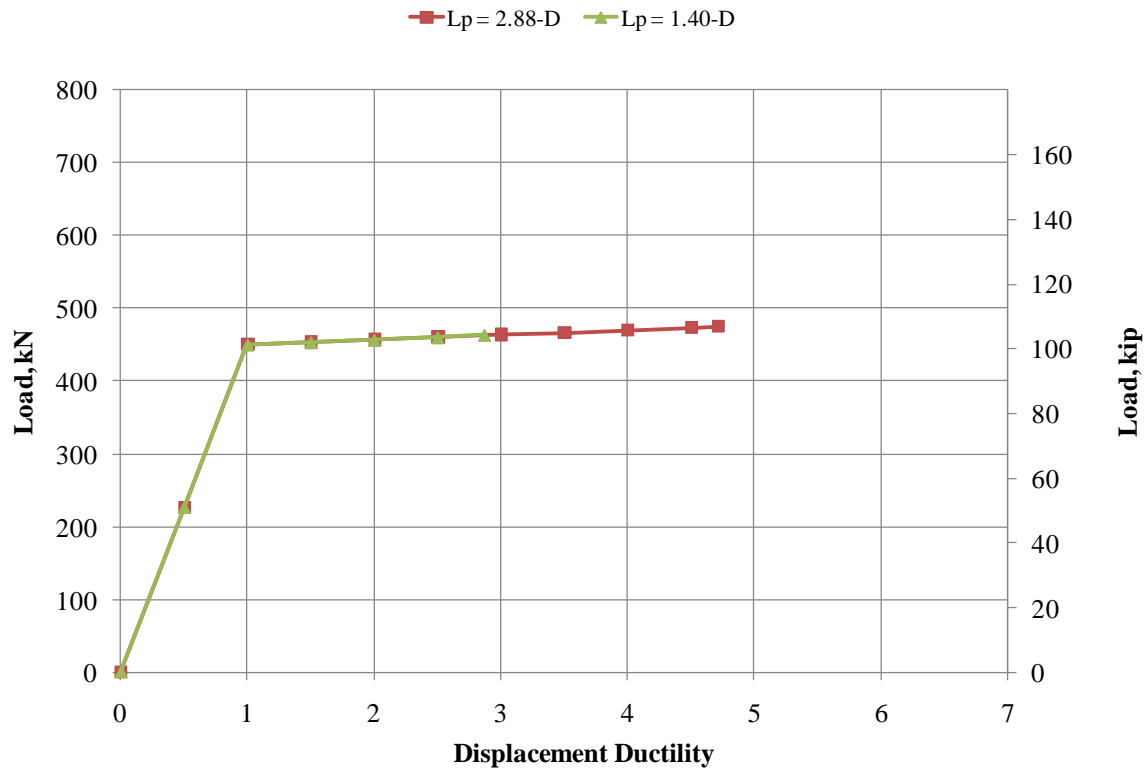


**Figure 4.5.3: Effect of Plastic Hinge Length, Soft Clay Foundation**

A comparison of the SAP2000 and finite element results is presented in Figure 4.5.4. If failure in the finite element model is defined using inelastic axial strain, or a uniaxial failure limit, the beam model provides a conservative approximation for the applied force-pile head displacement ductility response. In this case, the beam model under-predicts load capacity by about 30 percent with an accurate prediction for displacement ductility. However, if failure is defined using the multiaxial failure limit, or compressive damage, the beam model under-predicts both load capacity and displacement ductility by roughly 30 percent. Another key observation is that the initial stiffness of the beam model is also slightly less than that observed from the FE analysis, yet the effective yield point and post-yielding stiffness agree reasonably well. The variation in initial stiffness can be attributed to the fact that the input parameters for the FEA model are not the same

parameters required for the LPILE foundation analysis. That is to say, the finite element model requires a complex set of parameters that define the clay consolidation curve while LPILE requires the soil strength parameters.

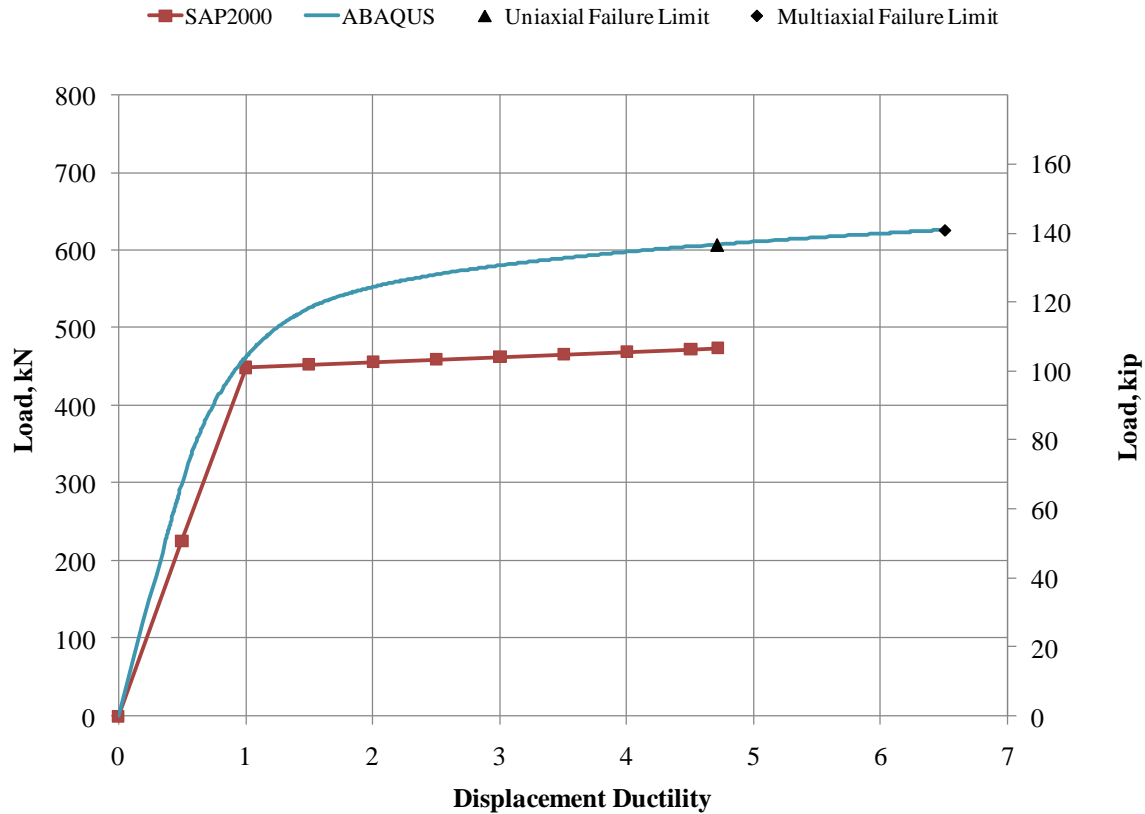


**Figure 4.5.4: Comparison of SAP2000 and ABAQUS Results, Soft Clay Foundation**

One might speculate that the finite element model achieves greater displacement ductility because the exterior surface of the pile is confined by soil. Therefore, if the soil confining pressure is over-approximated as being a uniformly applied pressure of 2.76 MPa (400 psi) (see Figure 4.4.12) and the XTRACT analysis is modified to include this effect, the result can be observed and is presented in Figure 4.5.5.

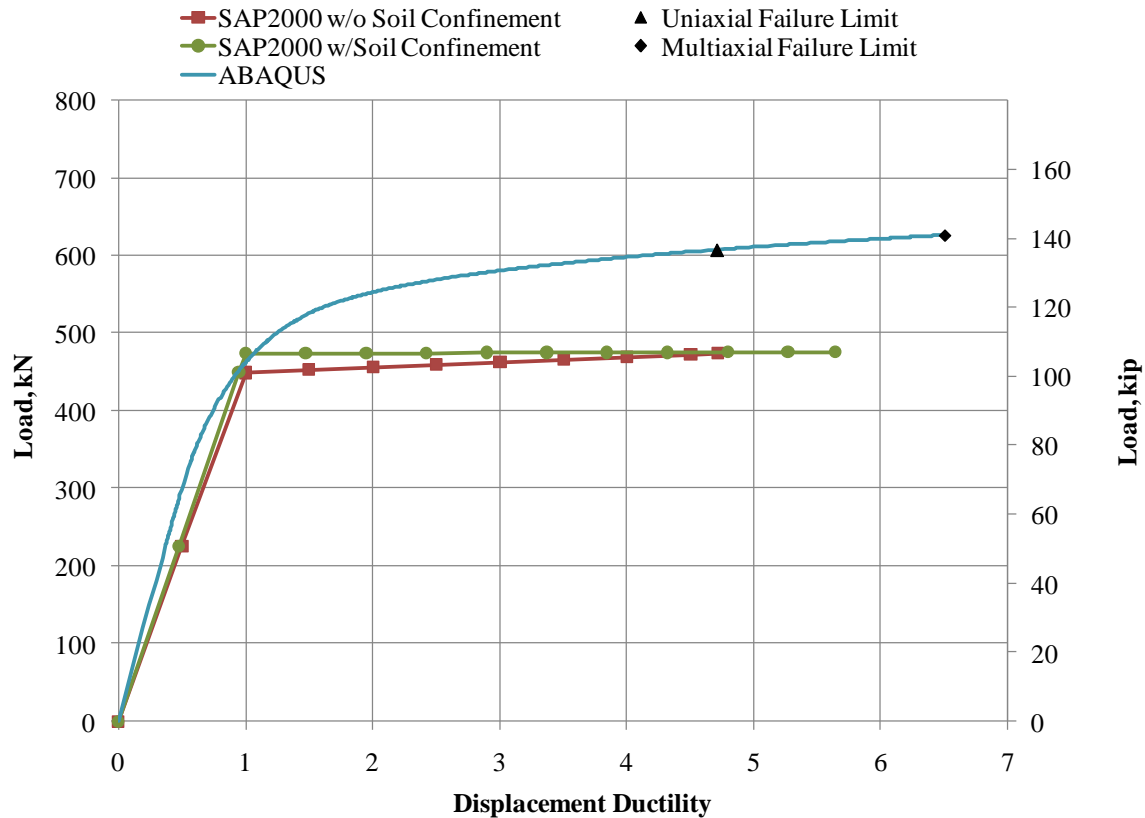


**Figure 4.5.5: Effect of Including Confining Pressure In SAP2000 Model**

The resulting analysis for including an over-approximation for confining pressure supplied by the soil clearly indicates that the maximum displacement ductility is improved, the response becomes elastic-perfectly-plastic, and the load capacity is unaffected. It should be noted, however, that Figure 4.4.12 clearly indicates that the soil confining pressure is a nonlinear distribution that rapidly decreases with depth, and soil confinement is not present on the tensile side of the pile due to gapping. Furthermore, since inelastic deformation in the beam model is specified in terms of an elasto-plastic response, it is evident that the moment-curvature response for the *in situ* piles is not as accurately predicted by XTRACT. This could be attributed to the fact that the simplified beam model only considers uniaxial stress-strain behavior whereas the finite element model includes multiaxial behavior. Overall, the simplified analytical method of

modeling the pile as a beam on a nonlinear elastic foundation provides a conservative estimate for the performance of the hollow core piles used in the foundation of the I-5 Ravenna Bridge.

#### **4.6 CONCLUSIONS**

In this chapter was presented the formulation of the analytical models used to investigate the performance of the *in situ* piles used in constructing the foundation of the I-5 Ravenna Bridge. The objectives of this portion of the research were: (1) develop a model using two soil types in order to understand the influence of confining pressure from the soil on the exterior surface of the pile, (2) determine whether or not confining pressure is great enough such that the cover concrete in the pile behaves as confined concrete, and (3) determine the location and length of the subgrade plastic hinge.

Section 4.2 provided an overview of the construction details for the *in situ* piles used in the Ravenna Bridge and discussed key modeling assumptions that were made. Section 4.3 presented the formulation of the XTRACT cross-section model based on the method discussed in Section 3.2, followed by the results from the analysis. Section 4.4 presented the 3D finite element model used to analyze the pile. The finite element model included the effects of soil confinement by incorporating either Boston Blue Clay or medium dense Ottawa Sand around the exterior of the pile. The clay was modeled using the modified cam clay plasticity model and the sand was modeled as a linear elastic material. The soil-pile interaction was modeled by defining normal and tangential contact interactions between the soil and pile surfaces. Section 4.5 detailed the formulation of the Winkler beam model used to investigate whether or not simplified analytical methods commonly used in design practice could reasonably approximate the response of the 3D

FEA model. The methods used to define the foundation stiffness and pile behavior under inelastic deformation were also discussed.

Based on the analytical results obtained using the method discussed in this chapter, the following conclusions are set forth:

- The response of the *in situ* pile is governed by the tensile capacity of the concrete. Once tensile cracks extended through the tension side of the pile a nearly linear response followed until compressive failure began at the opposite pile surface.
- Failure was observed when inelastic compressive strain and compression damage in the pile wall exceeded 0.00158 and 21 percent, respectively. The observed failure mechanism was compressive crushing and spalling of the concrete cover at an average below ground depth of 610 mm (24 in.). The prediction for displacement ductility when failure is defined in terms of inelastic axial strain (uniaxial failure limit) is roughly 70 percent of that predicted when failure is defined based on compression damage (multiaxial failure limit). Moreover, including multiaxial stress-strain behavior significantly improves the predicted displacement ductility.
- A plastic hinge measuring  $2.88-D$  in length formed 710 mm (28 in.) below ground for the pile embedded in Boston Blue Clay. Similarly, a plastic hinge measuring  $3.0-D$  in length formed 508 mm (20 in.) below ground for the pile embedded in Ottawa Sand. Hence, a stiffer soil causes the location of the plastic hinge to move toward the ground surface while softer soils will results in a greater depth to the center of the plastic hinge.

- The confining pressure supplied by the soil on the exterior surface of the pile is insufficient with regard to considering the concrete cover as confined concrete. The maximum confining pressure supplied by the soil occurs within the top 152 mm (6 in.) of soil and its magnitude rapidly decreases with depth.
- Confinement of the exterior surface of the pile may improve displacement ductility capacity since the spalled concrete cover is kept in place. However, the compressive zone would be further reduced to the extent that crushing of the concrete would progress through the pile wall until spalling of the inner core would occur. Therefore, one could expect that if the pile is retrofitted solely with a steel jacket a similar response would be observed and the performance of the pile would not appreciably improve.
- The Winkler beam model generated using XTRACT, LPILE, and SAP2000 Advanced Nonlinear provides a conservative elasto-plastic response to the 3D finite element model. When failure in the finite element model is defined based on the uniaxial state of strain, the simplified analysis under-predicted load capacity by roughly 30 percent. When failure in the finite element model is defined by the multiaxial state of strain, the simplified analysis under-predicted load and displacement ductility capacity by roughly 30 percent.
- When comparing the response of the Winkler beam model and the FE model with a multiaxial failure measure, it appears as though the beam model may provide a better prediction to the cyclic response of the pile. However, this should be further investigated.

- If the soil confining pressure is over-approximated as being a uniformly applied pressure over the plastic hinge region and is included in the Winkler beam model, the displacement ductility capacity is increased yet load capacity is unaffected. Results suggest that the simplified model is unable to predict the displacement ductility capacity provided by the 3D FEA model since the simplified model cannot account for multiaxial effects.



## CHAPTER FIVE

### 5. CONNECTION MODELING

#### 5.1 INTRODUCTION

The final research objective of this work was to develop a finite element model of the *in situ* pile-to-cross-beam connection to understand failure mechanisms and predict the moment-rotation response of the connection for use in future analyses. The connection model was analyzed for axial loads of 1183 kN (266 kips) and 592 kN (133 kips) in order to provide two sets of data for future analyses. To understand the moment transferring capability of the *in situ* connection, it was also analyzed as being fixed against rotation with an axial load of 1183 kN (266 kips). Cross-beam dimensions and connection reinforcement details were obtained from as-built drawings provided by the WSDOT, and are provided in Appendix A.2. It should be noted that the model presented in this chapter was generated using U.S. Customary units (lbs, in., s).

#### 5.2 CONNECTION DESCRIPTION

The cross-section of the cross beam measured 914 mm (36 in.) in height and 686 mm (27 in.) in width with an arbitrary length of 3760 mm (148 in.). The reinforced concrete plug, which connects the pile to the cross beam, measured 965 mm (38 in.) in diameter and 1270 mm (50 in.) in length. The plug was modeled as part of the cross beam in order to simulate a monolithic pour of concrete. A 2438 mm (96 in.) length of pile was modeled to the specifications detailed in Section 4.2. The length selected was such that it would simulate the approximate length of pile between the cross beam and above ground

inflection point. An overview of the model is provided in Figure 5.2.1, and note that it utilized a y-z plane of symmetry.

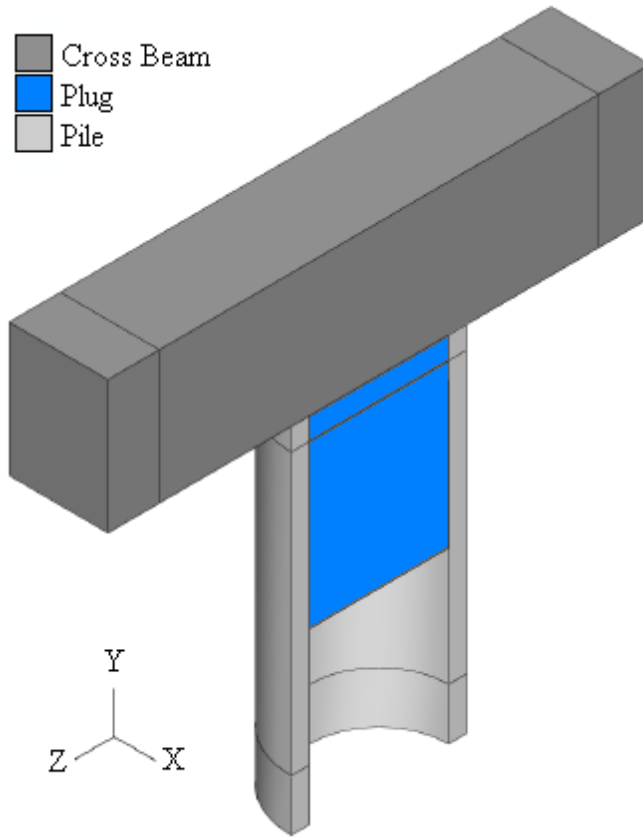


**Figure 5.2.1: Connection Model Overview**

An overview of the reinforcement layout for the cross beam and plug are provided in Figure 5.2.2. Longitudinal reinforcement in the cross beam was supplied in the form two No. 6 bars, five No. 10 bars, one No. 11 bar, and four No. 14 bars. Longitudinal bar spacing and coverage details are provided in Appendix A.2. Thirteen of each, No. 5 rectangular hoops, No. 5 stirrups, and No. 4 stirrups, were provided for shear reinforcement with 12 in. spacing between instances.

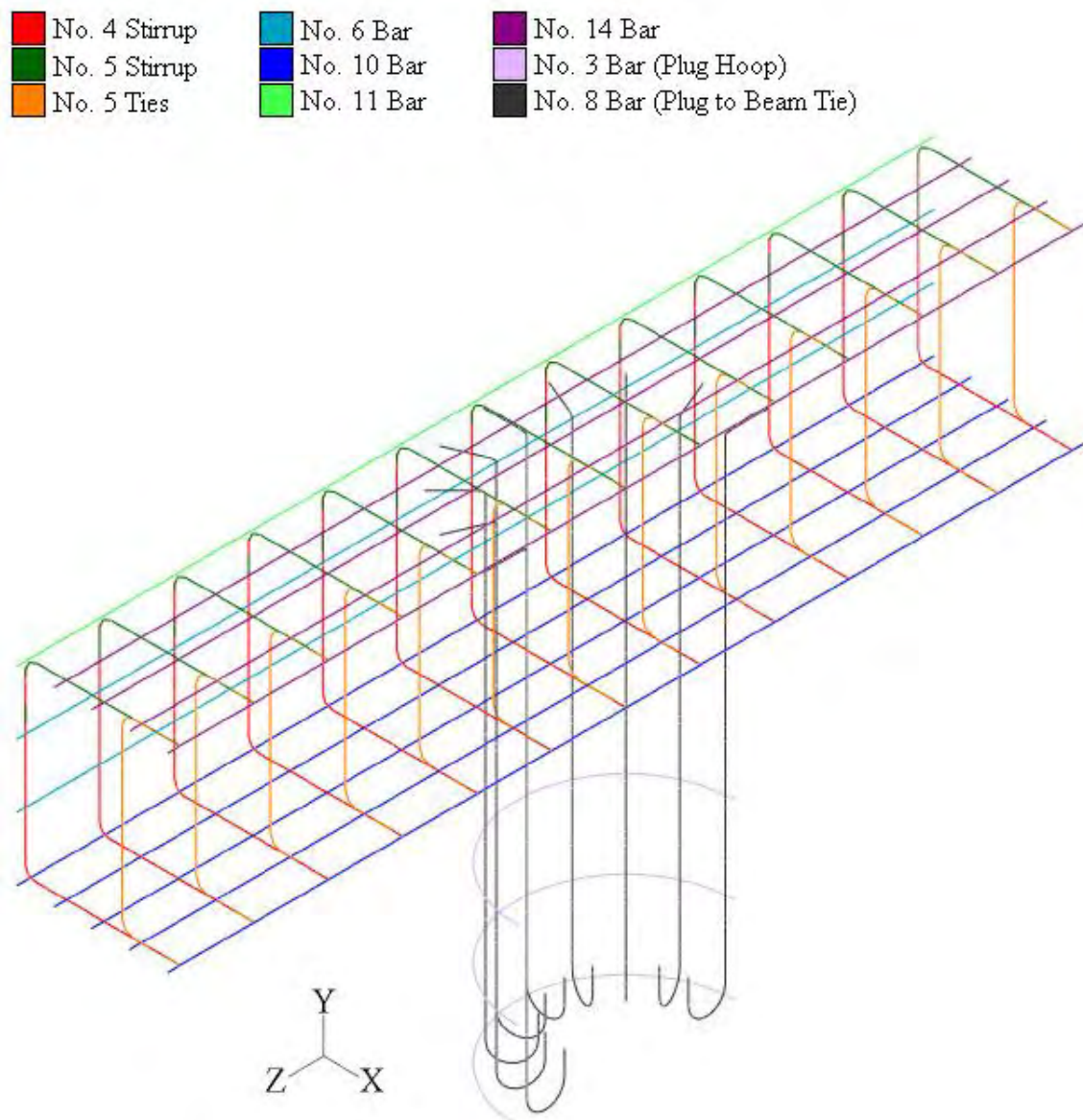


**Figure 5.2.2: Cross Beam and Plug Rebar Layout**

The concrete plug was connected to the cross beam via nine hooked No. 8 bar ties. Transverse reinforcement was supplied in the form of three No. 3 bar circular hoops with a diameter of 546 mm (21.5 in.). Based on Mander's model (1988) for confined concrete, it was determined that the plug concrete was unconfined. The constitutive models for the reinforcing steel, prestressing steel, and concrete used in the connection model were those

defined in Section 4.4.2. An overview of the assembled connection model is presented in Figure 5.2.3.

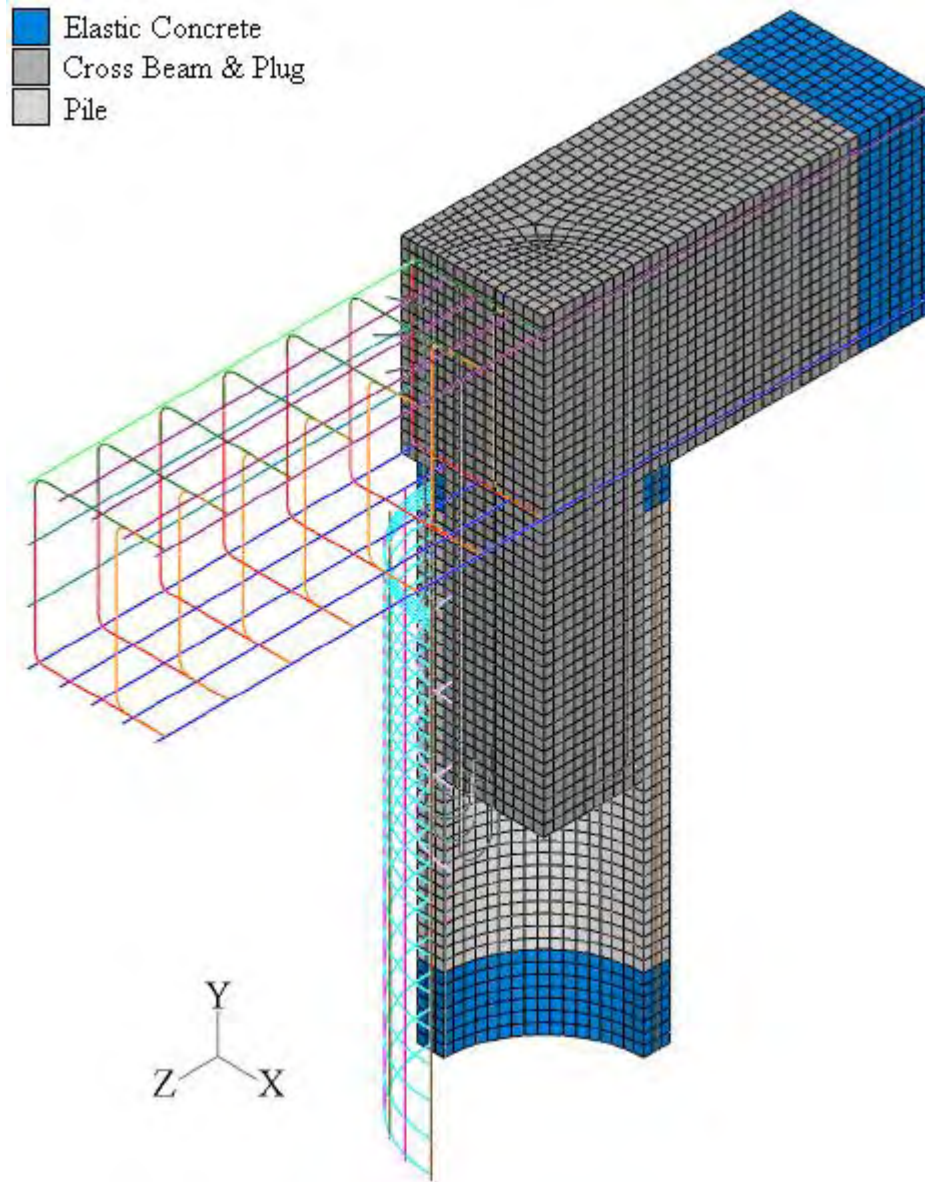


**Figure 5.2.3: Connection Model Assembly**

Finite elements for the pile, cross beam, and plug consisted of standard eight-node linear hexahedral 3D continuum elements with reduced integration. The cross beam and plug were meshed such that the approximate global size of the elements measured 51 mm (2 in.). The pile was meshed such that the approximate global size of the elements

measured 42 mm (1.66 in.) in order to have three elements through the wall thickness. To eliminate unnecessary material nonlinearity at points of support and applied loads, each end of the pile and cross beam was modeled as linearly elastic, with elastic properties equivalent to those listed in Table 4.4.3.

The reinforcing bars and prestressing tendons were meshed using standard two node 3D truss elements with an approximate element length of 100 mm (4 in.). The cross-sectional area of the reinforcing bars and seven wire prestressing strands were specified based on the tabulated values in Appendix E of ACI 318-05 (2005). Note that prestressing strands and reinforcing bars which lay on the plane of symmetry were specified to have one half of the ACI tabulated cross-sectional area.

### **5.3 BOUNDARY & INITIAL CONDITIONS**

The boundary conditions were imposed to minimize shear and flexural deformation of the cross beam. In addition, the desired moment-rotation response included connection rotation due to the P- $\Delta$  effect, pile shear deformation, and rigid body rotation. Therefore, the  $U_x$ ,  $U_y$  and  $U_z$  degrees of freedom (DOF) were constrained for all of the nodes on the top and ends of the cross beam to minimize shear and bending deformation. To facilitate symmetry, the  $U_x$  DOF was constrained for all of the nodes on the plane of symmetry. An overview of the boundary conditions is presented in Figure 5.3.1. To facilitate the application of the 270 kN (61 kips) prestressing force, a stress-type initial condition was utilized to apply an initial stress to the tendons at a magnitude of 1210 MPa (175.3 ksi) in the y-direction.

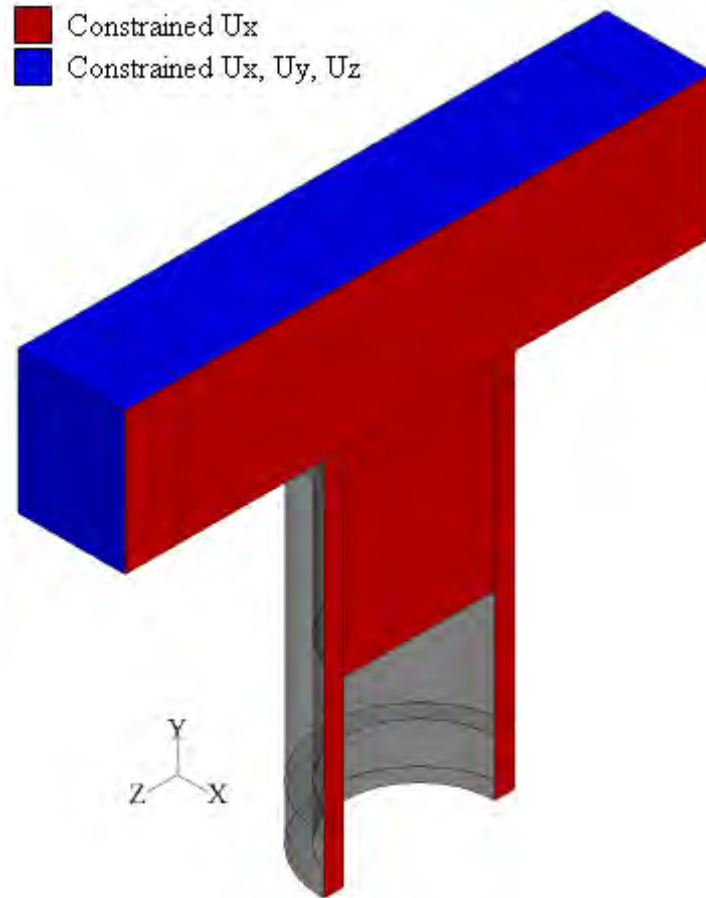


**Figure 5.3.1: Connection Model Boundary Conditions**

## 5.4 LOADING

Loading was applied using two steps: axial load was applied in the first step and lateral loading in the second. The loading increment was held constant through all steps of the analysis and the minimum time increment was specified as  $1e-5$ . The axial load step was used to apply the 1183 kN (266 kips) or 592 kN (133 kips) axial load at the free end of the pile as a uniformly distributed non-following surface traction in the positive  $y$ -direction. A non-following surface traction was utilized in order to include the  $P-\Delta$  effect. The lateral push step was used to apply a lateral load of 667 kN (150 kips) at the free end of the pile as a uniformly distributed surface traction in the negative  $z$ -direction.

Nonlinear geometry due to large deformations and deflections was included in all three steps of the analysis. Discontinuous analysis control was not used during the analysis because preliminary analyses deemed it unnecessary. Note that gravity loads could not be considered in the connection model due to imposed boundary conditions. However, gravity loads were considered to have little effect.

## **5.5 CONTACT INTERACTIONS**

Two interactions were required to define the necessary contact behavior between the cross beam and the pile. The first defined the contact interaction for the end of the pile in contact with the bottom of the cross beam. The second interaction defined the contact interaction between the interior surface of the pile and the exterior surface of the concrete plug. Note that the as-built construction details specified that the inner surface of the pile was roughened to bond the plug concrete to the pile. An overview of the contact surface pairs used to define the contact interactions is provided in Figure 5.5.1. The interactions were simulated using surface-to-surface based contact definitions. The definitions utilized surface-to-surface discretization with finite sliding, and contact constraints were imposed on nodes of the contact surfaces with no adjustment to slave or surface nodes. To model the connection as being fixed against rotation, the pile-plug contact interaction was replaced using a surface-to-surface tie constraint with default position tolerances and slave surface adjustments.

Both interactions were defined using an isotropic penalty friction formulation for tangential behavior and Augmented Lagrange normal contact behavior. The surface normal contact allowed for separation after contact and was defined using the default contact stiffnesses. The tangential friction interaction was slip-rate and contact-pressure

independent with a coefficient of friction of 0.66. It should be noted that no maximum shear stress was specified for either interaction property and that all other interaction options not discussed herein were taken as the default values within ABAQUS.

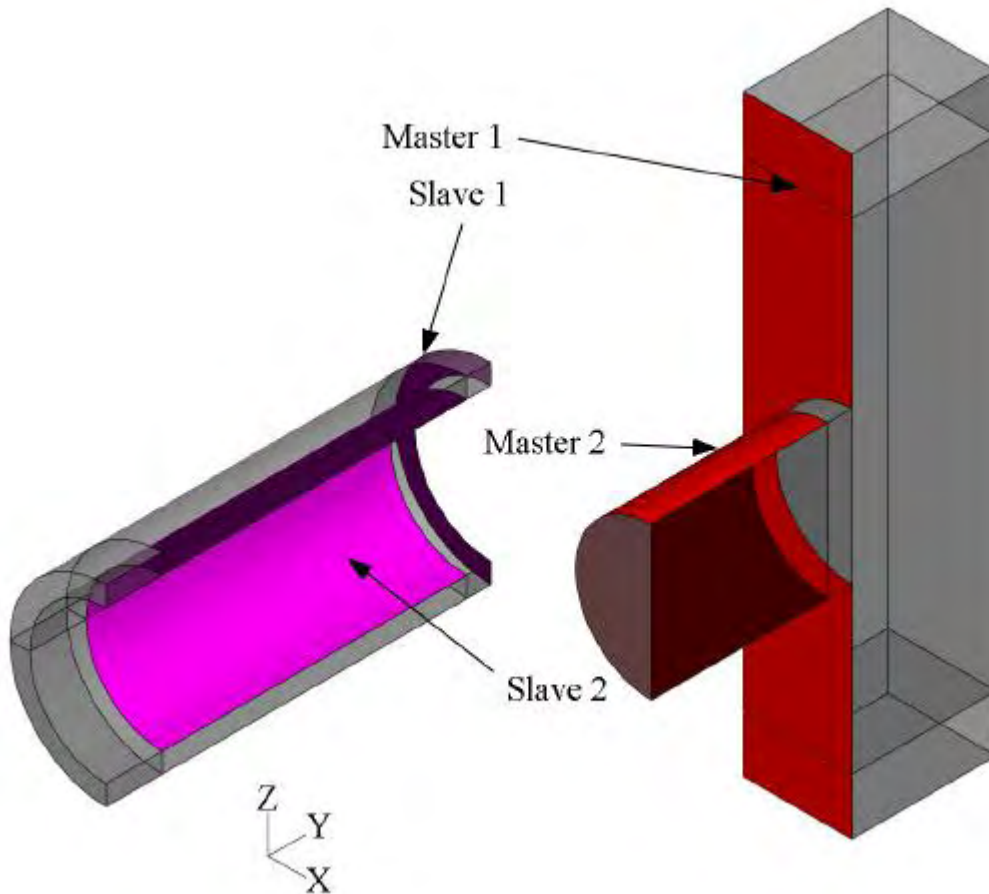


**Figure 5.5.1: Connection Model Contact Surface Definitions**

## **5.6 CONNECTION MODEL RESULTS**

The results presented in this section correspond to the connection model with an applied axial load of 1183 kN (266 kips) since it best represents the *in situ* connections. The performance of the connection model was governed by the tensile capacity of the concrete. Tensile cracks initiated at the reentrant corner where the concrete plug is fused



to the cross beam at a lateral load of approximately 220 kN (50 kips). Failure was characterized by the distribution of tensile damage in the concrete. By setting the upper limit of tensile damage to 50 percent, which corresponds to a complete loss of concrete tensile strength, and viewing the final state of the analysis, the tensile damage distribution in the connection can be observed as shown in Figure 5.6.1.

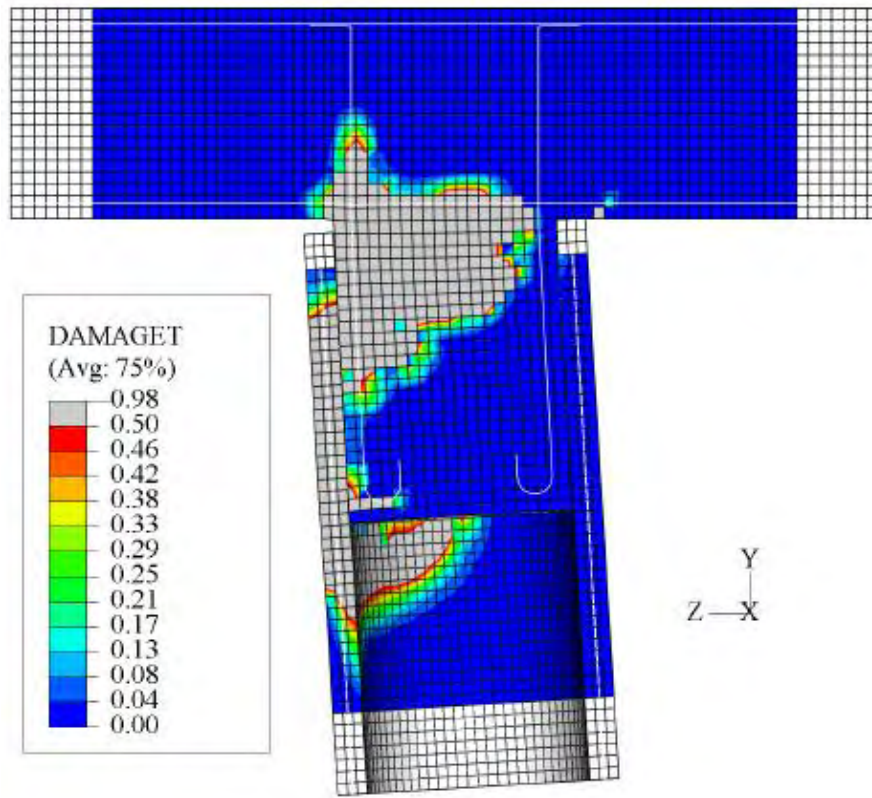


**Figure 5.6.1: Overview of Tensile Damage,  $d_t$ , Distribution in Connection**

By inspection of Figure 5.6.1, it is evident that tensile cracks propagate through roughly 90 percent of the plug diameter and extensive flexural cracking occurs in the pile wall. Similarly, Figure 5.6.2 illustrates that extensive tensile damage occurs throughout the entire concrete plug to the extent that all tensile forces are resisted by the hooked longitudinal ties connecting the plug to the cross beam.

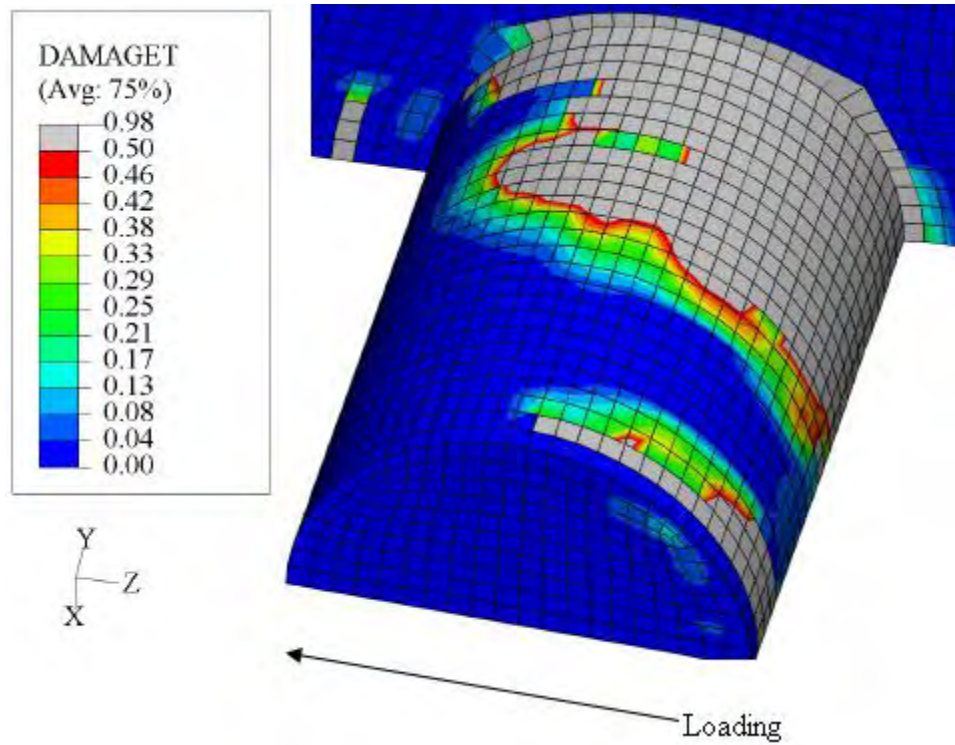


**Figure 5.6.2: Distribution of Tensile Damage,  $d_t$ , in the Concrete Plug**

Therefore, the distribution of maximum principal inelastic strain in the ties was plotted as shown in Figure 5.6.3 in order to observe whether or not any of the ties failed due to tensile rupture. By setting the upper limit and lower limits of the contour plot as the ultimate and yield strain, respectively, one can see that the majority of the ties have experienced significant yielding, yet none have ruptured.

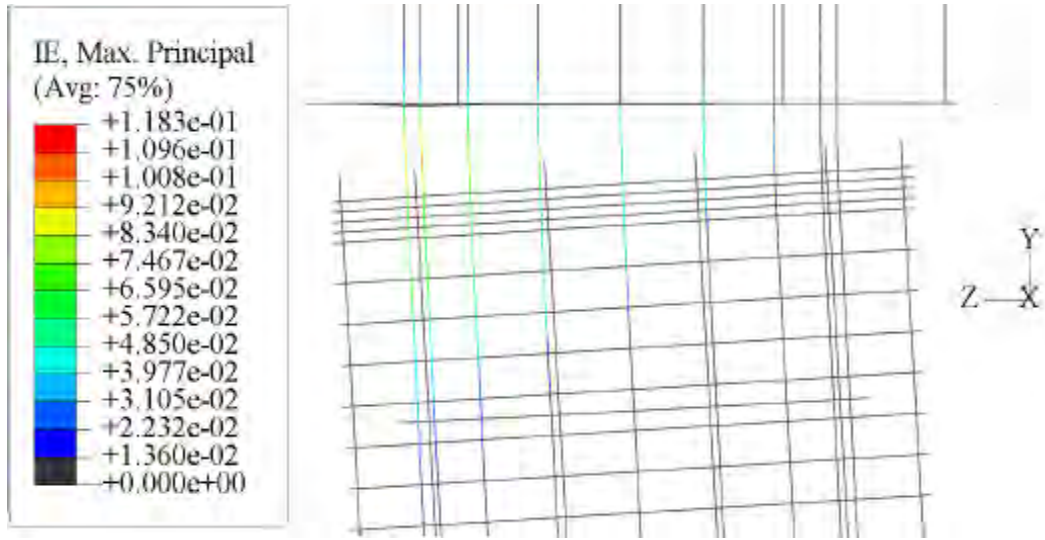


**Figure 5.6.3: Max Principal Strain Distribution in Cross Beam-Plug Ties**

Please refer to Figure 5.6.4 for the following discussion. The y-component of displacement for nodes  $U1$  and  $U2$  was used to calculate the rotation ( $\theta$ ) of the pile by Equation 5-1.

$$\theta = \tan^{-1} \left( \frac{|U1_y - U2_y|}{d_o} \right) \quad (5-1)$$

where:

$U1_y$  = y-component of displacement at Node  $U1$

$U2_y$  = y-component of displacement at Node  $U2$

$d_o$  = Outer diameter of pile

The  $z$ -component of displacement for node  $U3$  was used to calculate the contribution of moment due to the  $P$ - $\Delta$  ( $M_{P-\Delta}$ ) effect by Equation 5-2.

$$M_{P-\Delta} = |P_y \cdot U3_z| \quad (5-2)$$

where:

$P_y$  = Axial load

$U3_z$  =  $z$ -component of displacement at Node  $U3$

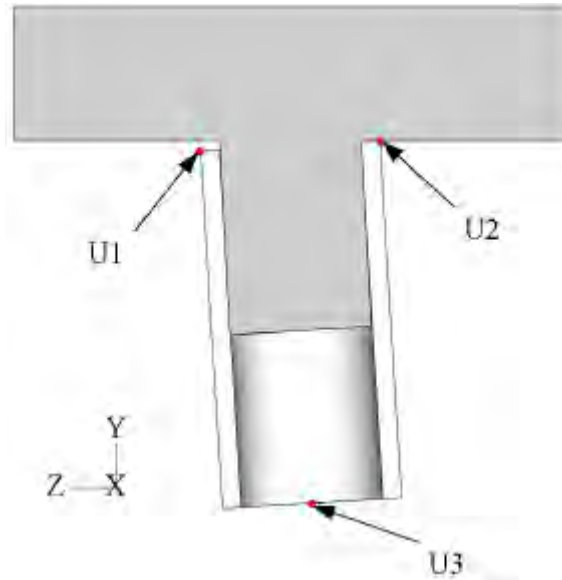


**Figure 5.6.4: Nodes Used for Calculations**

A comparison of the moment-rotation response for all three connection models is presented in Figure 5.6.5. It is interesting that the moment-rotation response is essentially elasto-plastic where little rotation of the connection is experienced during the elastic response. One can observe that varying the applied axial load does not adversely affect the rotation capacity of the connection model. However, a 50 percent reduction in the applied axial load decreases the yield moment and post-yield moment capacity by roughly 10 percent. It is also important to note that the moment capacity of the *in situ* connection model, having an applied axial load of 1183 kN (266 kips), is equivalent to

that of the fixed connection. By modeling the connection as fixed, the ultimate moment capacity is reached while allowing for significantly less rotation. Hence, the rotation capacity of the *in situ* connection is roughly 2.5 times that of the fixed connection. Overall, Figure 5.6.5 provides information pertaining to the rotational stiffness that should be used for the pile-to-cross beam connections when performing nonlinear pushover or nonlinear dynamic analysis of the I-5 Ravenna Bridge.

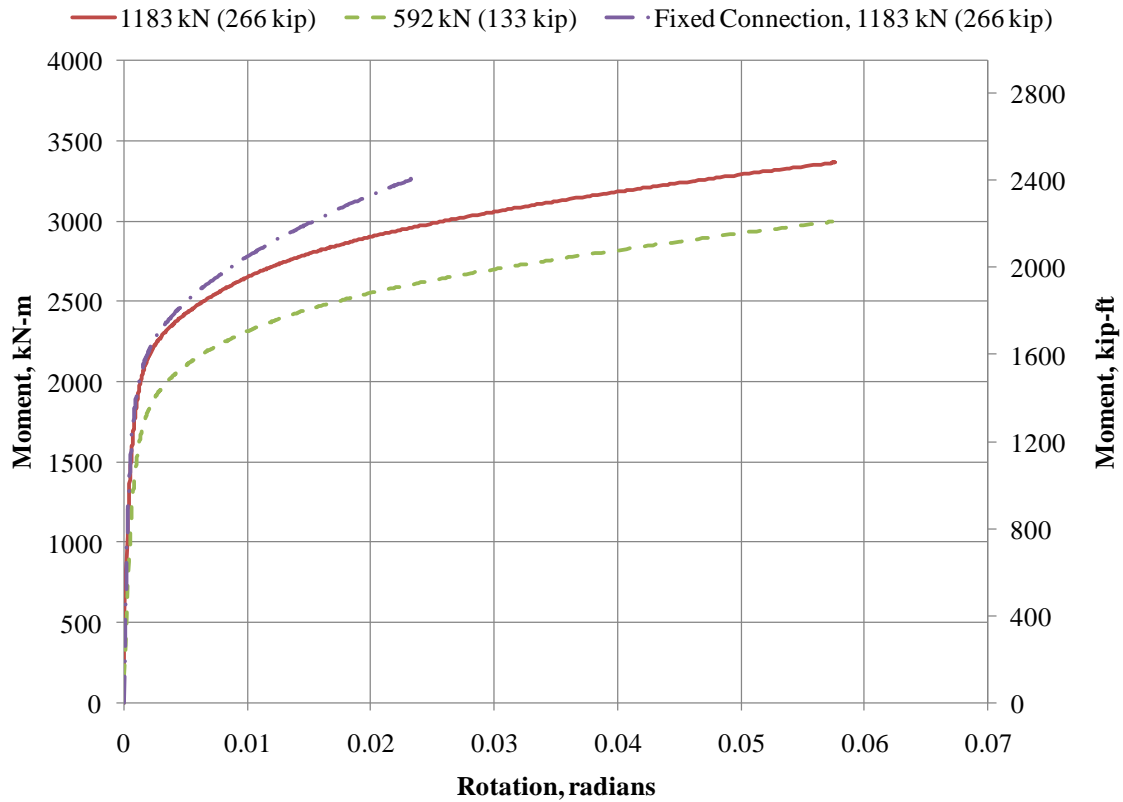


**Figure 5.6.5: Moment-Rotation Response Comparison**

## 5.7 CONCLUSIONS

In this chapter, formulation of the analytical models used to investigate the performance of the *in situ* pile-to-cross-beam connections in the I-5 Ravenna Bridge was presented. The objectives of this portion of the research were: (1) develop a model of the

*in situ* pile-to-cross-beam connection to understand the failure mechanisms, and (2) determine the moment-rotation response of the connection for use in future analyses.

Section 5.2 presented an overview of the connection geometry, including reinforcement details and the construction method used to connect the cross beam to the hollow core piles. Sections 5.3 through 5.5 presented the boundary conditions, initial conditions, loads, and contact interactions necessary to accurately model the connection. Section 5.6 presented the definition of failure, observed failure mechanism, and moment-rotation response of the connection.

Based on the analytical results obtained using the method discussed in this chapter, the following conclusions are set forth:

- The response of the *in situ* connection is governed by the tensile capacity of the concrete. Tensile cracking is initiated in the *in situ model* at the reentrant corner where the concrete plug is connected to the cross beam. At this juncture, tensile cracks continue to rapidly propagate through roughly 90 percent of the plug diameter until failure of the connection occurs in the plug.
- The majority of the reinforcing steel used to tie the concrete plug to the cross beam experienced significant inelastic deformation due to large tensile forces, yet none of the ties fail in tension or compression.
- The moment-rotation response of the connection is essentially elasto-plastic where little rotation of the connection is experienced during the elastic response.
- The rotation capacity of the connection is virtually unaffected by the applied axial load. However, when the applied axial load was reduced by 50 percent, the

yield moment and post-yield moment capacity are reduced by approximately 10 percent.

- Modeling the connection as fixed reduces the rotation capacity by nearly 60 percent while the moment capacity is virtually unaffected. This suggests that a fixed connection develops its full moment resisting capacity much more rapidly and allows for significantly less rotation than a partially fixed connection. This observation agrees well with fundamental structural mechanics.
- It is recommended that the rotational response of the connections in the I-5 Ravenna Bridge be taken as the equivalent energy elastic-plastic response of the moment-rotation relationship obtained from the finite element model.

## CHAPTER SIX

### 6. CONCLUSIONS

#### 6.1 SUMMARY

Numerical models were developed to investigate the response of the *in situ* piles and pile-to-cross-beam connections used in constructing the I-5 Ravenna Bridge. The *in situ* piles were investigated through multiple nonlinear static analyses using ABAQUS/Standard, XTRACT, SAP2000 Advanced Nonlinear, and LPILE. Behavior of the connection was investigated using a finite element model developed using ABAQUS/Standard.

The models developed to investigate the *in situ* piles were verified against existing experimental data presented by Budek, et al. (1997b). During development of the finite element model, it was found that careful consideration must be taken when defining the compression hardening, tension stiffening, and damage variables for the concrete damaged plasticity model. As a result, a method based on fracture mechanics and reinforced concrete design was developed to consistently define constitutive model parameters.

In order to compare XTRACT and ABAQUS results, the moment curvature relationships developed in XTRACT were implemented in a simple beam model in SAP2000 Advanced Nonlinear. The behavior of the beam elements were defined in terms of the effective moment-curvature response of the pile, with a yield surface defined as the axial load-effective moment interaction diagram. It was also noted that since the



axial load did not vary during the beam model analyses, post-yielding behavior can be defined in terms of the effective moment-curvature response. This chapter presents the major findings from this study and recommendations for future research. Based on the analytical results obtained from this work, a number of conclusions were obtained and are categorized by chapter.

## **6.2 CONCLUSIONS: CHAPTER THREE**

Cross sectional analysis appears to be adequate for predicting moment capacity but it does not reflect the damage and loss of stiffness from cyclic loading of the concrete without longitudinal reinforcement.

ABAQUS provides more accurate results for ductility than those of XTRACT. This could be attributed to the fact that ABAQUS includes the effect of multiaxial stress from hoop reinforcement in the concrete failure response, while XTRACT only considers uniaxial behavior.

The finite element analyses, cross-section analyses, and experimental work (Budek, et al., 1997b) have shown that failure occurs once concrete in the compression zone spalls, exposing the reinforcing steel and prestressing tendons, allowing them to buckle.

The proposed 3D finite element model is capable of capturing the behavior of prestressed hollow core concrete piles. Load capacity and displacement ductilities at yield and failure for both pile specimens appear to be well-predicted by the ABAQUS model, with an overprediction in strength of roughly 20 percent. This overestimation could be

attributed to the fact that the analytical model was loaded monotonically while the experimentally tested piles were subjected to cyclic loading, as indicated by Tuladhar, et al. (2007).

Excessive values for fracture energy can lead to convergence issues; therefore, a systematic approach to calculate the fracture energy is set forth. The proposed methodology utilizes concrete cylinder splitting strength to define tensile strength of the concrete and concrete cover thickness to define the crack depth.

The sensitivity analysis has shown that the concrete tensile strength, fracture energy, and prestressing force are the most influential parameters on the performance of the pile model. Transverse reinforcement ratio has negligible effect on load capacity and displacement ductility which agrees with experimental observations (Budek, et al., 1997b). This is attributed to the fact that, due to the hollow core, confining steel does not improve concrete compressive strength or ultimate strain.

Based on results from the sensitivity analysis, it is evident that the values used to define the concrete constitutive model have resulted in the most accurate predictions for displacement ductility and lateral load capacity. Overall, the systematic approach used in defining constitutive parameters provides accurate predictions for strength, ductility, and mode of failure.

The series of simplified analyses discussed in this section were found to provide reasonable approximations to both the complex finite element analyses and experimental results. Although the plastic hinge length does not adversely affect load capacity predictions, careful consideration must be taken when specifying the plastic hinge length for SAP2000 analyses since inaccurate values can lead to drastic over or underestimation of displacement ductility.

XTRACT cross section analyses combined with SAP2000 nonlinear pushover analyses provide conservative approximations for pile performance when the plastic hinge length is defined per Caltrans Seismic Design Criteria (2006). In these analyses, displacement ductility capacity was under-estimated by an average of 35 percent when using this simplified approach based on current design practice.

### **6.3 CONCLUSIONS: CHAPTER FOUR**

The response of the *in situ* pile is governed by the tensile capacity of the concrete. Once tensile cracks extended through the tension side of the pile a nearly linear response followed until compressive failure began at the opposite pile surface.

Failure was observed when inelastic compressive strain and compression damage in the pile wall exceeded 0.00158 and 21 percent, respectively. The observed failure mechanism was compressive crushing and spalling of the concrete cover at an average below ground depth of 610 mm (24 in.). The prediction for displacement ductility when failure is defined in terms of inelastic axial strain (uniaxial failure limit) is roughly 70

percent of that predicted when failure is defined based on compression damage (multiaxial failure limit). Moreover, including multiaxial stress-strain behavior significantly improves the predicted displacement ductility.

A plastic hinge measuring  $2.88-D$  in length formed 710 mm (28 in.) below ground for the pile embedded in Boston Blue Clay. Similarly, a plastic hinge length measuring  $3.0-D$  in length formed 508 mm (20 in.) below ground for the pile embedded in Ottawa Sand. Hence, a stiffer soil causes the location of the plastic hinge to move toward the ground surface while softer soils will results in a greater depth to the center of the plastic hinge.

The confining pressure supplied by the soil on the exterior surface of the pile is insufficient with regard to considering the concrete cover as confined concrete. The maximum confining pressure supplied by the soil occurs within the top 152 mm (6 in.) of soil and its magnitude rapidly decreases with depth.

Confinement of the exterior surface of the pile may improve displacement ductility capacity since the spalled concrete cover is kept in place. However, the compressive zone would be reduced to the extent that crushing of the concrete would progress through the pile wall until spalling of the inner core would occur. Therefore, one could expect that if the pile is retrofitted solely with a steel jacket a similar response would be observed and the performance of the pile would not appreciably improve.

The Winkler beam model generated using XTRACT, LPILE, and SAP2000 Advanced Nonlinear provides a conservative elasto-plastic response to the 3D finite element model. When failure in the finite element model is defined based on the uniaxial state of strain, the simplified analysis under-predicted load capacity by roughly 30 percent. If failure in the finite element model is defined on the multiaxial state of strain, the simplified analysis under-predicted load and displacement ductility capacity by roughly 30 percent.

If the soil confining pressure is over-approximated as being a uniformly applied pressure over the plastic hinge region and is included in the Winkler beam model, the displacement ductility capacity is increased yet load capacity is unaffected. Results suggest that the simplified model is unable to predict the displacement ductility capacity provided by the 3D FEA model since the simplified model cannot account for multiaxial effects.

#### **6.4 CONCLUSIONS: CHAPTER FIVE**

The response of the *in situ* connection is governed by the tensile capacity of the concrete. Tensile cracking is initiated in the *in situ model* at the reentrant corner where the concrete plug is connected to the cross beam. At this juncture, tensile cracks continue to rapidly propagate through roughly 90 percent of the plug diameter until failure of the connection occurs in the plug.

The majority of the reinforcing steel used to tie the concrete plug to the cross beam experience significant inelastic deformation due to large tensile forces, yet none of the ties fail in tension or compression.

The moment-rotation response of the connection is essentially elasto-plastic where little rotation of the connection is experienced during the elastic response. The rotation capacity of the connection is virtually unaffected by the applied axial load. However, when the applied axial load was reduced by 50 percent, the yield moment and post-yield moment capacity are reduced by approximately 10 percent.

Modeling the connection as fixed reduces the rotation capacity by nearly 60 percent while the moment capacity is virtually unaffected. This suggests that a fixed connection develops its full moment resisting capacity much more rapidly and allows for significantly less rotation than a partially fixed connection. This observation agrees well with fundamental structural mechanics.

It is recommended that the rotational response of the connections in the I-5 Ravenna Bridge be taken as the equivalent energy elastic-plastic response of the moment-rotation response obtained from the finite element model.

## **6.5 RECOMMENDATIONS FOR FUTURE RESEARCH**

There are numerous available avenues to investigate with regard to the performance of hollow core piles embedded in soil. One particularly interesting study that could be performed is to investigate how pile diameter, wall thickness, above ground height, and

axial load affect the location and length of the plastic hinge for a hollow pile embedded in uniform sand and clay. It would be interesting to see if strong correlations exist between the aforesaid parameters and the friction angle of sand or undrained shear strength of clay.

One crucial study would be to investigate viable retrofit methods for hollow core piles of the configuration described in this work. One suggested retrofit method is to pump grout, potentially non-shrink or expansive, into the hollow void of the pile and jacket the exterior with steel or fiber reinforced polymer based materials. However, an issue of concern would be the variation in stiffness between the retrofitted above ground height and subgrade length containing the soil plug.

## REFERENCES

- ABAQUS Software and Documentation, Version 6.7-1. © Dassault Systèmes, SIMULIA, 2007.
- American Concrete Institute Committee 318, *Building Code Requirements for Structural Concrete (ACI318-05) and Commentary (ACI318R-05)*. American Concrete Institute, Farmington Hills, MI. August 2005.
- Appa Rao, G., and Raghu Prasad, B.K., Fracture Energy and Softening Behavior of High Strength Concrete, *Cement and Concrete Research*, Vol. 32, 2002, pp.247-252.
- Bae, S., and Bayrak, O., Stress Block Parameters for High-Strength Concrete Members, *ACI Structural Journal*, Vol. 100, No. 5, September-October 2003, pp. 626-636.
- Bažant, Z.P., Size Effect in Blunt Fracture: Concrete, Rock, Metal, *Journal of Engineering Mechanics*, Vol. 110, No. 4, April 1984, pp. 518-535.
- Budek, A.M., Benzoni, G., and Priestley, M.J.N, Analytical Studies on the Inelastic Seismic Response of Solid and Hollow Precast Prestressed Piles, Division of Structural Engineering, University of California at San Diego, La Jolla, California, Report No. SSRP 97/16, November 1997(c)
- Budek, A.M., Benzoni, G., and Priestley, M.J.N, The Effect of External Confinement and Transverse Reinforcement on Plastic Hinges in Cast-in-Place Pile Shafts, Division of Structural Engineering, University of California at San Diego, La Jolla, California, Report No. SSRP 97/04, June 1997(a)
- Budek, A.M., Benzoni, G., and Priestley, M.J.N, Experimental Investigation of Ductility of In Ground Hinges in Solid and Hollow Prestressed Piles, Division of Structural Engineering, University of California at San Diego, La Jolla, California, Report No. SSRP 97/17, November 1997(b)
- Budek, A.M., and Priestley, M.J.N., Experimental Analysis of Flexural Hinging in Hollow Marine Prestressed Pile Shafts, *Coastal Engineering Journal*, Vol. 47, No. 1, 2005, pp. 1-20.
- Budek, A.M., Priestley, M.J.N., Benzoni, G., Inelastic Seismic Response of Bridge Drilled-Shaft RC Pile/Columns, *Journal of Structural Engineering*, Vol. 126, No. 4, April 2000, pp. 510-517.
- Boresi, A.P., Schmidt, R.J., Sidebottom, O.M., Table 15.2, Case 4. Single-Edge Crack in Finite Width Sheet, *Advanced Mechanics of Materials*, 5<sup>th</sup> Edition, John Wiley & Sons, © 1993, pp. 614-615.



- Caltrans Seismic Design Criteria (CSDC) Version 1.4*, California Department of Transportation, Section 7, June 2006.
- Chai, Y.H., Flexural Strength and Ductility of Extended Pile-Shafts. I: Analytical Model, *Journal of Structural Engineering*, Vol. 128, Iss. 5, May 2002, pp. 586-594.
- Chai, Y.H., Hutchinson, T.C., Flexural Strength and Ductility of Extended Pile-Shafts. II: Experimental Study, *Journal of Structural Engineering*, Vol. 128, Iss. 5, May 2002, pp. 595-602.
- Chen, W., *Plasticity in Reinforced Concrete*, 1<sup>st</sup> Edition. J. Ross Publishing, Fort Lauderdale, FL, © 2007.
- Collins, M.P., and Mitchell, D., *Prestressed Concrete Structures*. Prentice Hall, Englewood Cliffs, NJ, © 1991, pp. 81-87.
- Das, B.M., *Principles of Foundation Engineering*, 5<sup>th</sup> Edition. Brooks/Cole – Thomas Learning, Pacific Grove, CA, © 2004.
- Darwin, D., Barham, S., Kozul, R., and Luan, S., Fracture Energy of High-Strength Concrete, *ACI Materials Journal*, Vol. 98, No. 5, September-October 2001, pp. 410-417
- Ensfield, R.A., and Velasco, M.S.L., Fracture Parameters for High-Performance Concrete, *Cement and Concrete Research*, Vol. 36, 2006, pp. 576-583.
- Falconer, T.J., and Park, R., Ductility of Prestressed Concrete Piles Under Seismic Loading, Research Report No. 82-6, Department of Civil Engineering, University of Canterbury, New Zealand, February 1982.
- FHWA Seismic Retrofitting Manual for Highway Structures: Part 1 – Bridges*, U.S. Department of Transportation, Federal Highway Administration, Section 7.5, January 2006, pp. 233-234
- Gettu, R., Bažant, Z.P., and Karr, M.E., Fracture Properties and Brittleness of High Strength Concrete, *ACI Materials Journal*, Vol. 87, No. 6, November-December 1990, pp. 608-618
- Google Earth, Version 4.3 (beta). Accessed August, 25, 2008. Google, Inc., July 8, 2008.
- Hillerborg, A., Modeer, M., Petersson, P.E., Analysis of Crack Formation and Crack Growth in Concrete by Means of Fracture Mechanics and Finite Elements, *Cement and Concrete Research*, Vol. 6, pp. 773–782, 1976.

Holtz, R.D., Kovacs, W.D., *An Introduction to Geotechnical Engineering*, Prentice Hall, New Jersey, © 1981.

Ikeda, S., Tsubaki, T., and Yamaguchi, T., Ductility Improvement of Prestressed Concrete Piles, *Transactions of the Japan Concrete Institute*, Vol. 113, No. 2, 1982, pp. 531-538.

Iravani, S., Mechanical Properties of High-Performance Concrete, *ACI Materials Journal*, Vol. 93, No. 5, September-October 1996, pp. 416-426.

Kapur, J. Washington State's Bridge Seismic Retrofit Program. *Technical Memorandum of Public Works Research Institute*. Vol. 4009, 2006, pp. 519-531.

Lee, J., and Fenves, G.L., Plastic-Damage Model for Cyclic Loading of Concrete Structures, *Journal of Engineering Mechanics*, Vol. 124, No. 8, 1998, pp. 892-900.

Ling, H.I., Yue, D., Kaliakin, V.N., Themelis, N.J., Anisotropic Elastoplastic Bounding Surface Model for Cohesive Soils, *Journal of Engineering Mechanics*, Vol. 128, No. 7, July 2007, pp. 748-758.

LPILE Plus Software and Documentation, Version 5.0. Ensoft, Inc., 2008.

Lubliner, J., Oliver, J., Oller, S., and Oñate, E., A Plastic-Damage Model for Concrete, *International Journal of Solids and Structures*, Vol. 25, 1989, pp. 299-329.

Mander, J.B., Priestley, M.J.N., Park, R., Theoretical Stress-Strain Model for Confined Concrete, *Journal of Structural Engineering*, Vol. 114, No. 8, August 1988, pp. 1804-1826.

Martin, J., Stanton, J., Mitra, N., and Lowes, L.N., Experimental Testing to Determine Concrete Fracture Energy Using Simple Laboratory Test Setup, *ACI Materials Journal*, Vol. 104, No. 6, November-December 2007, pp. 575-584.

MatWeb, Advanced Elastomer Systems Geolast® 701-70 Thermoplastic Rubber, <http://www.matweb.com/search/datasheet.aspx?matid=22596>., Retrieved January 16, 2008.

Muguruma, H., Watanabe, F., and Nishiyama, M., Improving Ductility of Pretensioned High Strength Spun Concrete Piles by Lateral Confining of Concrete, *Proceedings of the Pacific Conference on Earthquake Engineering*, Vol. 1, Wairakei, New Zealand, August 1987, pp. 385-396.

- Pam, H.J., Park, R., and Priestley, M.J.N., Seismic Performance of Prestressed Concrete Piles and Pile-Pile Cap Connections, Research Report No. 88-3, Department of Civil Engineering, University of Canterbury, New Zealand, March 1988.
- Pender, M.J., Aseismic Pile Foundation Design Analysis, *Bulletin of the New Zealand National Society for Earthquake Engineering*, Vol. 26, No. 1, 1993, pp. 49-160.
- Priestley, M.J.N., Seible, F., and Calvi, G.M., *Seismic Retrofit and Design of Bridges*, John Wiley and Sons, New York, © 1996.
- Poulos, H.G., and Davis, E.H., *Pile Foundation Analysis and Design*, John Wiley and Sons, New York, © 1980.
- Roesler, J., Paulino, G.H., Park, K., and Gaedicke, C., Concrete Fracture Prediction Using Bilinear Softening, *Cement and Concrete Composites*, Vol. 29, 2007, pp. 300-312.
- SAP2000 Advanced Nonlinear Software and Documentation, Version 11.0.4. Computers & Structures, Inc, 2007.
- Sathishbalamurugan, M., Numerical Simulation of the Performance of Sand Columns, M.S. thesis, Washington State University, 2004.
- Shafiei-Tehrany, R. (2008). Seismic Assessment of I-5 Ravenna Bridge with Prestressed Hollow Core Piles and Multiple Column Piers, M.S. thesis, Washington State University, 2008.
- Shah, S.P., Fracture Toughness for High-Strength Concrete, *ACI Materials Journal*, Vol. 87, No. 3, May-June 1990, pp. 260-265.
- Suarez, V., Implementation of Direct Displacement Based Design for Pile and Drilled Shaft Bents, M.S. thesis, North Carolina State University, 2005.
- Tuladhar, R., Maki, T., and Mutsuyoshi, H., Cyclic Behavior of Laterally Loaded Concrete Piles Embedded into Cohesive Soils. *Earthquake Engineering and Structural Dynamics*, Vol. 37, August 2007, pp. 43-59.
- United States Geological Survey (USGS). Washington Earthquake Information. Retrieved August 25, 2008, from USGS: Tectonic Plate Motions, Crustal Blocks, and Shallow Earthquakes in Cascadia, <http://geomaps.wr.usgs.gov/pacnw/rescasp1.html>, June 21, 2002
- Useugi, M., Kishida, H., and Tsubakihara, Y. Behavior of Sand Particles in Sand-Steel Friction, *Soil and Foundations*, Vol. 28, No. 1, 1988, pp. 107-118.

Washington State Department of Transportation (WSDOT). Seismic Retrofit Program.  
Retrieved August 25, 2008, from WSDOT: Bridges and Structures:  
<http://www.wsdot.wa.gov/Bridge/Reporting/SeismicRetrofitProgram.htm>, 2008.

XTRACT Software and Documentation, Version 3.0.8. TRC/Imbsen Software Systems,  
Inc., 2001.

## **APPENDIX**

# APPENDIX A

## A.1 SOIL DATA

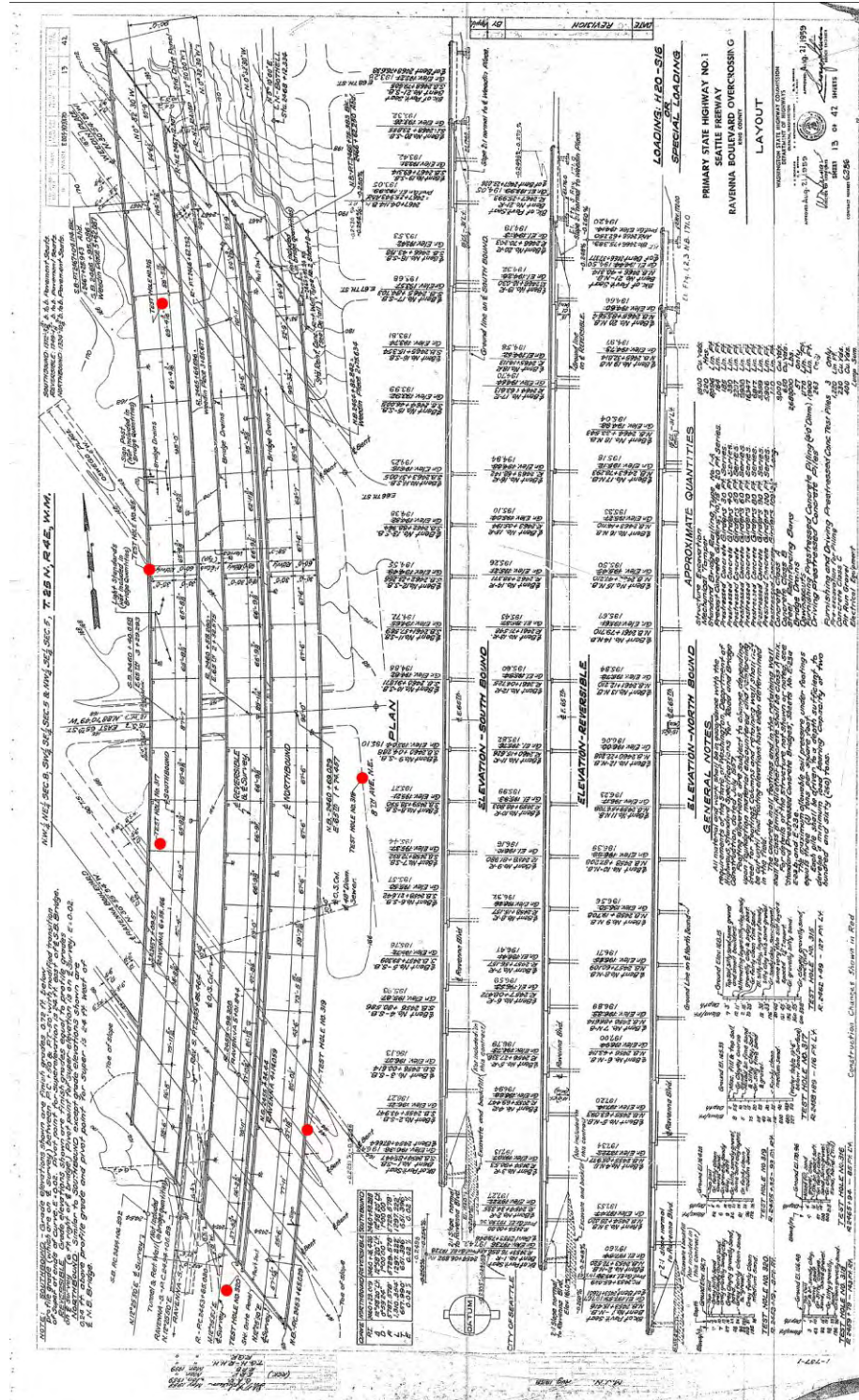


Figure A.1: Borehole Locations (Marked With Red)



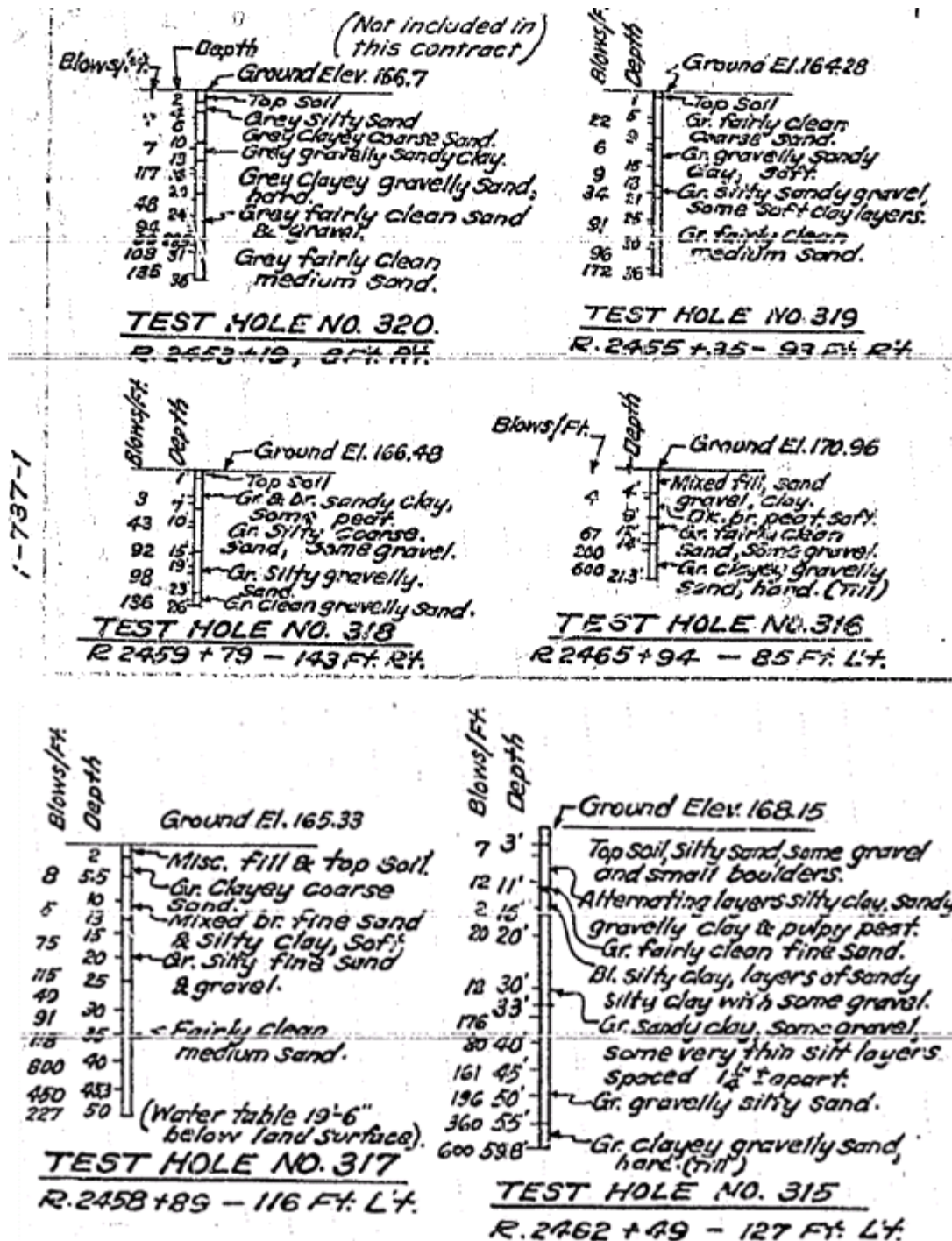


Figure A.2: Original SPT Data from Six Boreholes

## A.2 CONNECTION DETAILS

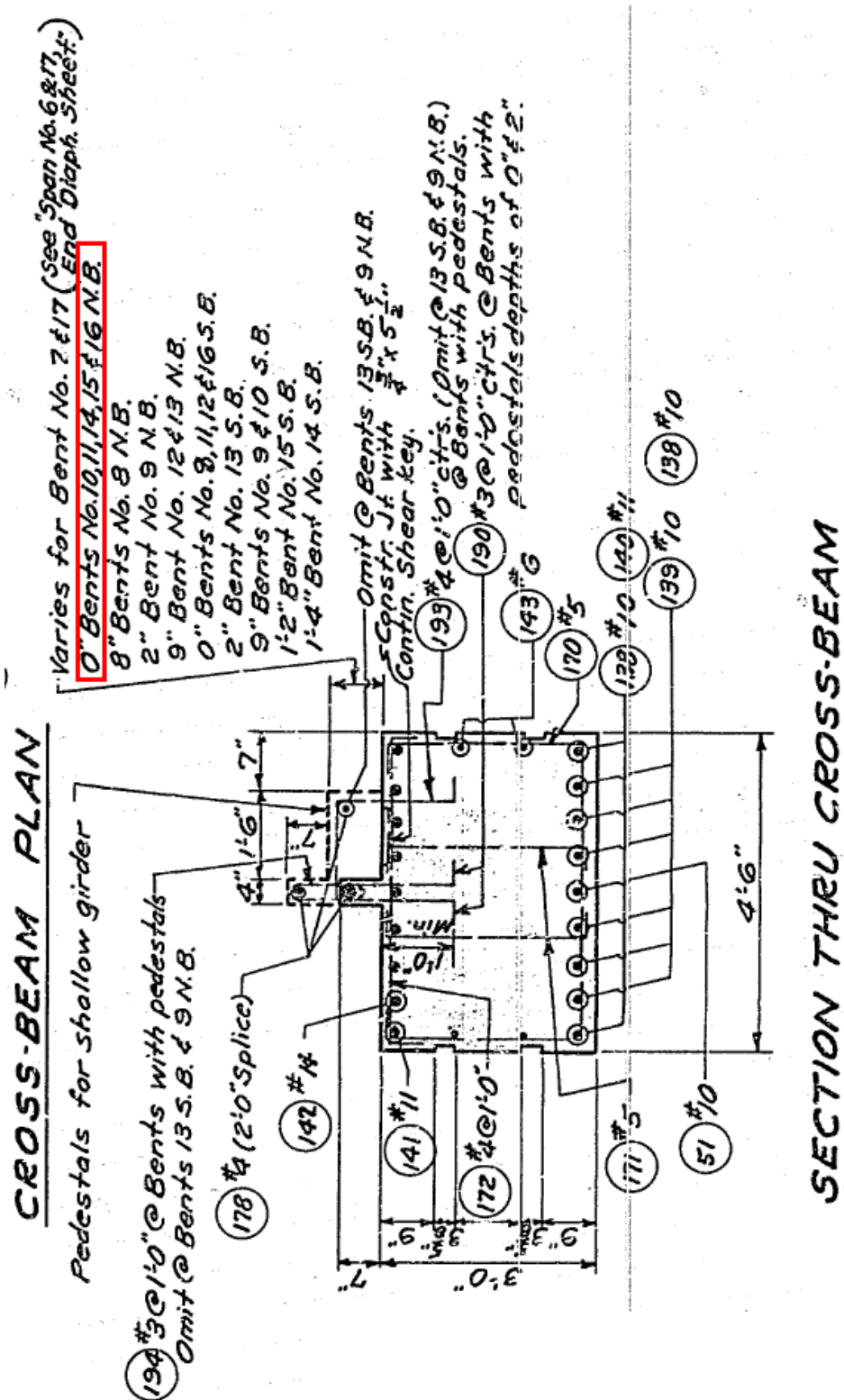
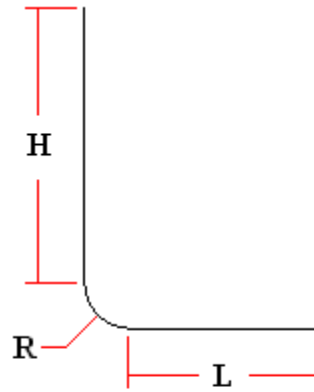


Figure A.3: Cross-Beam Details

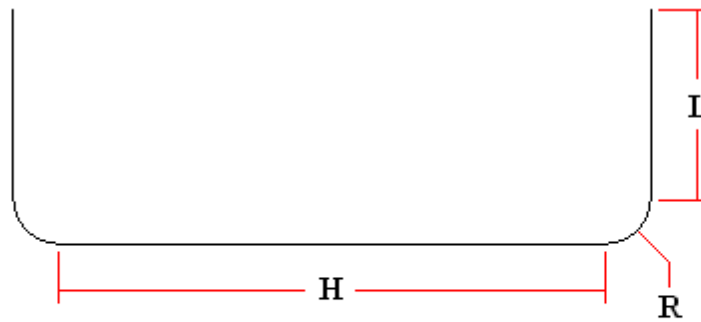






Bar Type	H	L	R
No. 4 Stirrup	700 mm (27.66 in.)	630 mm (25 in.)	38 mm (1.5 in.)
No. 5 Stirrup	190.5 mm (7.5 in.)	586 mm (23 in.)	48 mm (1.9 in.)

**Figure A.5: Cross Beam Stirrup Geometry**



Bar Type	H	L	R
No. 5 Hoop	390 mm (30.66 in.)	190.5 mm (7.5 in.)	48 mm (1.9 in.)

**Figure A.6: Cross Beam Rectangular Hoop Geometry**

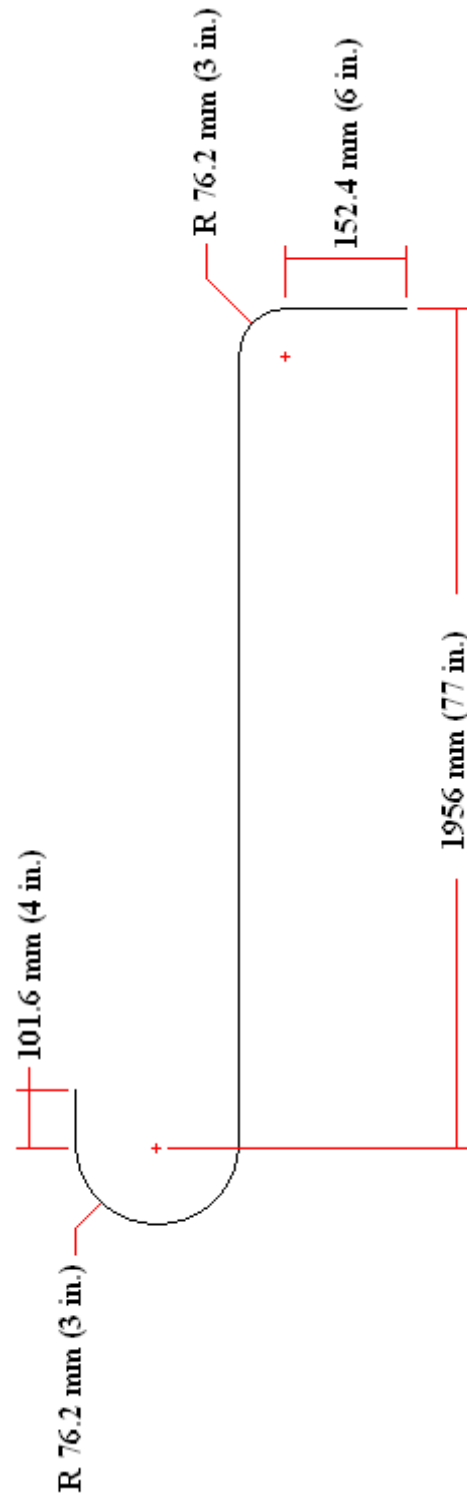


**Figure A.7: Plug to Cross Beam Tie Geometry**

## APPENDIX B

### B.1 SOFT CLAY PRESSURE-DISPLACEMENT DATA

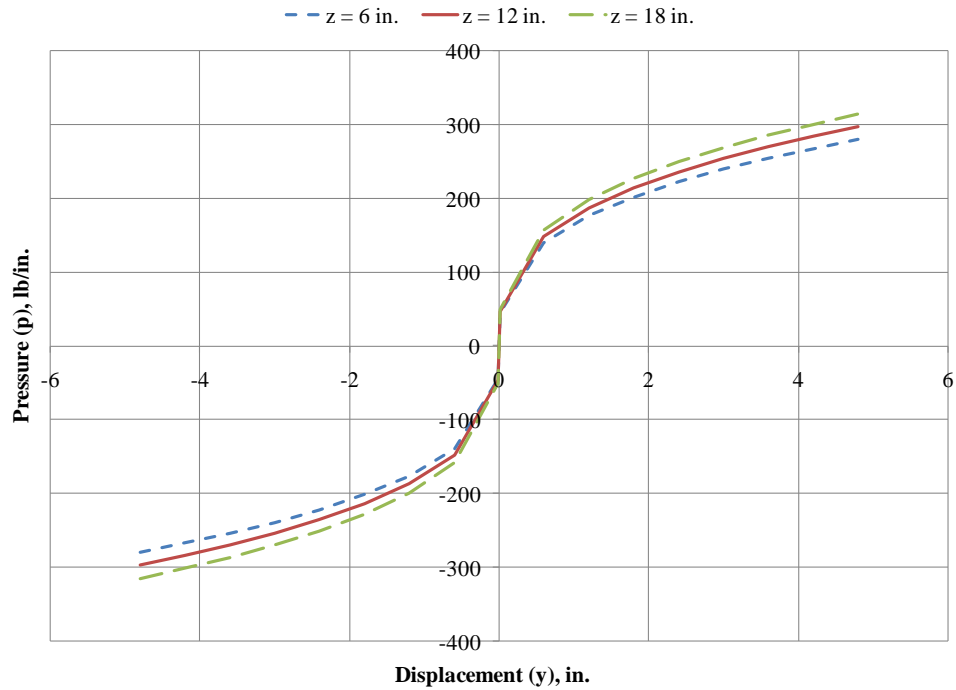


Figure B.1.1:  $p$ - $y$  Curves for Soft Clay at Depths of 6, 12, and 18 in.

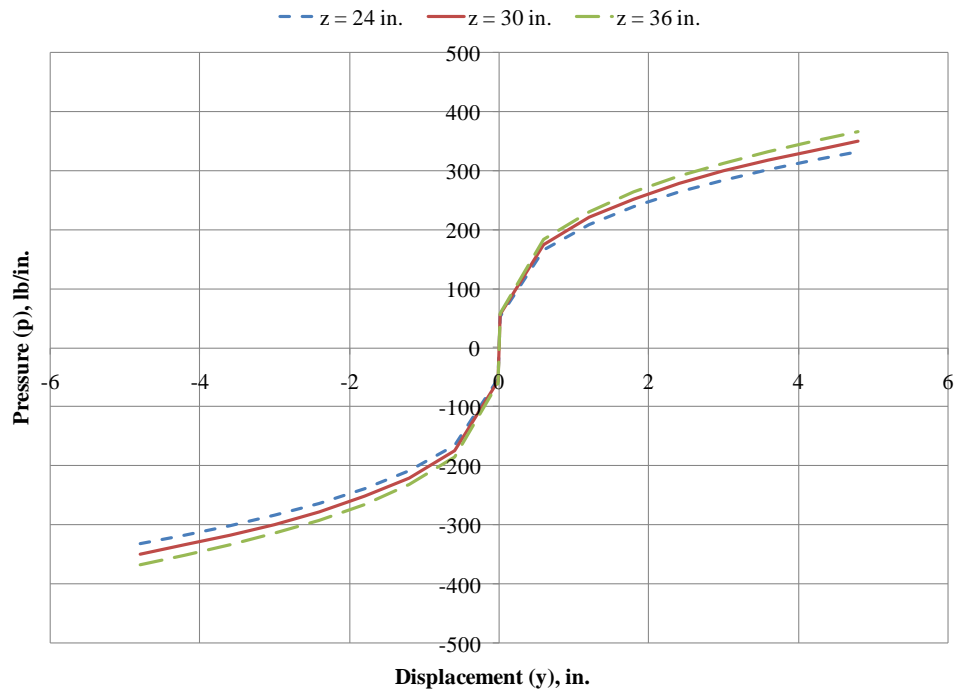
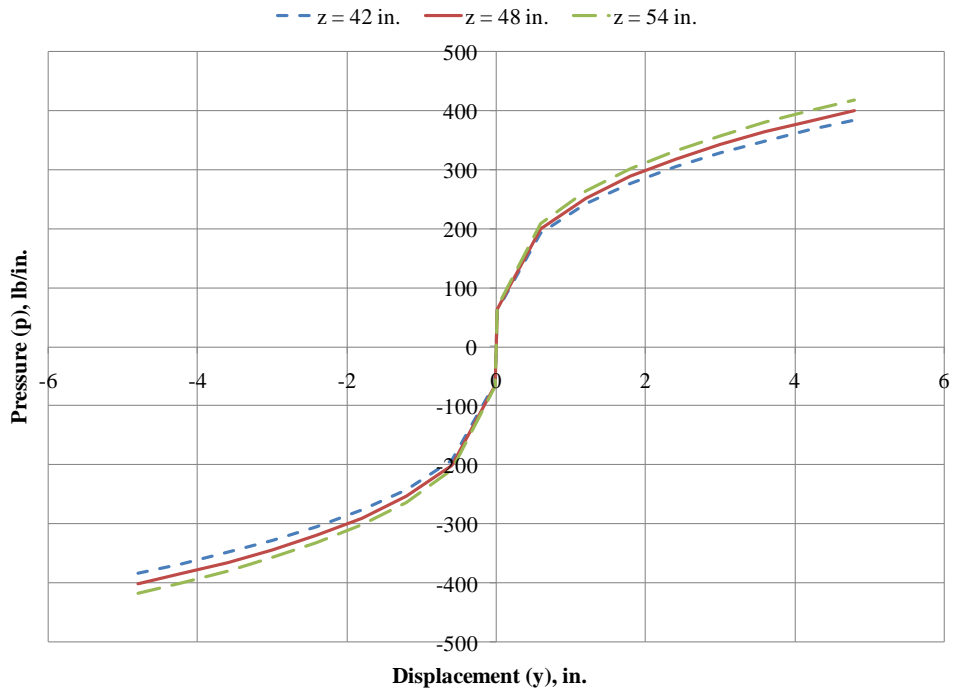
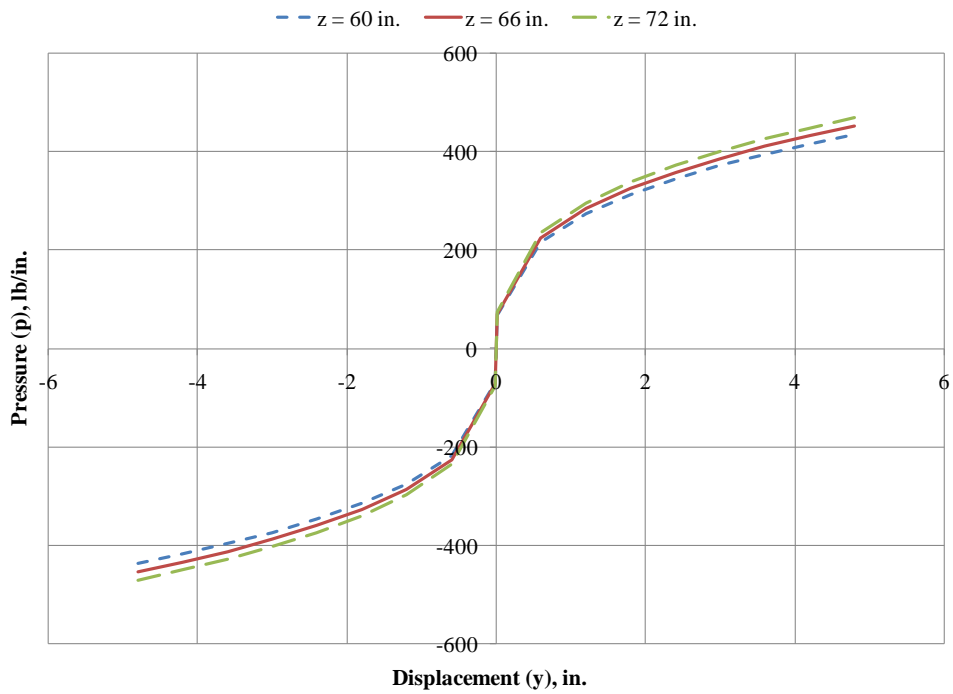


Figure B.1.2:  $p$ - $y$  Curves for Soft Clay at Depths of 24, 30, and 36 in.



**Figure B.1.3:  $p$ - $y$  Curves for Soft Clay at Depths of 42, 48, and 54 in.**



**Figure B.1.4:  $p$ - $y$  Curves for Soft Clay at Depths of 60, 66, and 72 in.**

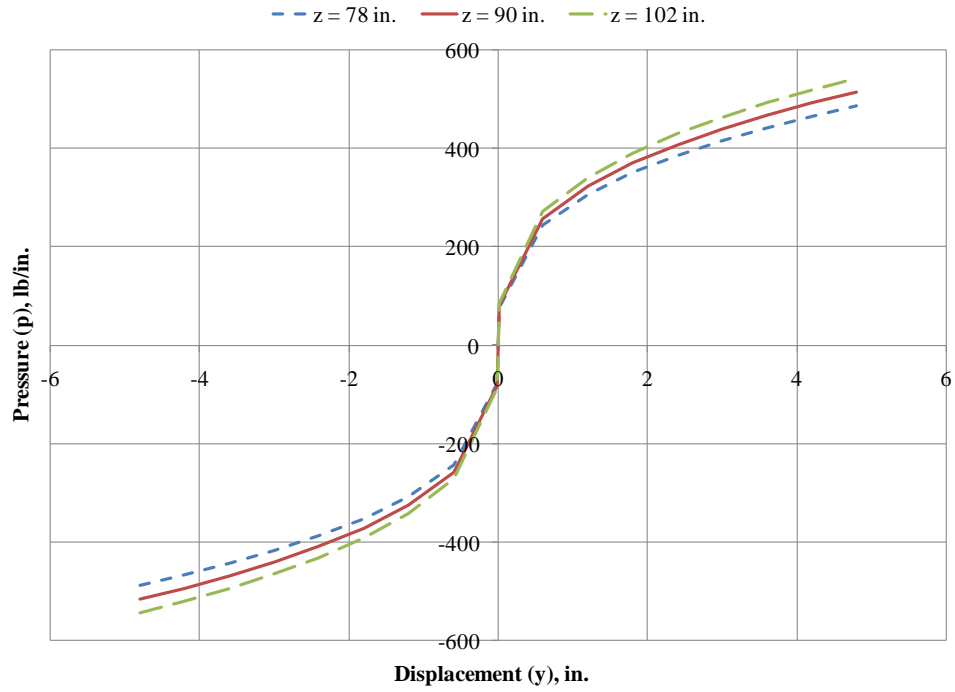


**Figure B.1.5:  $p$ - $y$  Curves for Soft Clay at Depths of 78, 90, and 102 in.**

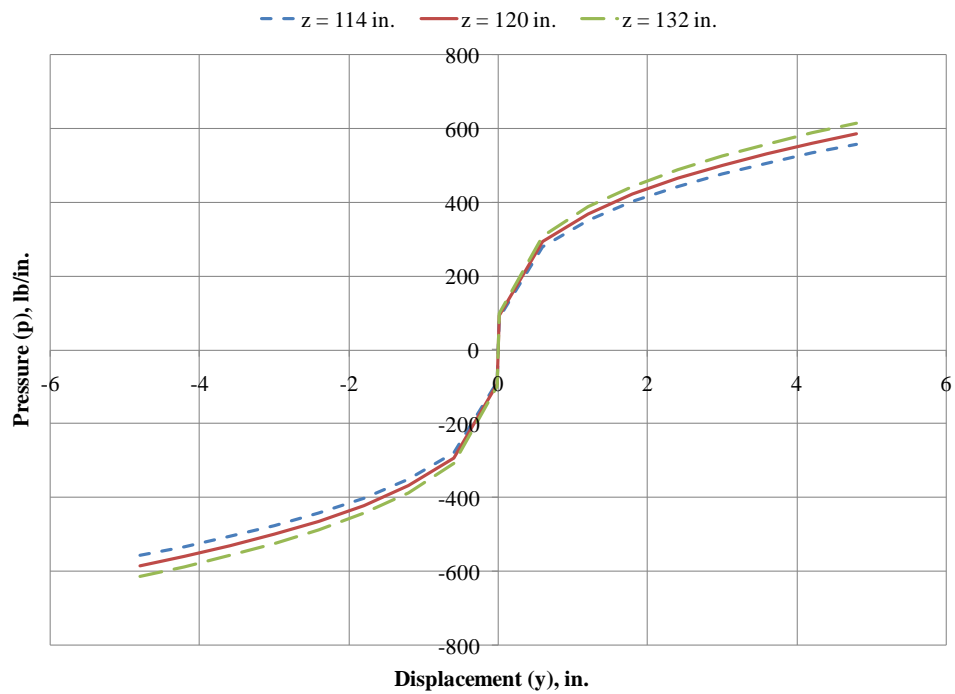


**Figure B.1.6:  $p$ - $y$  Curves for Soft Clay at Depths of 114, 120, and 132 in.**

## B.2 MEDIUM CLAY PRESSURE-DISPLACEMENT DATA

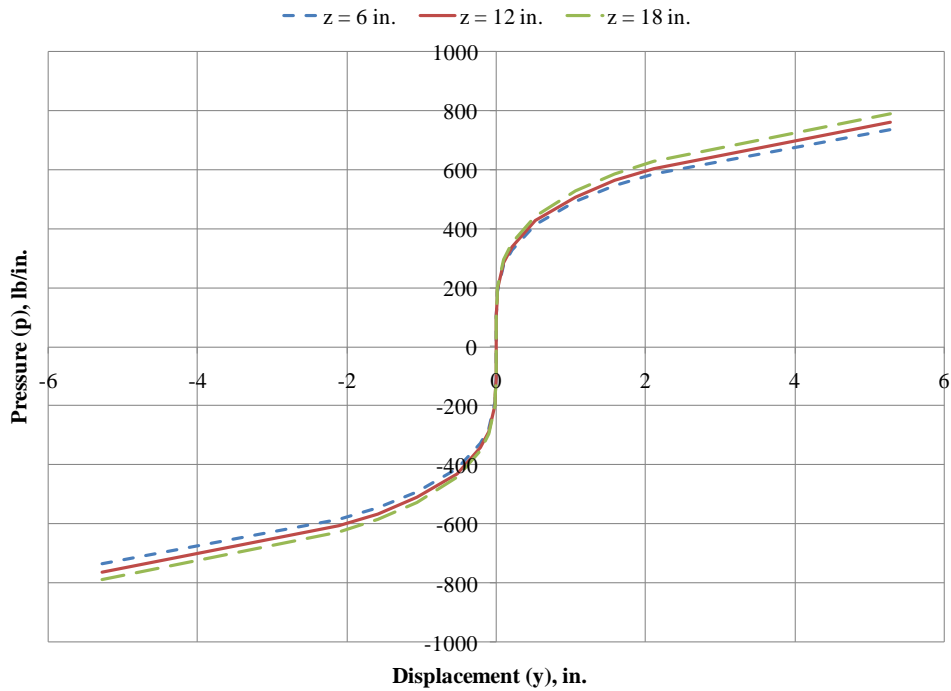


Figure B.2.1:  $p$ - $y$  Curves for Medium Clay at Depths of 6, 12, and 18 in.

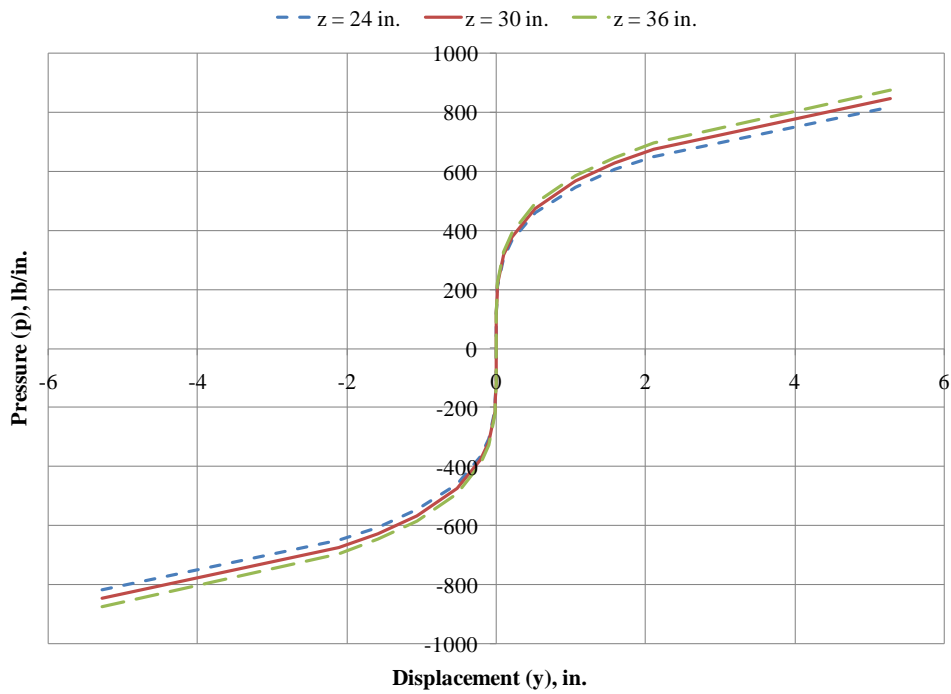
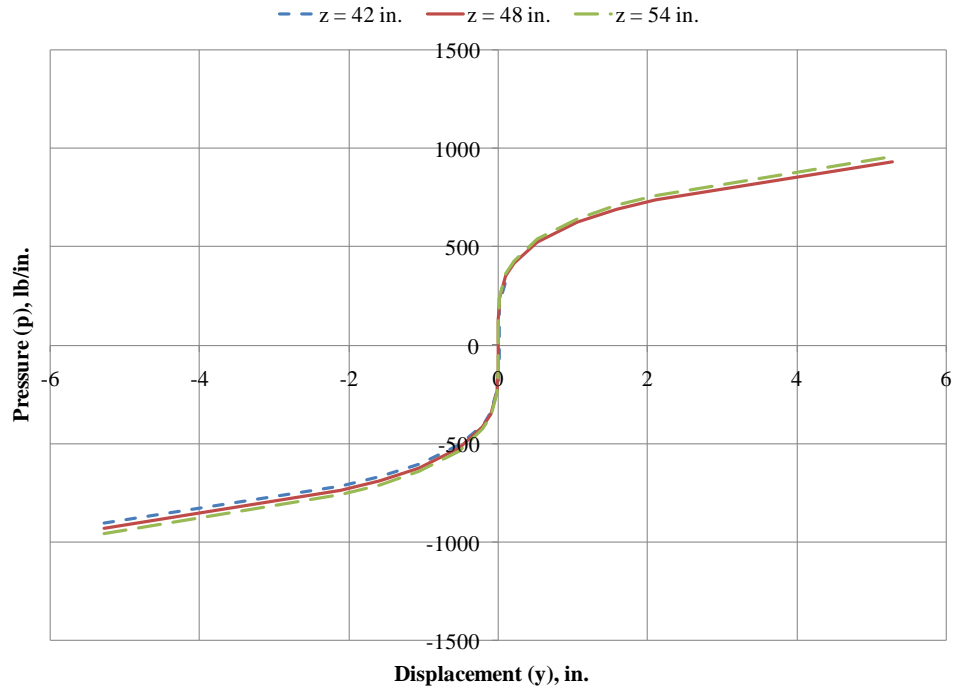
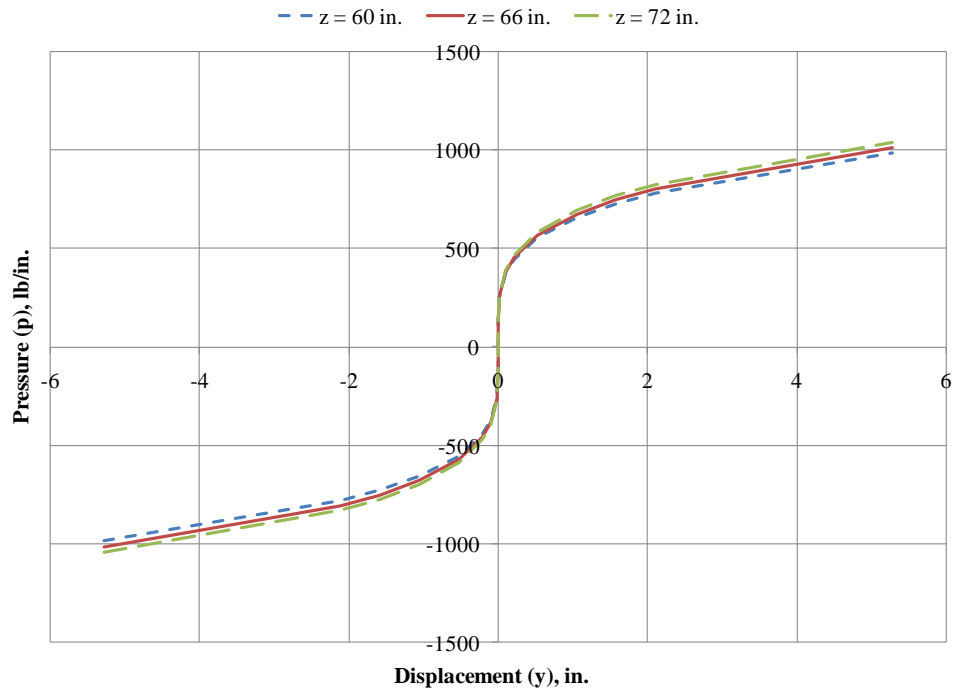


Figure B.2.2:  $p$ - $y$  Curves for Medium Clay at Depths of 24, 30, and 36 in.



**Figure B.2.3:  $p$ - $y$  Curves for Medium Clay at Depths of 42, 48, and 54 in.**



**Figure B.2.4:  $p$ - $y$  Curves for Medium Clay at Depths of 60, 66, and 72 in.**



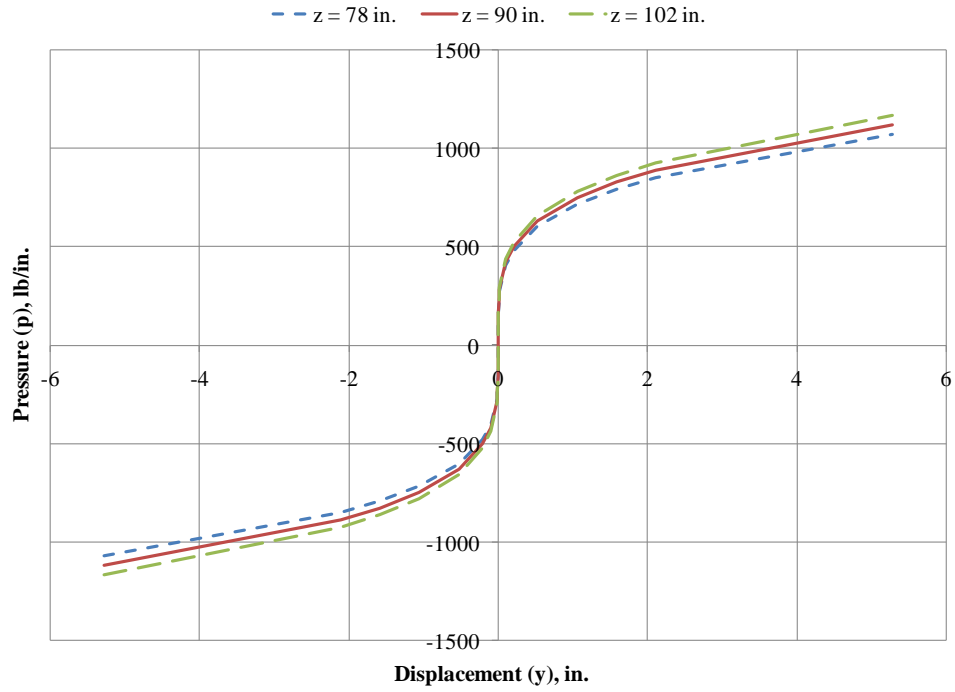


**Figure B.2.5:  $p$ - $y$  Curves for Medium Clay at Depths of 78, 90, and 102 in.**

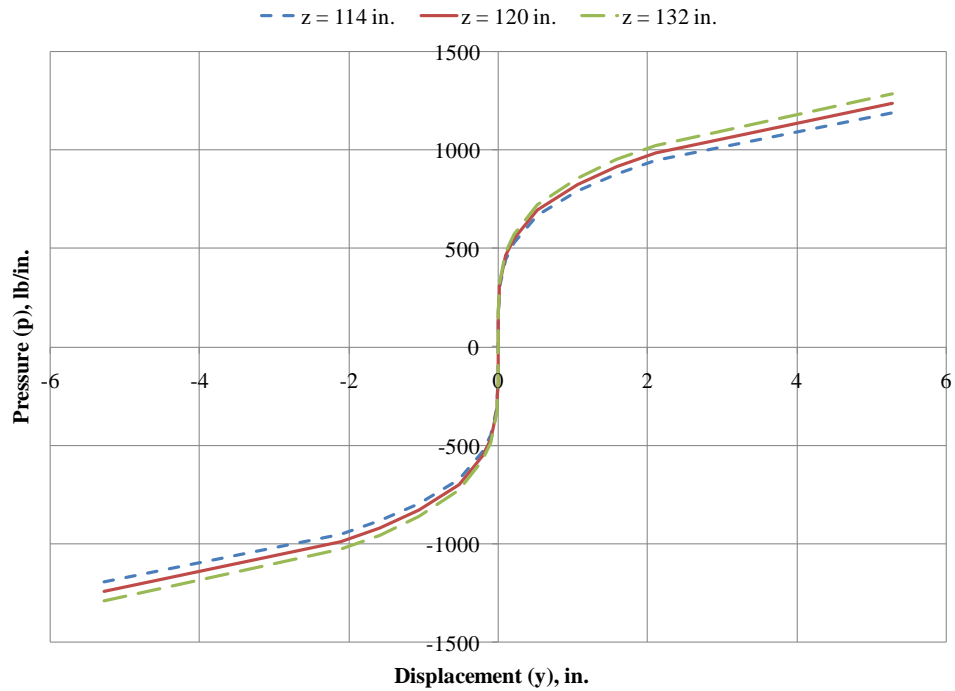


**Figure B.2.6:  $p$ - $y$  Curves for Medium Clay at Depths of 114, 120, and 132 in.**

### B.3 STIFF CLAY PRESSURE-DISPLACEMENT DATA

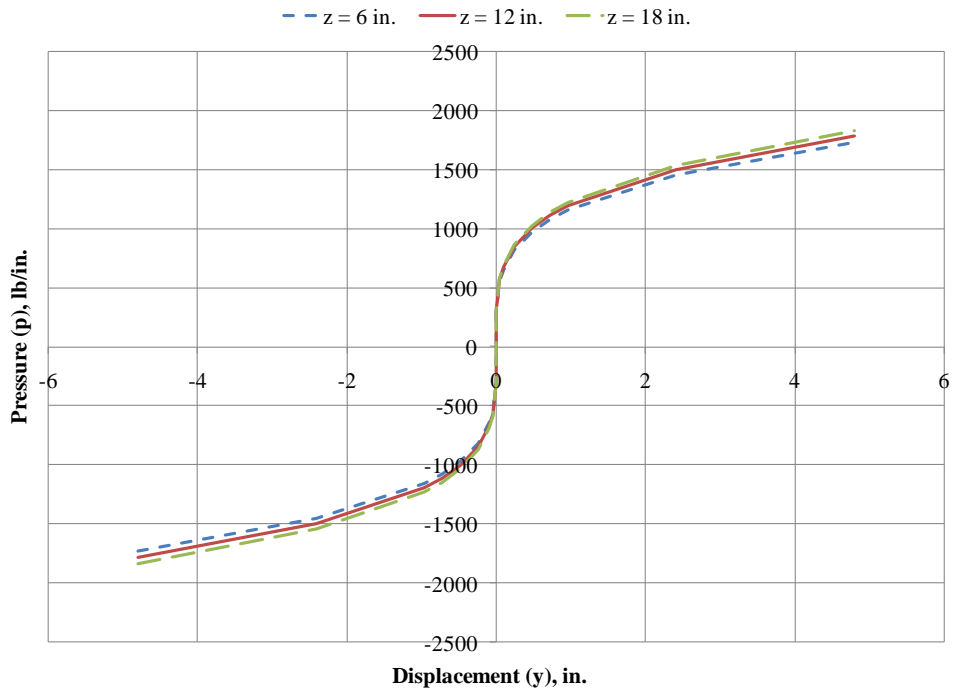


Figure B.3.1:  $p$ - $y$  Curves for Stiff Clay at Depths of 6, 12, and 18 in.

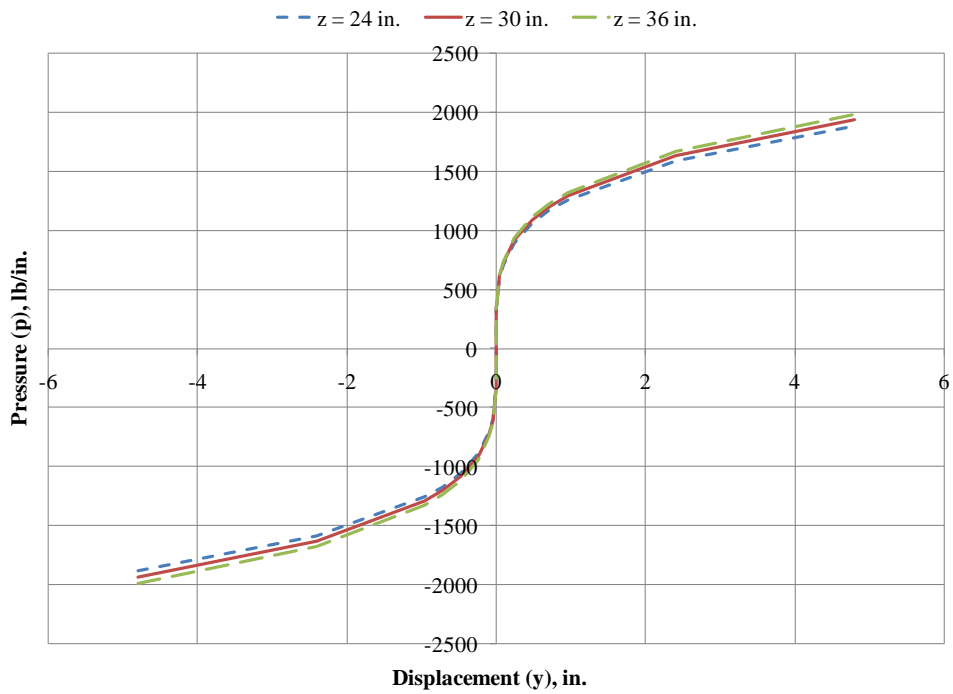
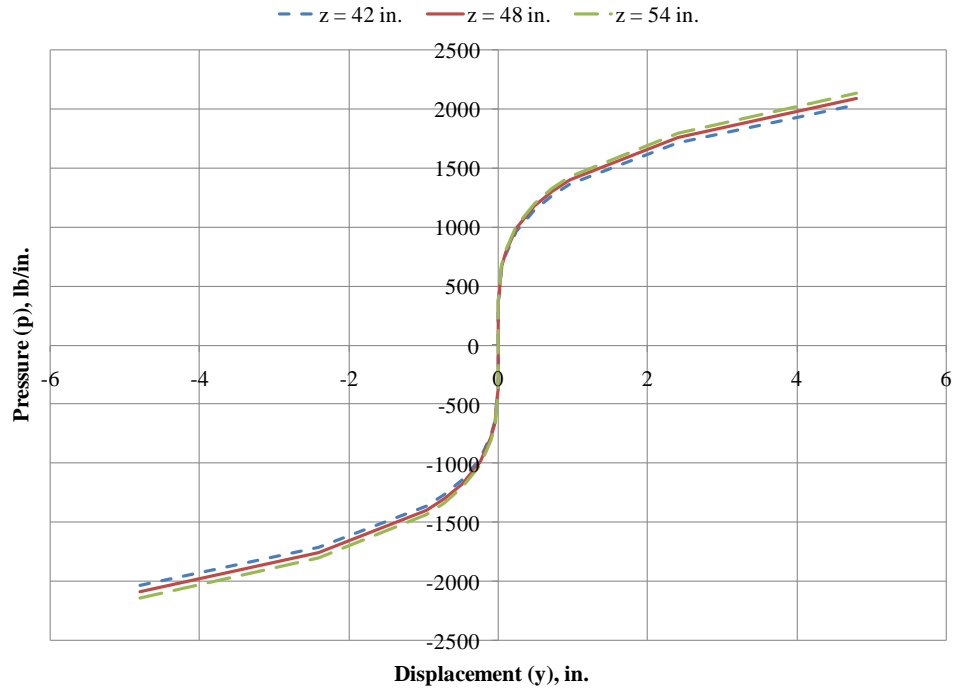
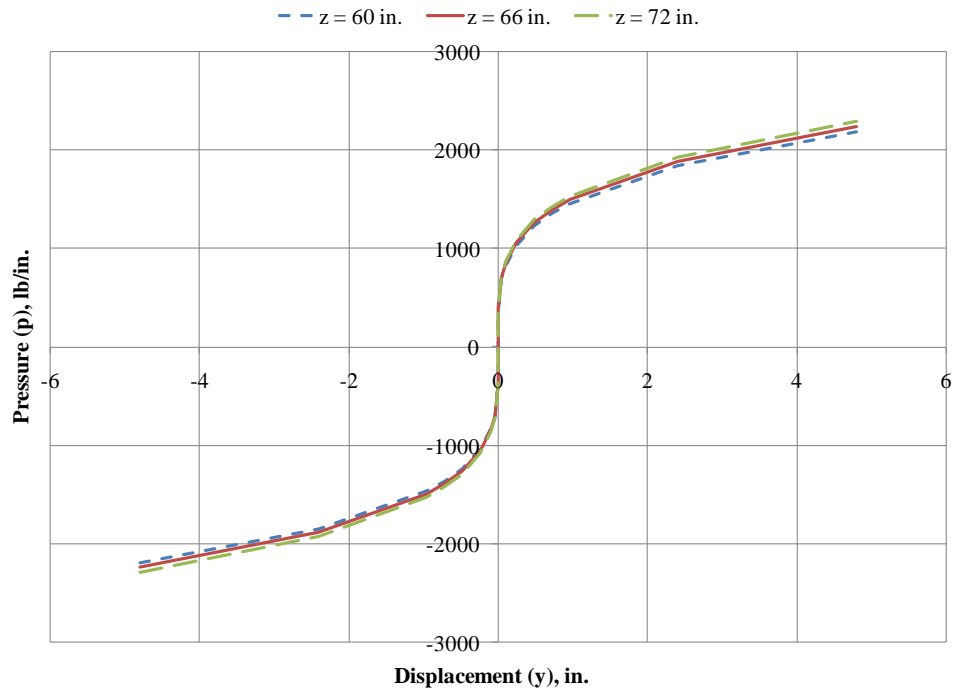


Figure B.3.2:  $p$ - $y$  Curves for Stiff Clay at Depths of 24, 30, and 36 in.



**Figure B.3.3:  $p$ - $y$  Curves for Stiff Clay at Depths of 42, 48, and 54 in.**



**Figure B.3.4:  $p$ - $y$  Curves for Stiff Clay at Depths of 60, 66, and 72 in.**

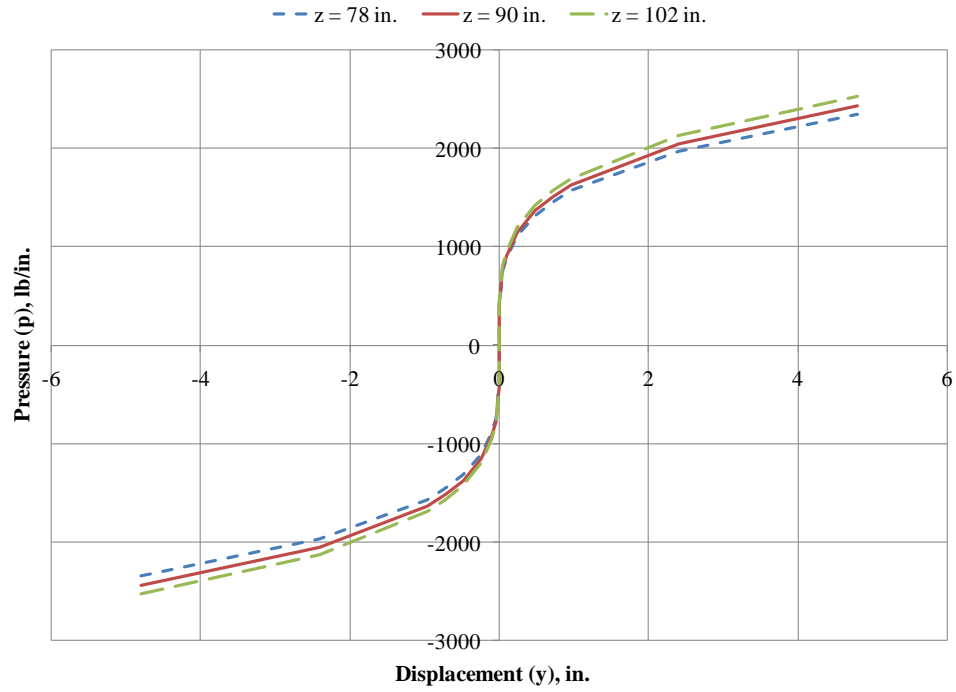


**Figure B.3.5:  $p$ - $y$  Curves for Stiff Clay at Depths of 78, 90, and 102 in.**

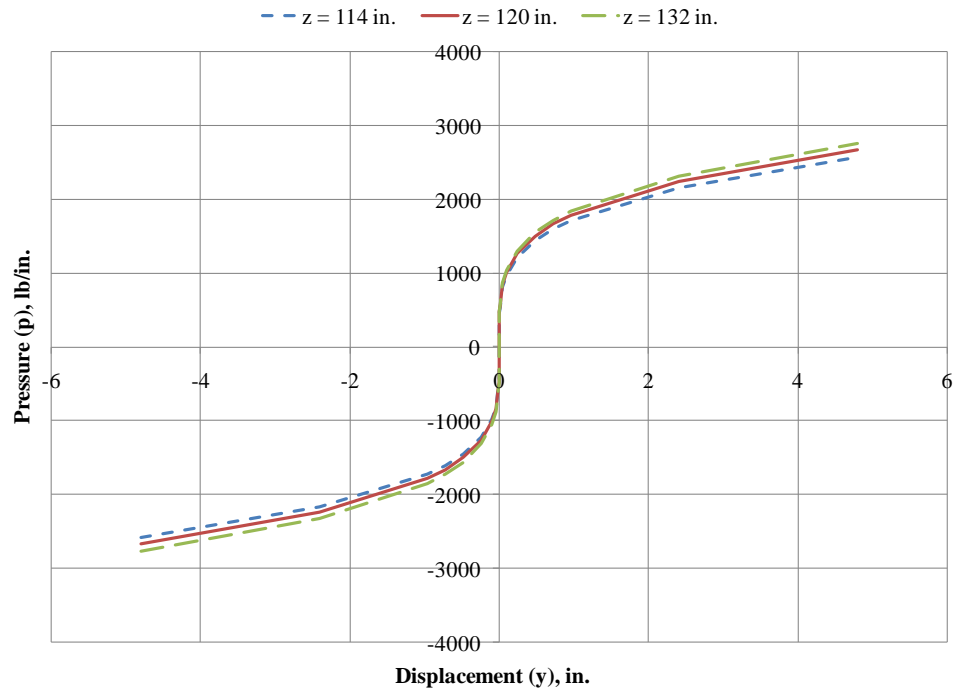


**Figure B.3.6:  $p$ - $y$  Curves for Stiff Clay at Depths of 114, 120, and 132 in.**

#### B.4 SOFT CLAY NONLINEAR SPRING DATA

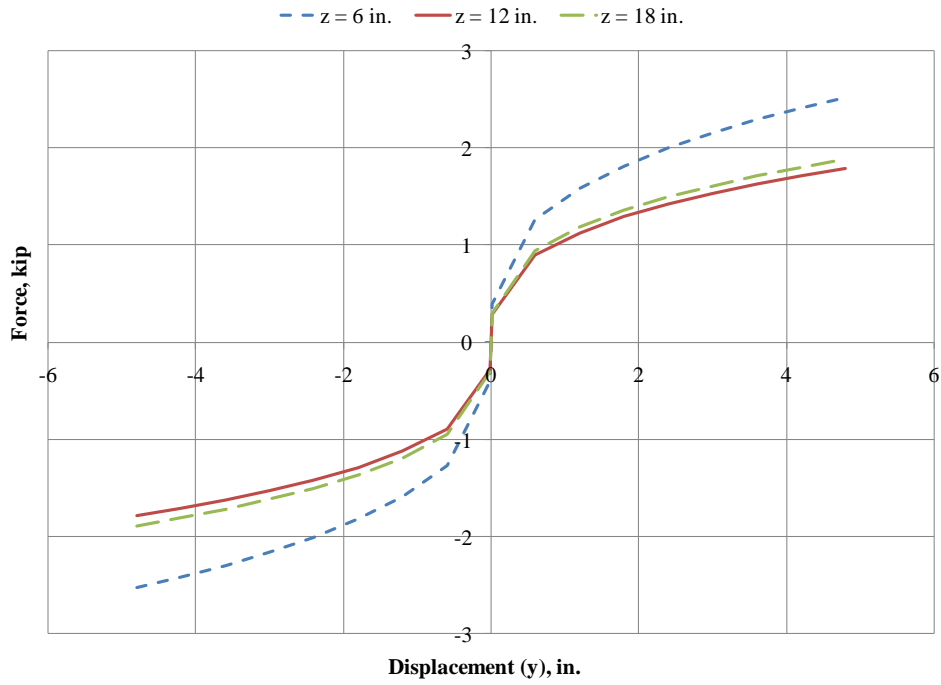


**Figure B.4.1: Force-Displacement Curves for Soft Clay at Depths of 6, 12, and 18 in.**

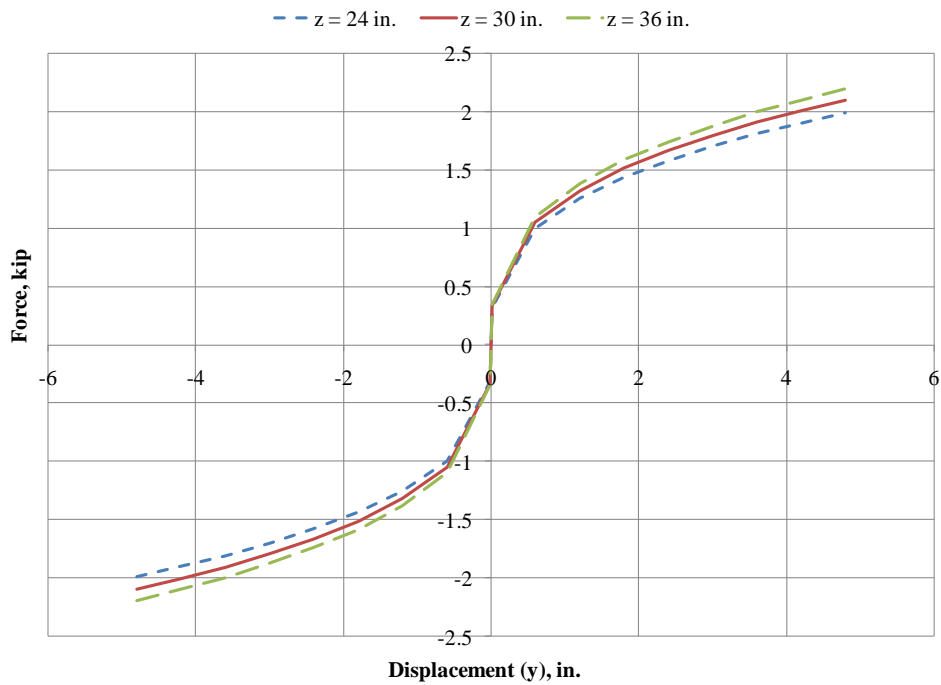


**Figure B.4.2: Force-Displacement Curves for Soft Clay at Depths of 24, 30, and 36 in.**

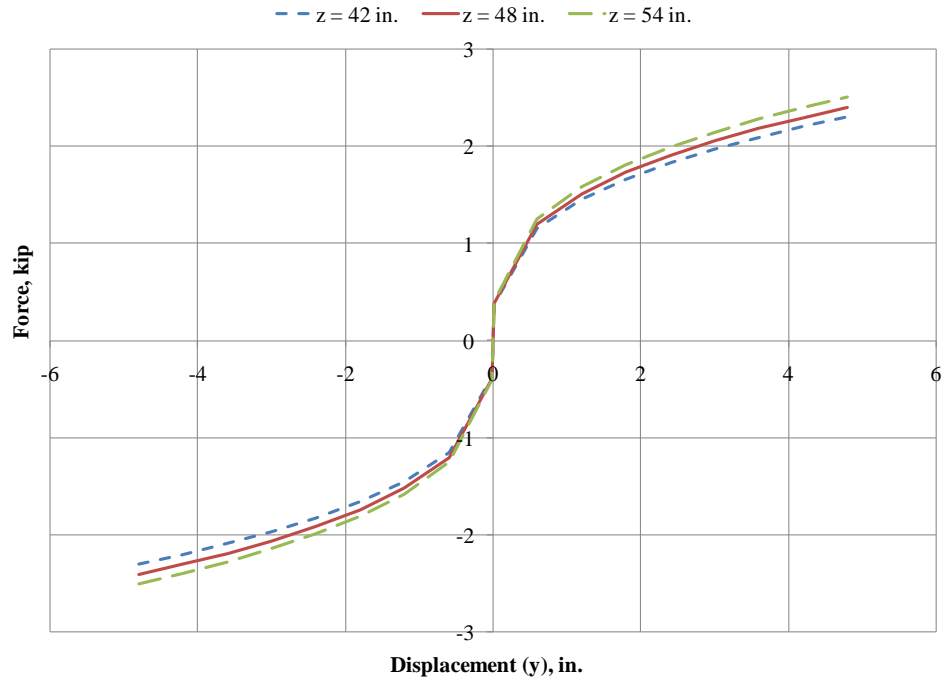


**Figure B.4.3: Force-Displacement Curves for Soft Clay at Depths of 24, 48, and 54 in.**

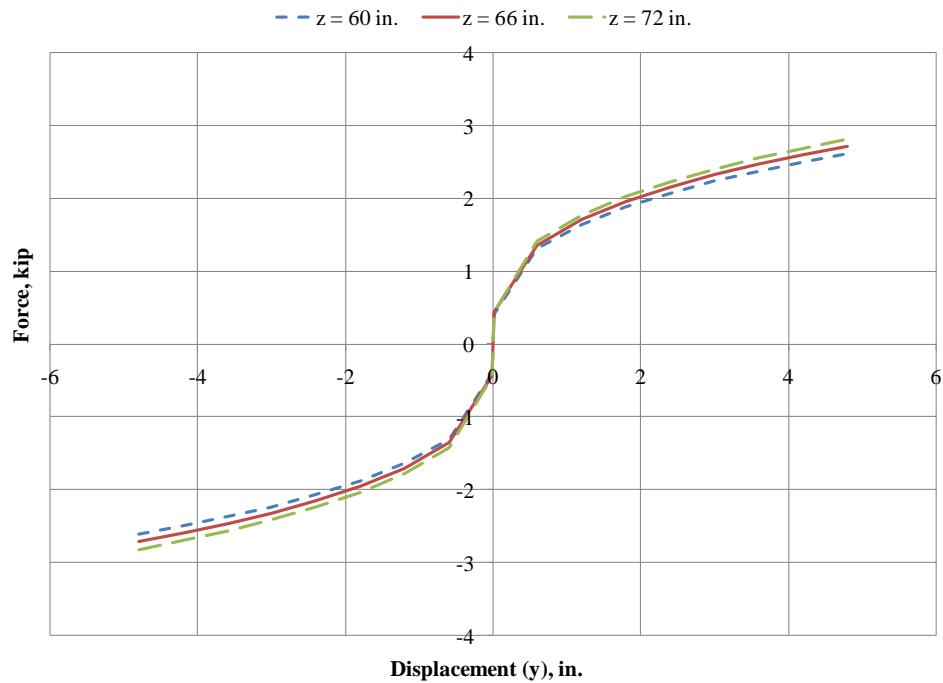


**Figure B.4.4: Force-Displacement Curves for Soft Clay at Depths of 60, 66, and 72 in.**

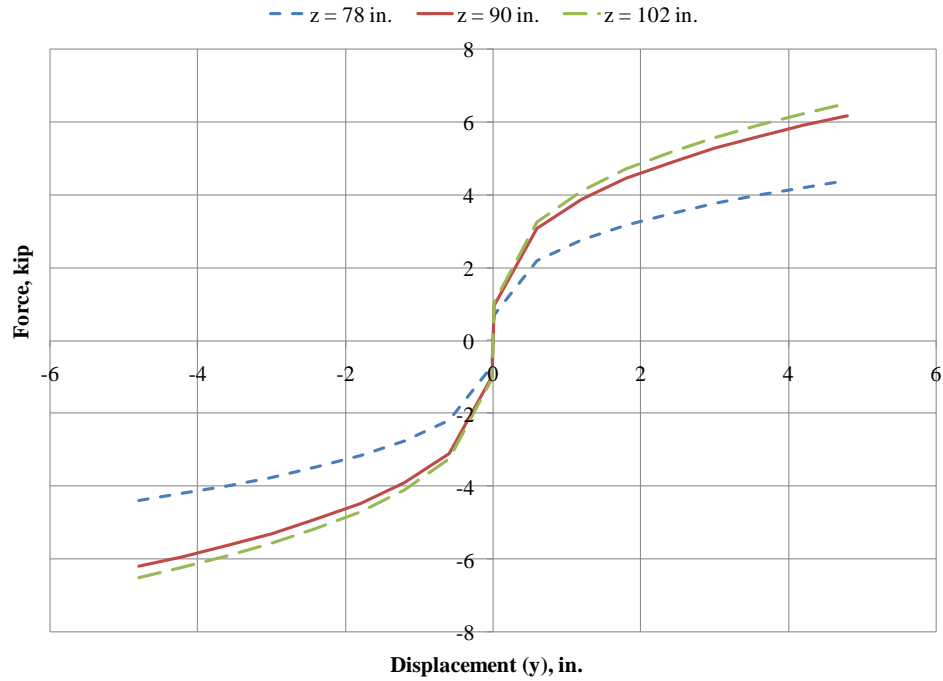


**Figure B.4.5: Force-Displacement Curves for Soft Clay at Depths of 78, 90, and 102 in.**

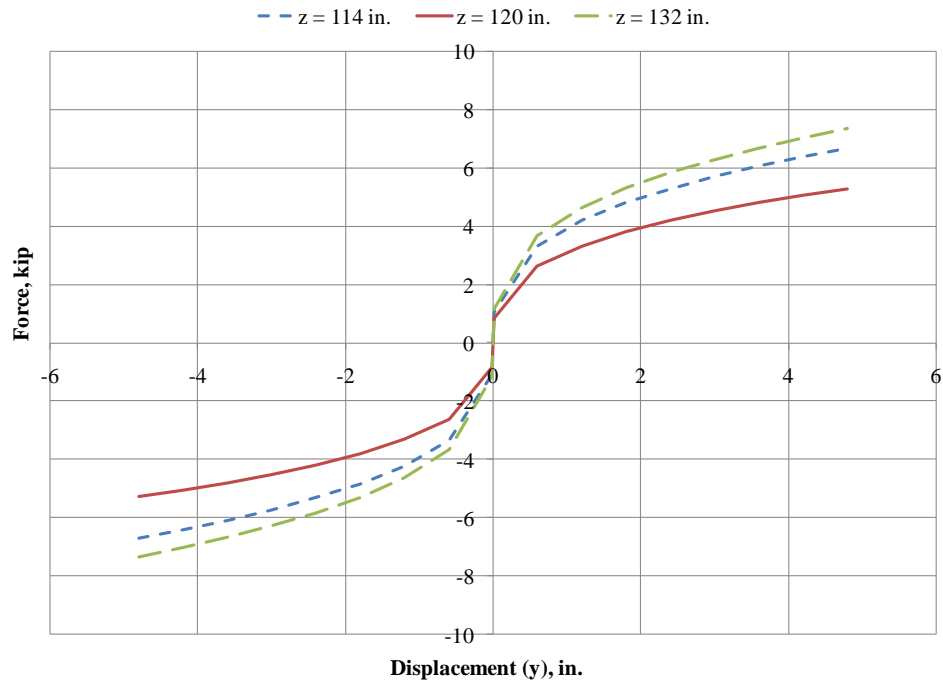


**Figure B.4.6: Force-Displacement Curves for Soft Clay at Depths of 114, 120, and 132 in.**

## B.5 MEDIUM CLAY NONLINEAR SPRING DATA

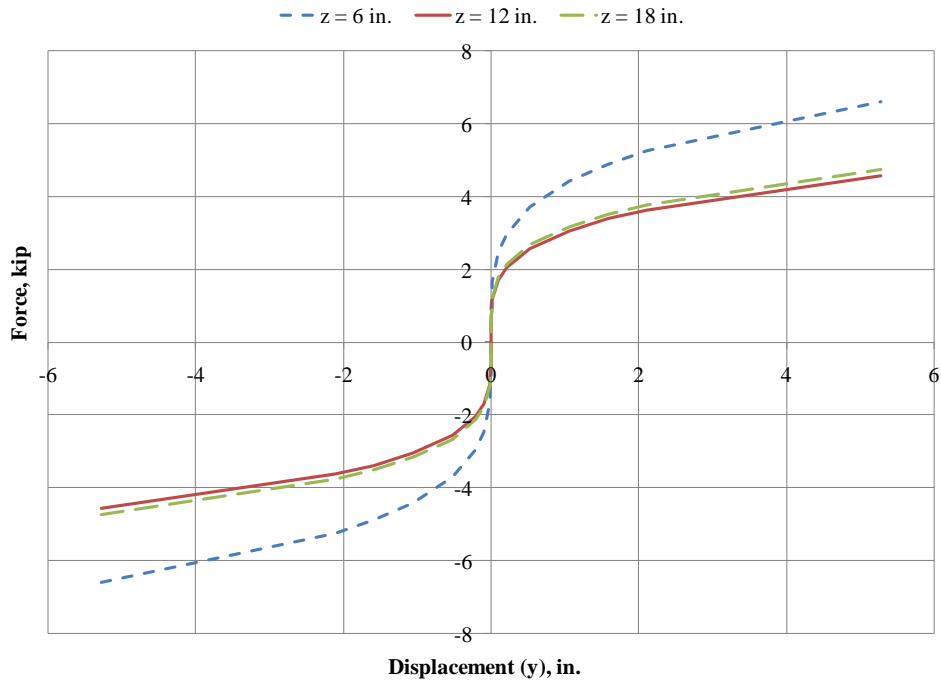


**Figure B.5.1: Force-Displacement Curves for Medium Clay at Depths of 6, 12, and 18 in.**

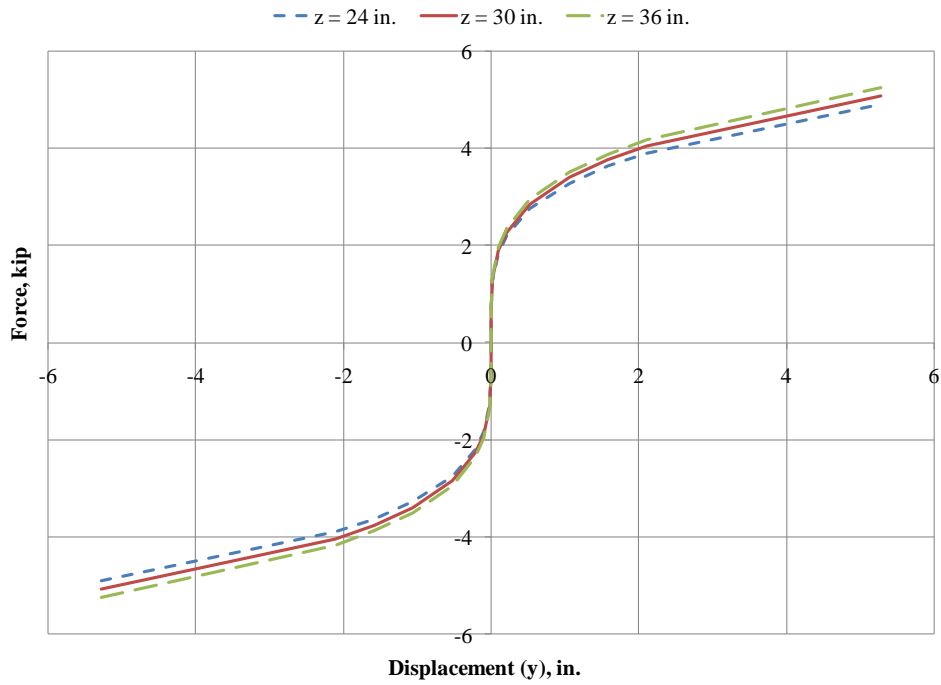


**Figure B.5.2: Force-Displacement Curves for Medium Clay at Depths of 24, 30, and 36 in.**



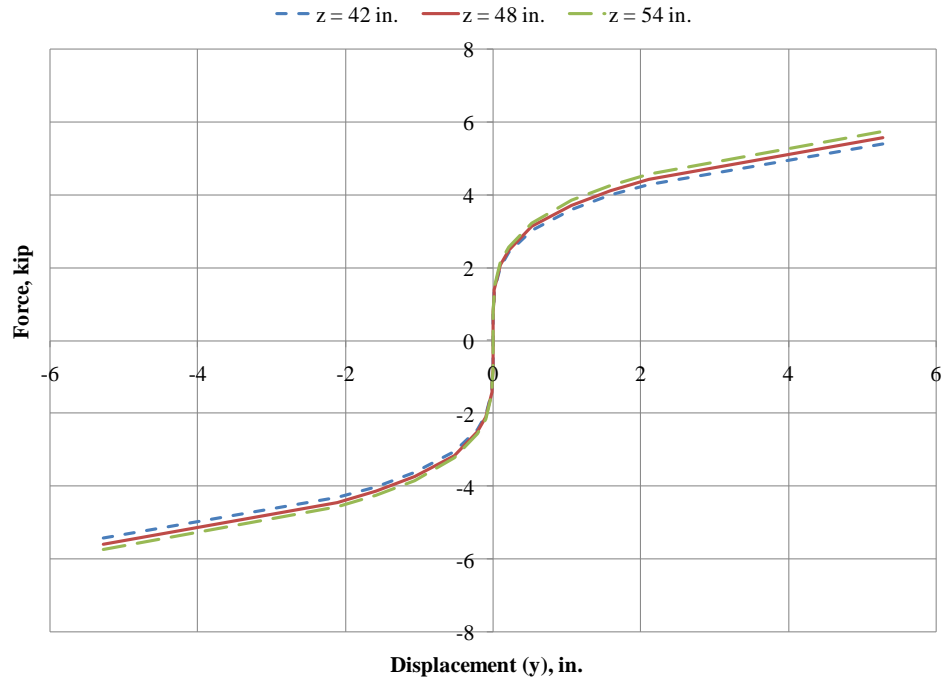


**Figure B.5.3: Force-Displacement Curves for Medium Clay at Depths of 42, 48, and 54 in.**

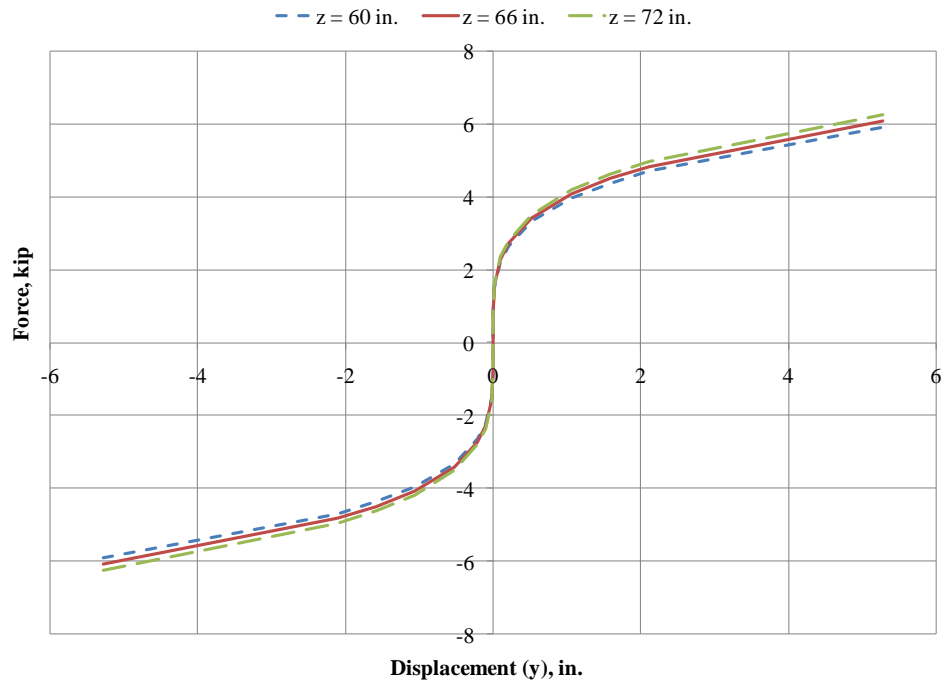


**Figure B.5.4: Force-Displacement Curves for Medium Clay at Depths of 60, 66, and 72 in.**

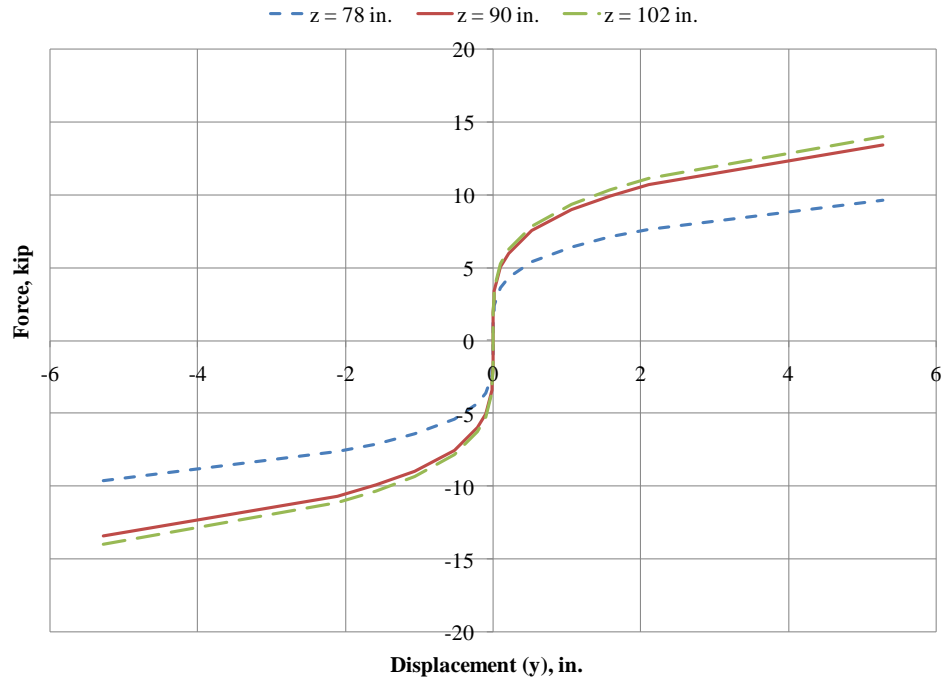


**Figure B.5.5: Force-Displacement Curves for Medium Clay at Depths of 78, 90, and 102 in.**

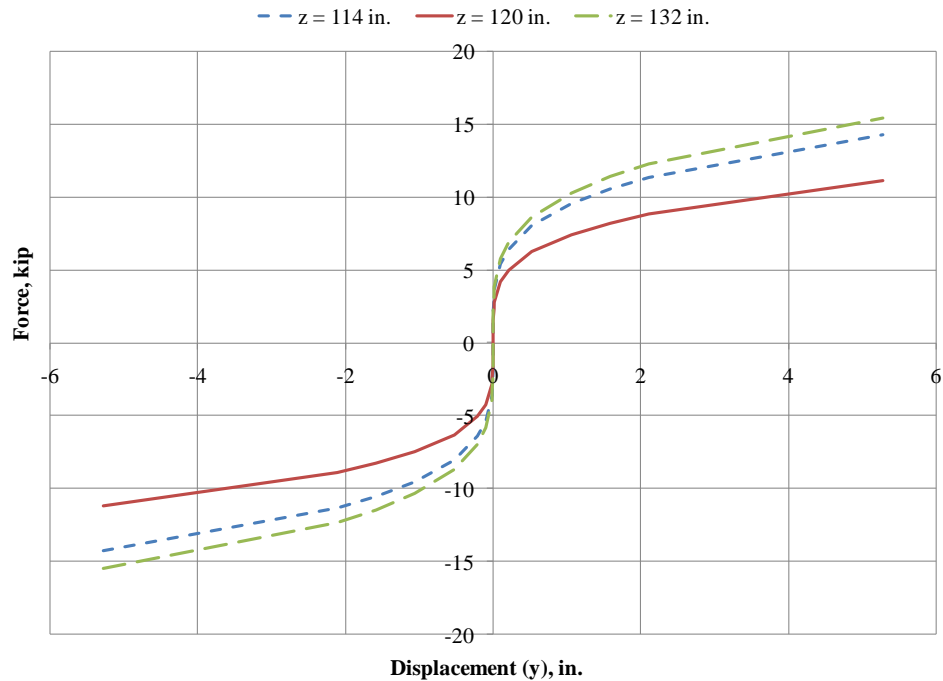


**Figure B.5.6: Force-Displacement Curves for Medium Clay at Depths of 114, 120, and 132 in.**

## B.6 STIFF CLAY NONLINEAR SPRING DATA

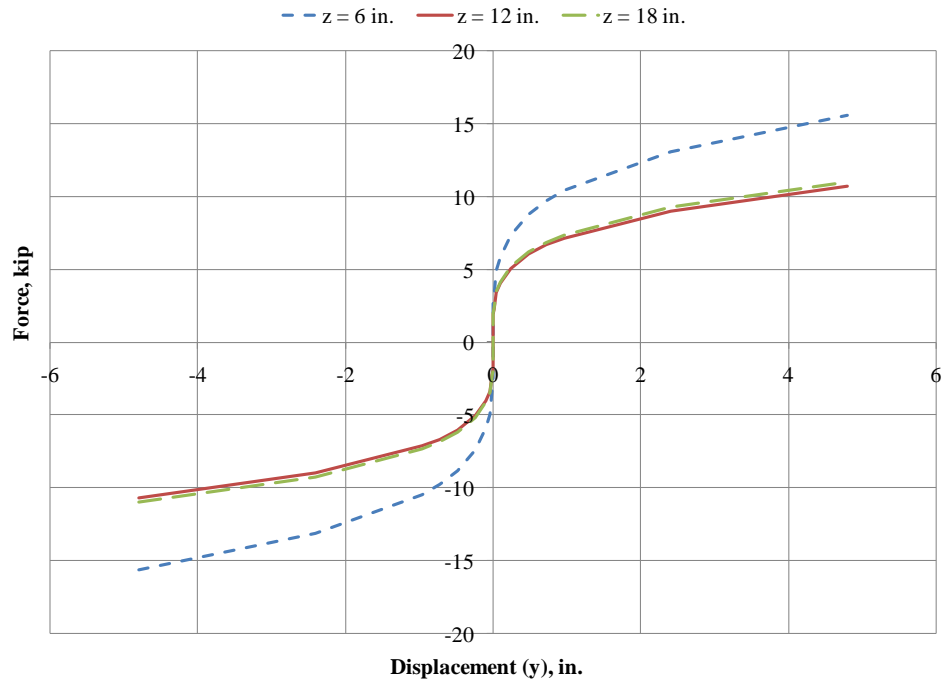


**Figure B.6.1: Force-Displacement Curves for Stiff Clay at Depths of 6, 12, and 18 in.**

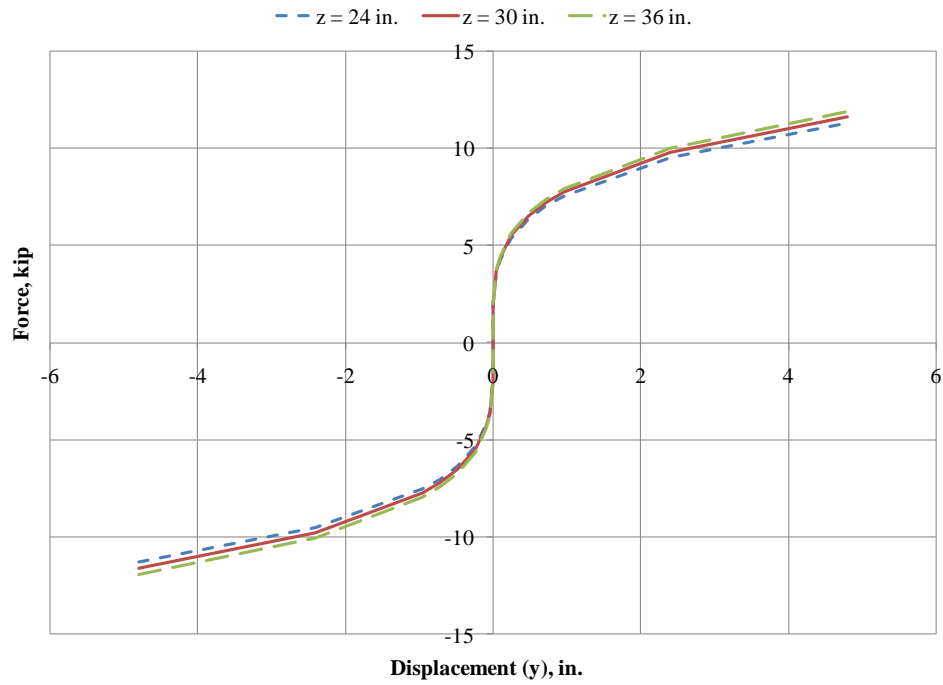


**Figure B.6.2: Force-Displacement Curves for Stiff Clay at Depths of 114, 120, and 132 in.**

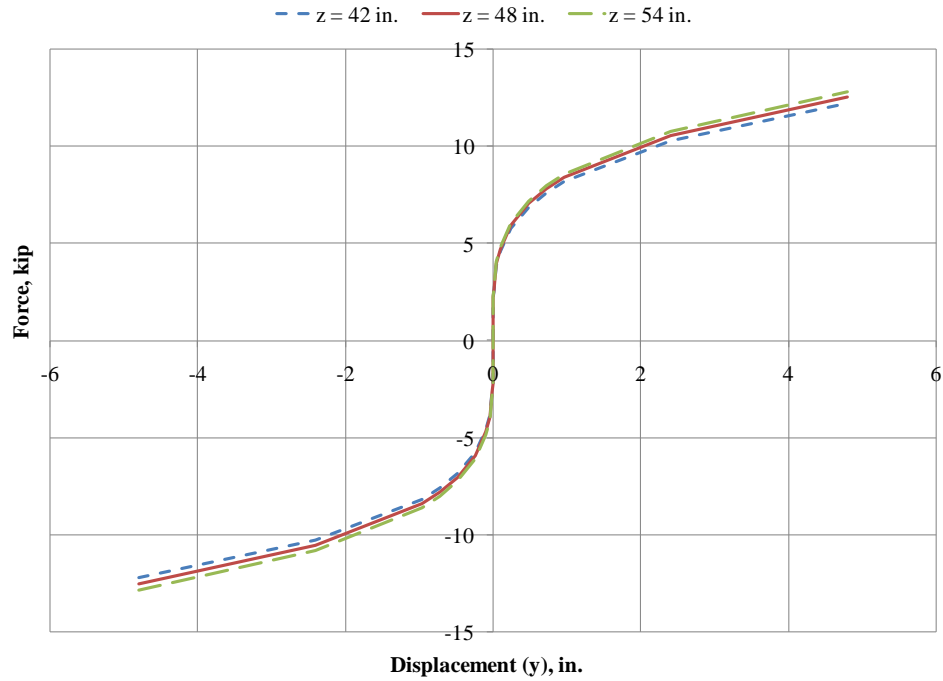


**Figure B.6.3: Force-Displacement Curves for Stiff Clay at Depths of 114, 120, and 132 in.**

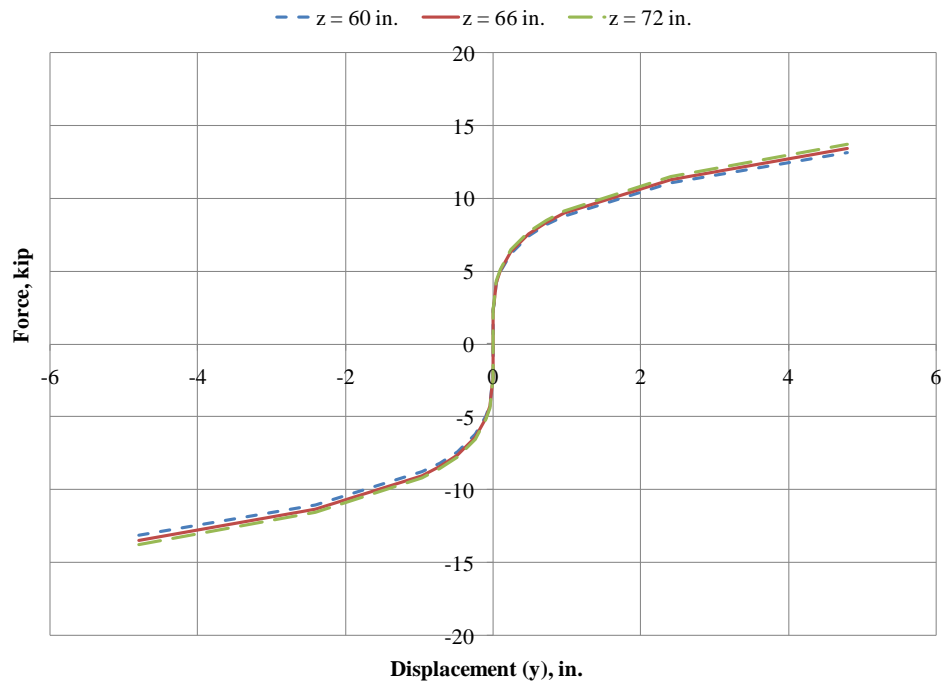


**Figure B.6.4: Force-Displacement Curves for Stiff Clay at Depths of 114, 120, and 132 in.**

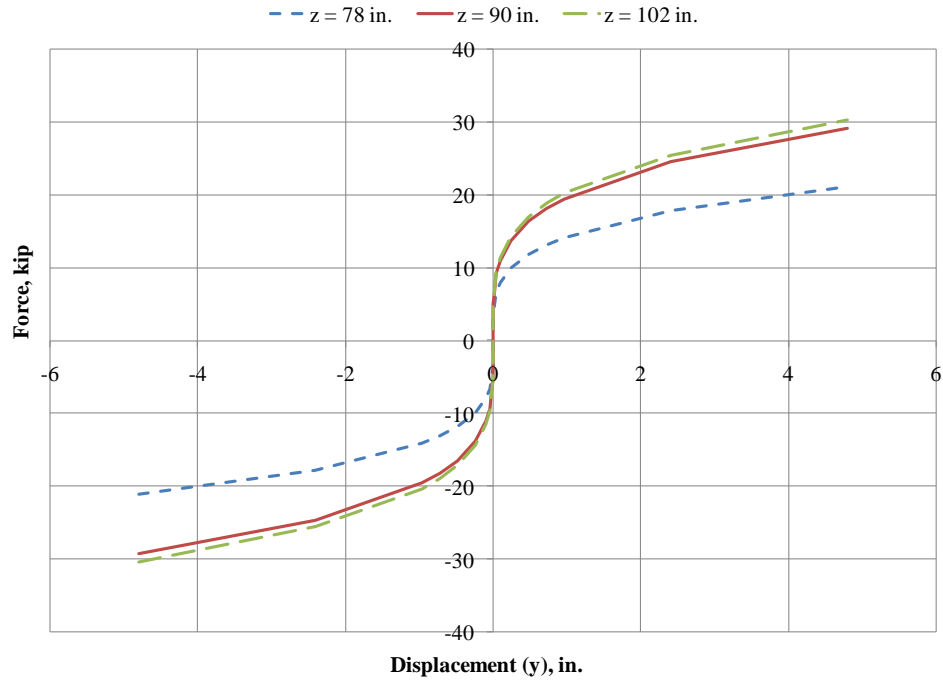


**Figure B.6.5: Force-Displacement Curves for Stiff Clay at Depths of 114, 120, and 132 in.**

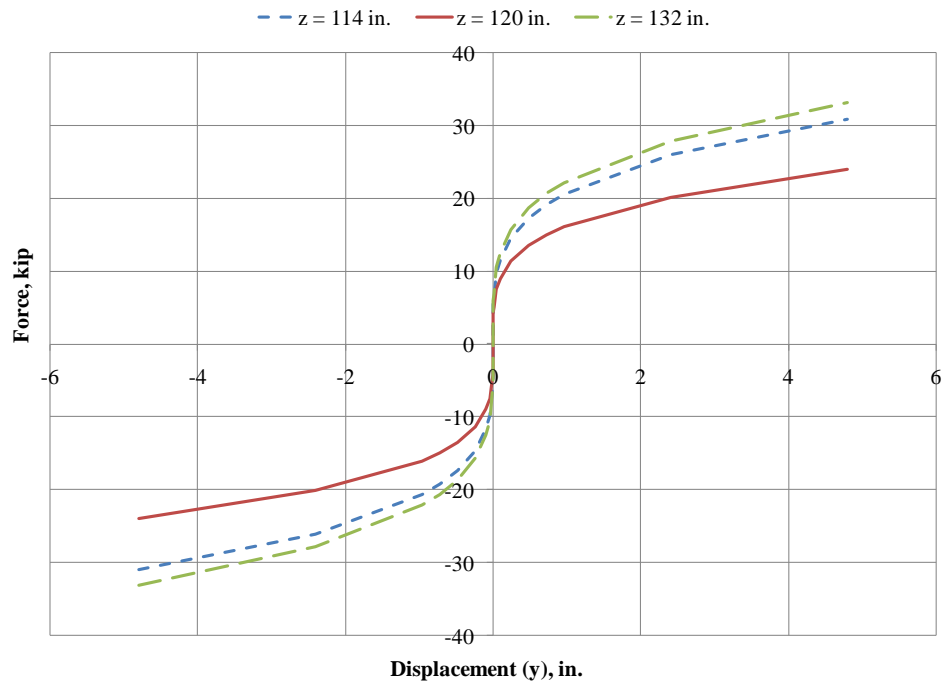


**Figure B.6.6: Force-Displacement Curves for Stiff Clay at Depths of 114, 120, and 132 in.**